Electrochemical Processing of Directionally Solidified Eutectic Alloys: Release and Characterization of Metallic Nanowires

Inaugural-Dissertation

zur
Erlangung des Doktorgrades der
Mathematisch-Naturwissenschaftlichen Fakultät
der Heinrich-Heine-Universität Düsseldorf

vorgelegt von

Andrew Jonathan Smith

aus Manchester, CT - USA

März 2008

Aus dem Institut für Organische und Makromolekulare Chemie
der Heinrich-Heine Universität Düsseldorf

Gedruckt mit der Genehmigung der
Mathematisch-Naturwissenschaftlichen Fakultät der
Heinrich-Heine-Universität Düsseldorf

Referentin:	Prof. Dr. Claudia Staudt
Korreferent:	PD Dr. Manuel M. Lohrengel

Tag der mündlichen Prüfung: 05.05.2008

Some of the results presented in this work were reported in published papers or during scientific meetings:

Publications

B. Bello Rodriguez, A. J. Smith, A. W. Hassel
"Electrodeposition of Gold on Tungsten Nanowires"
J. Electroanal. Chem., in press

S. Milenkovic, A. J. Smith, A. W. Hassel
"Single crystalline Molybdenum nanowires and nanowire arrays"
Journal of Nanoscience and Nanotechnology, in press

A. W. Hassel, V. Cimalla, C. Röhlig, J. Pezoldt, M. Niebelschütz, O. Ambacher, K. Brückner, M. Hein, J. Weber, S. Milenkovic, A. J. Smith
"Nanomechanics of single crystalline tungsten nanowires"
Journal of Nanomaterials, Volume 2008 (2008), Article ID 638947

S. Brittman, A. J. Smith, S. Milenkovic, A. W. Hassel
"Copper Nanowires by an Electrochemical Release from a Directionally Solidified Silver-Copper Eutectic"
Electrochim. Acta **53** (2007) 324-329

A. W. Hassel, A. J. Smith, S. Milenkovic
"Nanostructures from directionally solidified NiAl-W Eutectic Alloys"
Electrochimica Acta, **52** (4) 1799-1804, 2006

Oral Presentations (presenting author underlined)

A. J. Smith, M. Stratmann, A. W. Hassel
"Selective Electrodissolution of Directionally Solidified Eutectic Alloys for "Mass Production" of Metallic Nanowires with Extreme Aspect Ratios"
58th Annual Meeting of the International Society of Electrochemistry
2007.09.09 – 2007.09.14, Banff, Canada

A. J. Smith, S. Milenkovic, A. W. Hassel
"Initial Steps in Handling Single Nanowires"
92. AGEF Seminar "Nanotubes and Nanowires"
2007.04.19, Düsseldorf, Deutschland

A. J. Smith, S. Milenkovic, A. W. Hassel
"Directionally Solidified Nanostructured Materials: Properties and Applications"
International Bunsen Discussion Meeting
2006.11.02 – 2006.11.04, Dresden, Deutschland

A. J. Smith, S. Milenkovic, A. W. Hassel
"Metallic Nanoarrays for Application in Nanoelectronics and Nanosensor Technology"
4th Spring Meeting of the International Society of Electrochemistry
2006.04.17 – 2006.04.20, Singapore

Poster Presentations

A. J. Smith, A. W. Hassel
"Studying and Applying Metallic Nanowires Obtained from Electrochemical Treatment of Directionally Solidified Eutectics"
6th International Symposium on Electrochemical Micro & Nanosystem Technologies
2006.08.22 – 2006.08.25, Bonn, Deutschland

A. J. Smith, S. Milenkovic, A. W. Hassel
"Overview of Nanoscopic Morphologies Accessible Through Electrochemical Processing of Directionally Solidified Eutectic Alloys "
92. AGEF Seminar "Nanotubes and Nanowires"
2007.04.19, Düsseldorf, Deutschland

Εξαιρετικά αφιερωμένο στη Μαρία

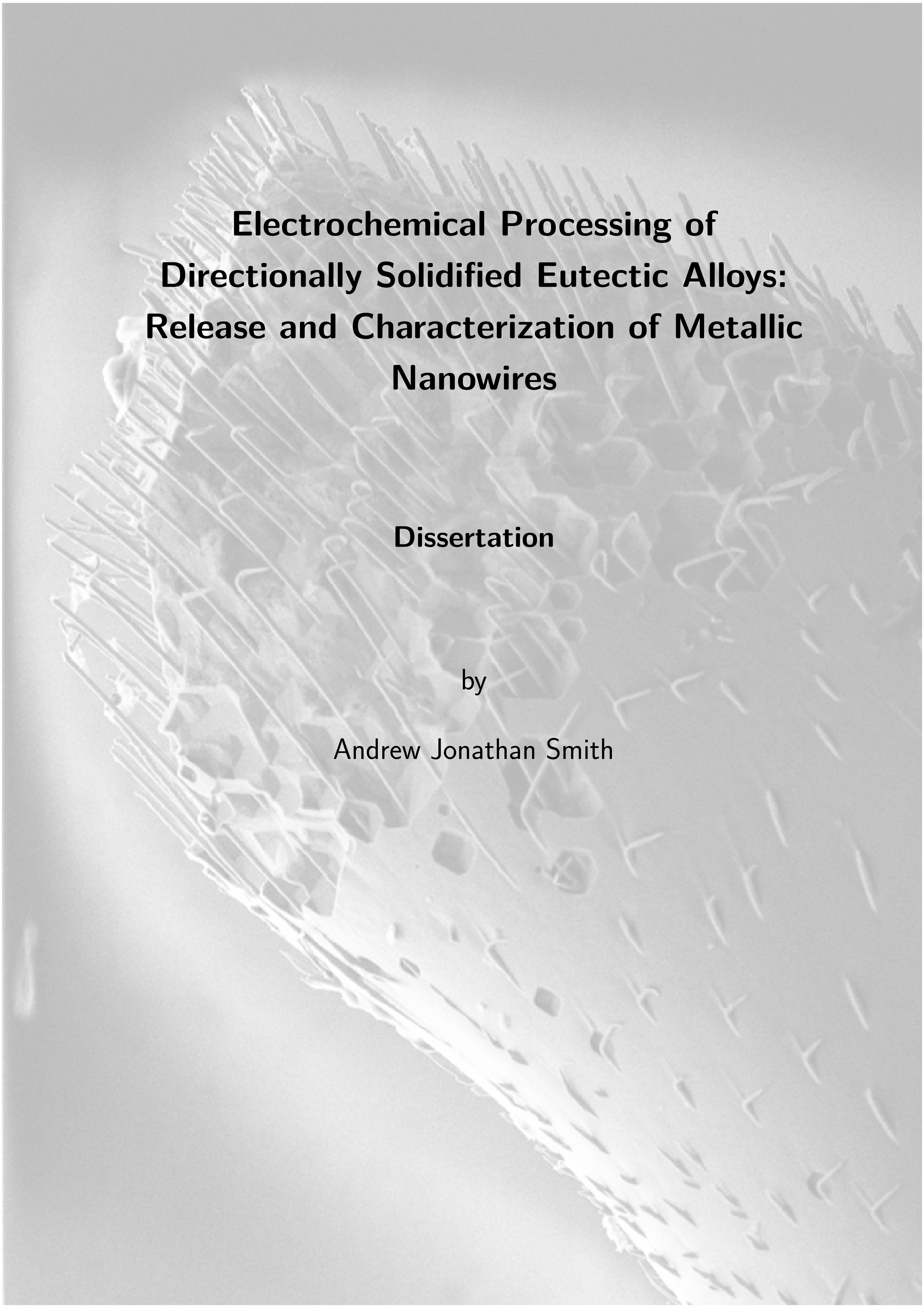

Electrochemical Processing of Directionally Solidified Eutectic Alloys: Release and Characterization of Metallic Nanowires

Dissertation

by

Andrew Jonathan Smith

Acknowledgments

First and foremost I must express my thanks to Prof. Claudia Staudt and PD Dr. Manuel M. Lohrengel for kindly supervising this thesis.

Also, my warmest gratitude goes to Dr. Achim Walter Hassel for his guidance, mentoring, and support during the past eight years.

Of course, I could never have finished this thing without some (actually: a lot of) help. So here goes: Thanks go to Dr. Srdjan Milenković for a seemingly endless supply of samples and smiles, to Dr. Belen Bello-Rodriguez for keeping all of us sane in the lab, to Kirsten Lill for being the best office-buddy ever as well as a good friend.

Very special thanks go to Christian Fenster who has the dubious luck of being my very good friend *and* my colleague at the same time. Thank you for being there.

Over the past two years I was lucky to have some very capable students supporting my work. Thank you Pedro Perezim, Sarah Brittmann, Dana Frankel, and André Abts.

Many thanks also go to my colleagues for helpful discussions and experimental support: Dr. Daniel Sanders and Andrei Ionut Mardare as well as the rest of the “ElKo’s”.

I must also thank the excellent staff at the Max-Planck-Institut für Eisenforschung for their help and support: Andrea Mingers and Daniel Kurz for ICP-OES measurements, Monika Nellessen for guidance using the FIB, Erika Bartsch for TEM measurements, and Ralf Selbach and his very capable crew of craftsmen: Markus Bormann and Robert Thissen, among others, for creatively constructing various widgets and gadgets.

Next I would like to thank the people that are my friends: Andreas Serr, Katharina Gerigk, Niels-Jakob Küttner, Mark Fellmann, Andreia Ioana Popa, and Jana van der Kloet. Thank you, Thank you, Thank you... I wouldn’t have made it without you!

Finally, the most important person in my life: Maria Georgiou. I cannot express the amount of luck and gratitude I feel, knowing that you are there.

The fact that we live at the bottom of a deep gravity well, on the surface of a gas-covered planet going around a nuclear fireball ninety million miles away and think this to be normal is obviously some indication of how skewed our perspective tends to be.

Douglas Noel Adams

Zusammenfassung

Gerichtet erstarrte (quasi)binäre eutektische Legierungen ermöglichen den Zugang zu metallischen Drähten oder Lamellen, die in eine metallische Matrix eingebettet sind. Während des Erstarrens separieren die Elemente der Legierung, so dass reine, einkristalline Phasen entstehen. Die in einem Kristallzuchtofen nach Bridgman durchgeführte, gerichtete Erstarrung kann durch Verändern des Temperaturgradienten sowie der Wachstumsgeschwindigkeit optimiert werden, um nanoskopische Strukturen mit regelmäßiger Anordnung zu erhalten. Die in dieser Arbeit untersuchten Systeme sind NiAl-Mo, NiAl-Re, NiAl-W und Ag-Cu.

Durch die Anwendung elektrochemischer Prozesse können die nanoskopischen Strukturen aus den Materialien herauspräpariert werden. Das selektive Auflösen der Drähte liefert metallische Proben mit regelmäßiger Anordnung nanoskopischer Poren. Diese Poren können als Templat für weitere Präparationsschritte dienen. Ein vollständiges Auflösen der Drähte liefert metallische Nanofilter.

Das Herauspräparieren der Drähte geschieht durch selektives Auflösen der Matrix. Die Nanodrähte sind regelmäßig angeordnet und stehen aufrecht in der Matrix. Die Länge der Drähte ist abhängig von der Ätzdauer und kann präzise eingestellt werden. Die Drähte sind einkristallin und haben auch azimuthal gleiche Orientierungen, so dass jeder Draht eine exakte Kopie aller seiner Nachbarn ist.

Führt man das selektive Ätzen der Matrix fort, bis diese vollständig aufgelöst ist, erhält man freie Nanodrähte. Die Drähte können dann für weitere Untersuchungen bzw. zur Herstellung von nanoskopischen Messsonden verwendet werden.

Der Umgang mit einzelnen Nanodrähten wird durch das Verwenden von mechanisch getriebenen Mikromanipulatoren sowie Piezo getriebenen Nanomanipulatoren in Kombination mit einem hochauflösenden Lichtmikroskop oder einem Rasterelektronenmikroskop mit fokussiertem Ionenstrahl ermöglicht. Weiterhin werden die Manipulatoren für mechanische Untersuchungen an Nanodrähten eingesetzt, die die extreme Flexibilität der Drähte zeigen.

Durch die Kombination von chemischen, elektrochemischen und mechanischen Prozessschritten sowie Mikro- und Nanomanipulation sind Messsonden für Rastertunnelmikroskopie und *in situ* pH-Messungen in extrem kleinen Volumina zugänglich.

Durch Kombination von Drahtarrays bzw. von freien Nanodrähten mit Polymeren können Kompositmaterialien hergestellt werden. Erste Experimente auf diesem Gebiet zeigen, dass die Herstellung einer Vielzahl von Strukturen mit sehr verschiedenen Eigenschaften auf diesem Wege möglich ist.

Abstract

Directional solidification of (quasi)binary eutectic alloys leads to the formation of metallic wires or lamellae embedded in a metal matrix. During this process the alloying elements segregate, resulting in pure phases. Additionally, the solidified material is single crystalline. Optimizing this process by adjusting the temperature gradient and the growth speed in the Bridgman-type crystal growth oven as well as tuning the composition of the employed alloy yields regularly spaced fibrous structures with nanoscopic dimensions. The alloys investigated in this work are NiAl-Mo, NiAl-Re, NiAl-W, as well as Ag-Cu.

Electrochemical processing of the directionally solidified material allows selectively dissolving either the wire or the matrix phase. Dissolving the wire phase leads to the formation of arrays of nano-sized pores, which can be used as templates for further preparation steps. Complete dissolution of the wire phase yields metal substrates with nano-sized channels.

Selective dissolution of the matrix phase exposes the nanowires, yielding arrays of regularly spaced, upstanding nanowires. Variation of the etching duration gives precise control of the length of the exposed wires. As mentioned above, each wire is single crystalline. Additionally, the wires are iso-oriented so that each wire is an exact clone of each of its neighbors.

Further etching leads to the complete dissolution of the matrix yielding free nanowires. These wires can be further processed and used for detailed investigations of the wires' properties as well as for fabrication of nanodevices.

Handling single nanowires is achieved by employing mechanically driven micromanipulators and piezo-driven nanomanipulators in combination with a high magnification light microscope, a scanning electron microscope, as well as a focused ion beam system. The manipulators are also employed for bending tests showing the extreme flexibility of the nanoscopic wires.

By combining a number of chemical, electrochemical, mechanical processing, and manipulation techniques, fabricating devices such as STM or pH probes is possible.

Polymer composite materials are fabricated with both, free wires and wire arrays. Initial experiments show that a large number of different structures with a wide range of novel properties are obtainable by combining nanoscopic metal wires with polymer materials.

Contents

1 Introduction

The concept of a nanoscopic technology was first described in a lecture given by Richard P. Feynman at the annual meeting of the American Physical Society on December 29$^{\text{th}}$, 1959 titled “There’s Plenty of Room at the Bottom.” The lecture was published in *Engineering and Science* in 1960 [1]. The term “nanotechnology” was initially defined by Tokyo Science University Professor Norio Taniguchi in 1974 [2]: “‘Nanotechnology’ mainly consists of the processing of, separation, consolidation, and deformation of materials by one atom or by one molecule.” This definition was later broadened to include all techniques and technologies that allow studying, characterizing, and manipulating nano-sized objects, i.e. objects with sizes in the range of some nanometers to some hundreds of nanometers. Further, the manufacture of nano-sized devices, utilizing the unique effects of the nano-sized world, are rapidly moving into the focus of current research. The unique effects observed in the nano-regime are a direct result of the decreased dimensions of objects, showing a non-linear transition from bulk properties to the emergent properties of nanostructures. These properties are due to the effects of “size confinement” or “quantum confinement”, where a certain material property is constrained due to the small dimensions of the sample. Thus, the term “nanotechnology” also includes all nano-sized devices, probes, and processes (e.g. surface coatings) that are based on taking advantage of nano-size effects.

The establishment of cluster physics [3] and the development of the scanning tunneling microscope (STM) [4] were the two decisive factors in initiating research in the nano-regime.

Cluster physics deals with the interaction of multiatom particles, while neglecting molecule chemistry. The interest in clusters was sparked by the fact that the physical properties of a bulk material change when the amount is reduced to the size of clusters. In an attempt to determine the minimum amount of material necessary for a given property to emerge, *ab initio* calculations are performed.

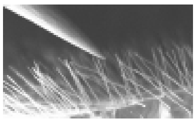

These processing-intense calculations are made possible by the reduction of the number of involved atoms. The corresponding synthesis of nanoscopic structures combined with measurements of their properties allows for a direct comparison of theoretical calculations and experimental results.

The development of scanning tunneling microscopy was honored by the Nobel Prize in Physics being awarded to its inventors Gerd Binnig and Heinrich Rohrer in 1986. The technique is based on probing the density of states of the surface under investigation. This is done by bringing a conductive tip close to a conducting or semi-conducting sample and applying a voltage bias between the two; when the distance is sufficiently small, quantum tunneling occurs. The tunneling current is a function of the local density of states, so that variations of the current can be translated into an image [5]. In particular research performed by Kolb *et al.* should be mentioned, which utilizes scanning tunneling microscopy for well directed deposition of metal clusters [6].

The past twenty years have seen the development of a wide range of derived techniques, most importantly atomic force microscopy (AFM). Bonnell and Shao published a review of scanning probe techniques in [7]. In addition to the development of new technologies, the improvement and easy accessibility to scanning electron microscopy (SEM) has greatly influenced research in the sub-micro and nano fields.

Fabrication of nano-structured materials is possible through many different routes. A review of fabrication methods based on interfacial chemical reactivity is given by Khomutov *et al.* in [8]. A further publication, focusing on inorganic, polymeric and composite nano-structured films is given in [9]. The scanning probe methods mentioned above can be adapted from being purely observational tools to be used as a medium for the fabrication of nano-structured surfaces. An overview of these fabrication applications is given by Garcia *et al.* in [10].

Next to the fabrication of carbon nanotubes and other carbon nanostructures which have been extensively researched in recent years and are still of great interest today, another field of nanoresearch producing nano-sized wires is focused on silicon nanostructures.

Silicon nanowires can be grown thermally with the help of various catalysts, such as carbon or gold nanoparticles dispersed on a silicon substrate, yielding wires with diameters ranging from some nanometers up to hundreds of nanometers [11–14]. Using this method, silicon - metal composite wires are also obtainable [15]. Other methods for producing silicon nanostructures include laser exposure combined with chemical etching [16], sulfide-assisted growth [17, 18] as well as a range of chemical vapor deposition (CVD) methods [19]. These also incorporate various catalysts and yield branched structures, doped wires, or other silicon-based nanostructures [19–21].

Silicon nanostructures are investigated intensively due to the application of silicon in the semiconductor industry. The challenge of making computing devices ever smaller is driving research in the direction of nanoscopic logic devices. Carbon nanotubes as well as silicon nanowires and other semiconducting materials are used for manufacturing nano-sized logic devices [22–27]. A completely different approach was taken by Sakai *et al.* in producing conductive wires and nanotransistors from organic precursors [28].

Other nano-sized devices such as field emitters, light emitting diodes, field effect transistors, and other semi conductor materials have also been realized using various methods including laser assisted growth, vapor-liquid-solid (VLS) thermal growth, metal organic vapor phase epitaxy (MOVPE), and photolithography [29–33].

As with many nanostructures, the changes in the mechanical properties are of great interest. Again, the bulk properties of certain materials do not translate directly to the nanoscopic regime; rather, vastly different behavior is often found. The temperature dependence of the mechanical properties of silicon dioxide nanowires was investigated by Namazu and Isono in [34].

The third type of nanostructures under intense study is the field of zinc oxide nanowires and nanonetworks. A comprehensive review of zinc oxide nanostructures was published by Wang in [35]. An example of various dendritic 2D web-like structures can be found in [36]. More recently, investigations of the optical and thermal properties of zinc oxide nanowires show that the nanostructures have improved thermal conductivity as well as an increased band gap, leading to stronger absorptions in UV-VIS investigations [37].

Electrochemical approaches are also widely employed for the fabrication of nanostructured materials. Scaling down traditional electrochemical techniques has greatly enhanced the capabilities of electrochemical nanoproduction methods as described in a review by Schultze and Bressel [38].

One of the earliest electrochemical approaches to fabricating nano-structured materials was the anodic oxidation of aluminum and other valve metals in aggressive media. These experiments yielded honey comb structures of alumina with pore sizes down to tens of nanometers and relatively high aspect ratios of approx. 150 [39–41]. Optimizing these procedures allows the fabrication of extremely well ordered structures with round, square, or triangular morphologies [42].

Due to the ease of manufacturing well ordered, high aspect ratio alumina pore arrays, these structures are widely used as templates for the production of other metallic or composite nanomaterials. These materials - including silver, gold, cobalt, nickel, and copper - are deposited inside the pores using either electrolytic or electroless deposition methods [43–47]. A review of these methods is given by Piao *et al.* in [48]. Other applications, including the fabrication of nano-sized pillars as well as composite materials with unique magnetic properties were investigated by Mozalev, Pirota, Lin, and Kato [49–52].

Another method for fabricating nanopore arrays is ion track etching. This technique is based on irradiation of polymer or glass substrates with swift heavy ions followed by chemical etching of the ion tracks, yielding arrays of nano-sized pores. These pores are then used as templates for the deposition of other materials using various chemical and electrochemical methods [53–55].

Electrochemical approaches also include precipitation of various metals by cathodic polarization of a substrate in an appropriate electrolyte. Many common metals can be deposited from aqueous electrolytes, but deposition of aluminum or titanium is only possible from organic electrolytes since they deposit at potentials much lower than that needed for the nucleation of hydrogen [56]. The use of electrochemistry as a tool for tuning the properties of precipitated nanostructures is demonstrated by Bai and Hu in [57]. Manufacturing nanoscopic structures with very high active surface areas was achieved by Ji and Searson by depositing a two component alloy into an alumina template. Subsequent removal of the almunia as well as one of the alloying elements yielded nanowires with a porous nanoscopic substructure [58].

Many other material systems and techniques for preparing nanostructures are being pursued. Among these, just to name a few, are the production of germanium dioxide nanowires by physical vapor deposition (PVD) [59], alternating gallium arsenic / gallium phosphorus wires using VLS [60] as well as arrays of zirconia nanotubes filled with copper or nickel yielding nano-sized core-shell structures with enhanced physical properties compared to bulk materials [61].

Chemical fabrication of metallic nanostructures is also possible using various methods; among these are the synthesis of gold nanorods and nanoparticles of different shapes from organic precursors. A review of recent results in this field is given by Alkseeva in [62]. Utilizing other techniques such as microwave irradiation, sonochemical treatment, and electrochemical procedures allow for the preparation to a multitude of nano-sized gold structures [63–69].

Recently, single crystal gold nanobelts were prepared via directional eutectoid decomposition followed by selective chemical etching [70, 71]. The preparation of these nanostructures is similar to directional solidification of eutectic alloys which is the method used for preparing the materials investigated in this work. The fact that self-organized micro and nanostructures are obtainable from eutectic alloys has been known since the mid 1960s. The novel optical, electronic, and magnetic properties of these alloys were investigated in great detail [72]. The nanostructures fabricated by this method consist of regularly spaced fibers or sheets embedded in a metal matrix. Electrochemical techniques can be applied to directionally solidified eutectics to prepare various nanostructures by tuning the (electro-)chemical environment to selectively dissolve specific phases [73, 74].

The results of electrochemically processing directionally solidified eutectic alloys as well as the applications of the obtained structures using further tailoring, manipulation, and the formation of composites are the topic of this thesis.

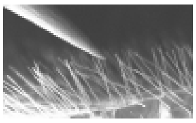

2 Objectives

Before discussing the theoretical background of the fabrication and processing steps involved in preparing nanoscopic structures from directionally solidified eutectic alloys as well as describing the obtained results, a short overview of the goals and objectives of this work will be given in this chapter.

The schematic in fig. 2.1 shows the various routes of interest for processing the directionally solidified alloy. There are two fundamental routes that can be taken: selectively dissolving the matrix phase (left and middle branch in fig. 2.1) or selectively dissolving the fibrous phase (right branch in fig. 2.1).

Dissolving the fibrous phase leads to the formation of arrays of regularly spaced nanopores. Processing ultrathin samples in this manner yields metal substrates with nanochannels.

The most basic approach to obtaining nanowire structures is to subject entire samples to conditions that will selectively etch the matrix. This process will yield arrays of nanowires standing upright whose lengths are controllable, depending on the processing time. Continuing this process until the matrix is completely dissolved yields free nanowires which can be processed further, e.g. for the fabrication of nanowire - polymer composites.

Applying a polymer to the "forests" obtained from partial matrix removal produces ordered composite materials as well as polymer membranes with nanosized channels.

Using various microelectrochemical techniques, the processing of the material can be localized yielding a number of different structures. Etched pits crossed by nanowires, bridged structures as well as samples tipped with single nanowires are of interest.

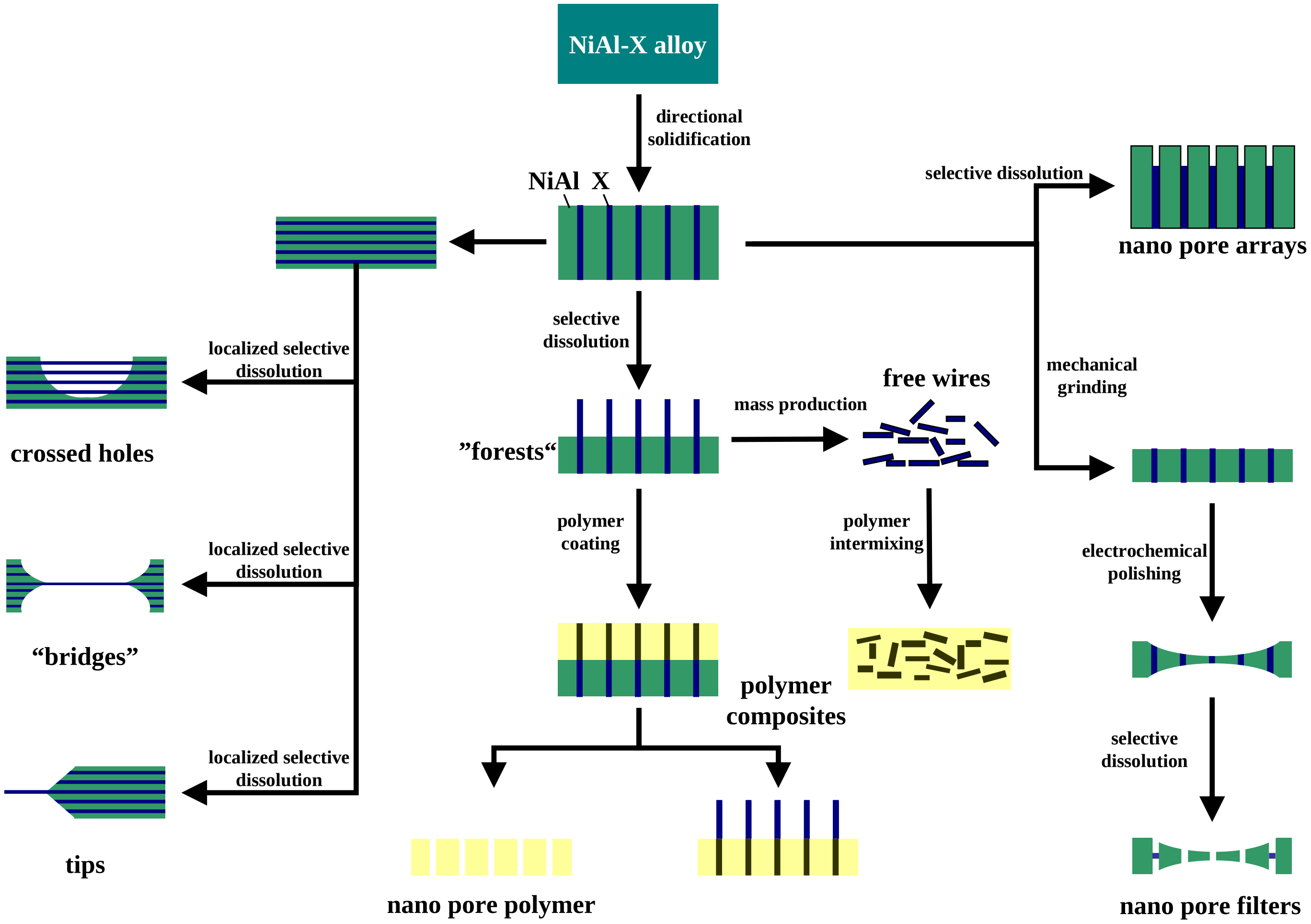

Figure 2.1: Schematic overview of the processing steps and the resulting morphologies.

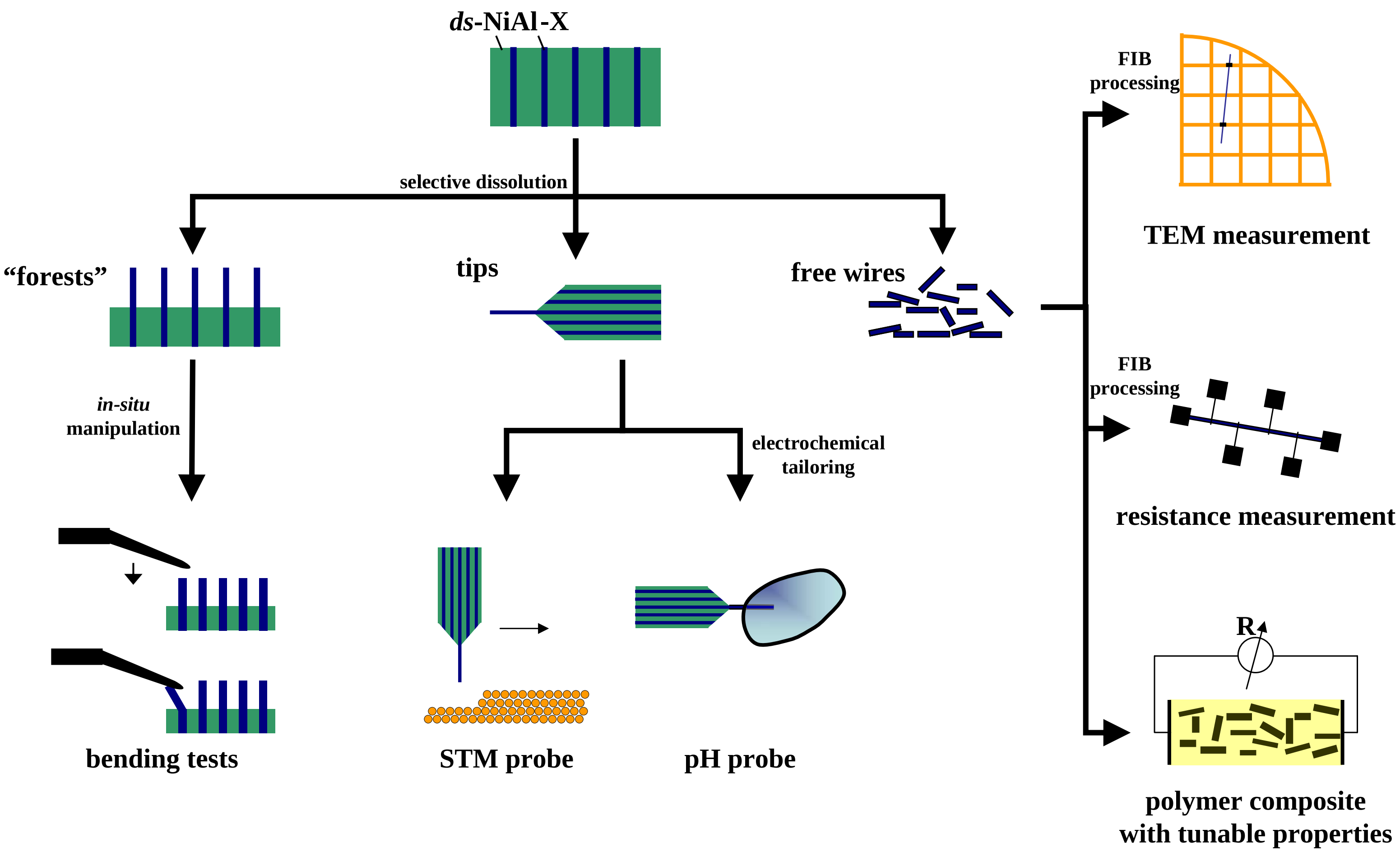

Figure 2.2: Schematic overview of the applications and other experimental procedures performed.

Figure 2.2 gives an overview of the investigations performed on the obtained nanoscopic structures and the applications derived from these structures.

Upright nanowires can be individually subjected to bending tests using piezo-driven nanomanipulators. The same manipulators are used to mount free wires to different substrates for transmission electron microscope (TEM) analysis as well as electrical measurements.

Using pointed sticks of directionally solidified material with single nanowires protruding from the tips allows single nanowire probes to be handled manually. These probes were employed as scanning tunneling microscope (STM) tips and, after electrochemical processing of the nanowire, as pH sensitive nanoprobes.

Finally, initial steps in elucidating the properties of nanowire - polymer composite materials were investigated by mixing different amounts of free nanowires with polyimide copolymer and measuring the resulting material properties.

3 Theory

3.1 Eutectic Materials

Mixing two different substances of a eutectic system in the correct proportions leads to a minimum in melting temperature. Precisely this ratio of one component to the other is called the eutectic composition. So, in general it can be said that a eutectic is a mixture of two or more components that are mixed in such quantities as to yield the lowest possible melting temperature. The first experiments on this phenomenon were carried out in 1864 by Rüdorff [75]. The word “eutectic” was coined by Guthrie in 1884 [76]. It is derived from the Greek word “eutektos” meaning “most fusible” [77]. The first correct description of the underlying mechanisms was given by Vogel in 1912, and Straumanis and Brakss̆ performed directional solidification in 1935 [78, 79]. The theory of eutectic growth was established by Jackson and Hunt in the mid 1960s [80].

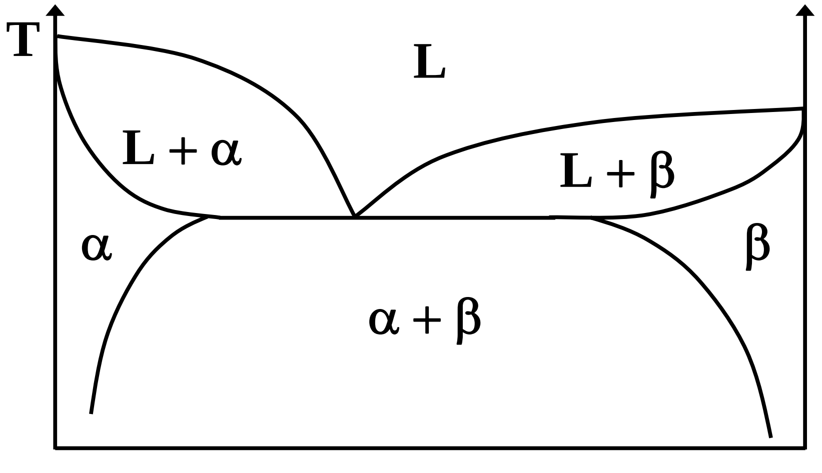

Figure 3.1: Schematic of a eutectic phase diagram.

In order to better understand eutectics, a short description of phase diagrams is necessary [81]. The phase diagrams employed here are thermodynamic diagrams of temperature as a function of the composition. They show stable (or metastable) equilibria of co-existing phases. One should keep in mind that they are simplified - as they are drawn for conditions consisting of constant pressure and only one changing variable (the composition) - but give a good starting point for further study. The point in the phase diagram of a eutectic system where the liquidus and solidus lines intersect is called the eutectic point.

The eutectic is an invariant equilibrium wherein the composition and the temperature of the system are unambiguously defined for a given value of pressure. According to the Gibbs phase rule, any system with N components which is an invariant equilibrium must consist of $N + 1$ phases.

$$F + P = N + 2 \qquad \text{eq. (3.1)}$$

F : number of degrees of freedom
P : number of phases
N : number of components

It follows that a binary eutectic is defined by eq. (3.2) which states that the melt L transforms into two crystals α and β (see fig. 3.1).

$$L = \alpha + \beta \qquad \text{eq. (3.2)}$$

One of the main features of eutectics is the fact that they contain an extremely high amount of interfaces. These interfaces can be between two phases or between two crystals of the same phase but with different crystallographic orientations. A typical solidified eutectic contains approx. $1\,\mathrm{m}^2$ of interface per cm^3 of material [82].

Most of the eutectic systems employed in this work are quasi-binary alloys. As the term “quasi-binary” indicates the system - consisting of three metals - behaves like a binary one, e.g. the liquid is in isothermic equilibrium with two solid phases ($L = A_xB_y + C$). The alloys used were: NiAl-Mo, NiAl-Re, and NiAl-W [83–86]. These eutectic composite materials are especially interesting due to their favorable mechanical properties at high temperatures (even close to their melting points). Another binary eutectic studied was Ag-Cu [87, 88]. Copper nanostructures are of great interest due to the fact that copper has already widely replaced aluminum in integrated circuits, moreover the use of Cu_2O in the next generation of metal oxide semiconductors gives merit to the investigation of these structures [89, 90]. The interest in silver originates from its excellent electrical properties and the desire to examine these properties at very low dimensions [91–93].

3.2 Directional Solidification

In order to obtain self-organized nanostructered material from the eutectic alloys described previously, it is necessary to directionally solidify these alloys. This is typically performed using a Bridgman type oven (fig. 3.2). The oven consists of two zones - a hot zone and a cold zone. The sample is placed in the hot zone and the alloy is allowed to melt completely. Then the sample is lowered into the cold zone at a well defined, constant speed. This speed, as well as the temperature gradient between the hot and cold zones, are two factors that influence the nanostructure. Therefore these are two of the parameters which can be adjusted to tune the system to yield the desired nanostructure.

As stated in section 3.1 a special feature of eutectic materials is the abundance of interface area. Interfaces are always high energy regions; therefore any system will adapt in such a way as to minimize the surface energy and develop the most energetically beneficial crystal surfaces. This is achieved by coupled growth of the phases in addition to the selection of appropriate crystal surfaces mentioned above. The range of orientation mismatch between the two phases in which the energy is minimal is very small so that the slightest crystallographic mismatch leads to a great increase in surface energy. This fact affects the formation of a stable crystallographic relationship between the phases [82, p. 53] [95] (see section 3.3).

Another important factor during the solidification of eutectics is nucleation. In the initial stages of growth, the orientation relationship among the phases is important as this relationship determines the "perfectness" of the microstructure. It is important that nucleation occurs in a controlled manner. During growth, it is also important to prohibit nucleation in order to obtain a well-ordered structure [96].

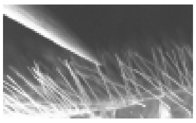

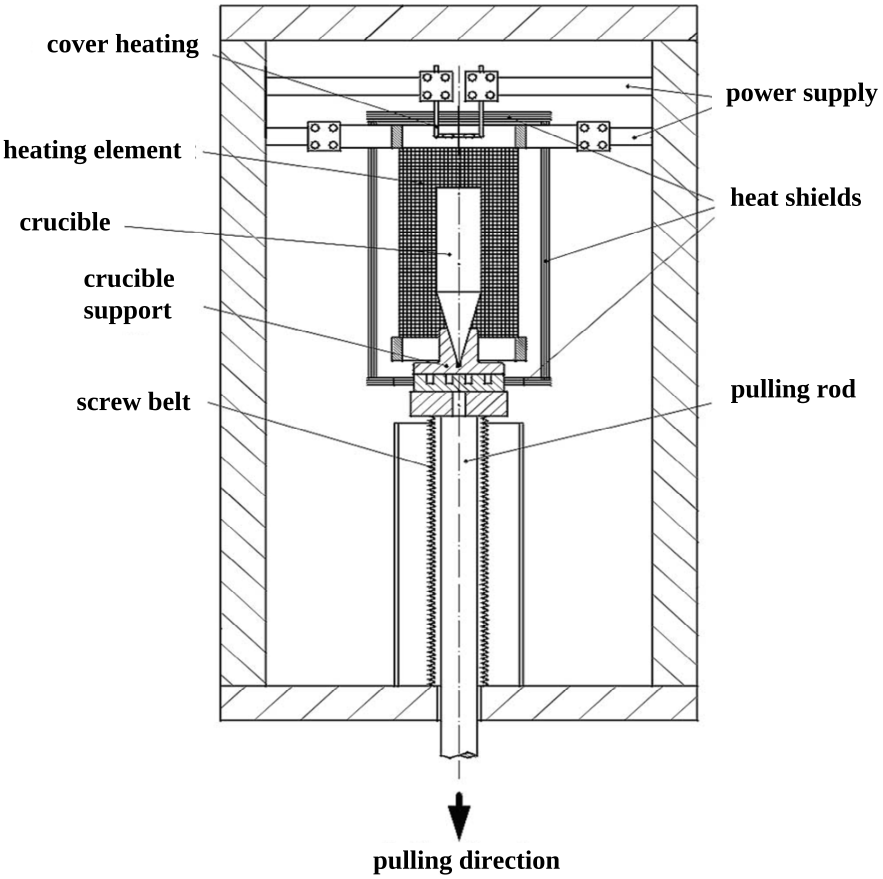

Figure 3.2: Bridgman-type oven for directional solidification, from [94].

When a melt solidifies right after dropping below its melting temperature, the solidification mechanism involved is heterogeneous nucleation. Since heterogeneous nucleation occurs at impurities in the melt or at imperfections on the inside of the crucible, the probability of nucleation is not the same throughout the system. When solidifying a binary eutectic, two phases must precipitate from a homogeneous melt; two nucleation sites are necessary before coupled growth can occur. Since the undercooling necessary for nucleation is different for each of the eutectic's phases it is probable that one of the phases will nucleate first. The liquid will then be enriched with the element with a higher nucleation threshold, thus increasing the nucleation probability of this element. Finally equilibrium is reached and both phases precipitate simultaneously [82, p. 67].

The two constituents of a binary eutectic alloy can lead to microstructures with a large variety of geometrical combinations. If both phases possess a low entropy of fusion, the eutectic structure is usually regular (either fibrous or lamellar). Jackson differentiated between “faceted” and “non-faceted phases”. “Faceted” phases have preferential crystallographic growth directions associated with atomically smooth solid / liquid surface facets. “Non-faceted” phases solidify with complete crystallographic isotropy due to an atomically rough solid / solid interface [80, 97].

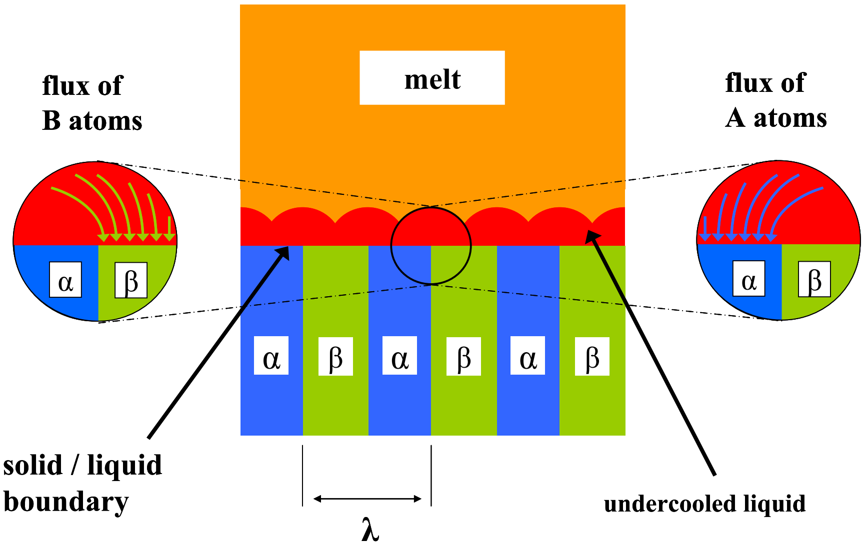

Figure 3.3: Schematic representation of the directional solidification process in the Bridgman-type oven.

In the case of the alloys used in this study, precipitation occurred according to the mechanism of diffusion-coupled growth. Figure 3.3 shows a schematic representation of a sample undergoing directional solidification. The sample is lowered from the heated zone at the top into the cooled zone at the bottom at a certain speed. Therefore the solidification front can be seen as traveling upwards at the same speed. The interfaces between the precipitated phases are perpendicular to the solid/liquid interface and parallel to the growth direction [98].

Precipitation occurs in the undercooled liquid right at the solidification front. The solid phase α rejects the B atoms just as the solid phase β rejects the A atoms due to mutual insolubility and minimization of surface energy during crystal growth. The rejected atoms diffuse along the concentration gradient to the nearest favorable site and then precipitate. Thus, the phases “feed” each other during the diffusion-coupled growth. This is the underlying self-organization mechanism. In this manner, either fibrous or lamellar structures are obtained depending on the volume fraction of the phases. As an approximate guideline, a volume fraction above 0.3 produces lamellae, a volume fraction below 0.3 produces fibrous structures [98, p. 95][97]. The eutectics chosen in this work all have volume fractions well under the threshold value of 0.3 (except for the silver-copper system, see section 4.2.2, page 40), so that the experiments yielded well ordered arrays of nano-sized metallic wires. In the case of Ag-Cu, the composition was very close to the threshold value, therefore producing lamellae and wires side by side [99].

Also, it should be mentioned that a precise control of the temperature gradient in the Bridgman-type oven as well as the growth speed affect the diameter and spacing of the wires. However, due to the fact that the volume fraction of the eutectic alloy is fixed, these two variables are linked. Depending on the chosen conditions, smaller, densely packed wires are obtained or larger wires with wider spacing are produced, depending on the chosen conditions.

Usually it is desirable to obtain the best possible microstructure during solidification. When dealing with eutectics, the solid phase consists of two interpenetrating crystals (a so-called duplex crystal). In order to reduce the abundance of faults and imperfections during growth, it is important to consider the following factors:

- The shape of the solidification front should be as flat as possible (may be disturbed by the macroscopic curvature of the front due to undirected heat extraction or convection).
- Fluctuations of the diffusion field as well as the convection field (unsteadiness in the crucible motion, fluctuations in the heat extraction due to temperature changes in the oven, turbulence just in front of the interface)

The most important factors for successfully performing directional solidification are:

- crucible material and shape
- direction of heat extraction
- temperature gradient right in front of the solid-liquid interface
- convection in the melt

A suitable crucible material for melting high temperature eutectics is corundum. It must possess a high chemical stability as well as being able to withstand the high melting temperatures of the alloys. The shape of the crucible should be cylindrical and relatively small as to allow for a uniform heat extraction.

Samples that solidify isotropically (non-directionally) can only dissipate heat radially which leads to a negative temperature gradient at the solidification front. This explains why the primary precipitates are always unstable and form dendrites. During directional solidification a positive temperature gradient is maintained at the solidification front at all times, virtually eliminating interface instabilities and nucleation at the liquid-solid interface.

It is essential for growth to occur at a suitable speed. The maximum solidification speed directly influences the microstructure; it can be seen as one of the most important control parameters for directional solidification. The speed at which the sample is drawn through the temperature gradient is limited by the sample geometry. During solidification, all heat must be extracted at the solidification front. If the speed is too high, the value for the temperature gradient will cease to be positive leading to the problems discussed above. At the same time, the growth speed affects the size and spacing of the microstructure. Therefore, it is important to adapt the sample diameter to obtain the desired microstructure, i.e. if the aim is to obtain smaller fibers necessitating a high growth speed, the sample diameter should be decreased to ensure rapid and uniform heat extraction [82, p. 162 et seqq., et sqq.].

The crystal growth is determined by the cooling speed $\dot{T}$ (see eq. (3.5) at the solidification front. The cooling speed is in turn determined by the temperature gradient G - as mentioned above - in combination with the solidification speed v:

$$G = \frac{\mathrm{d}T}{\mathrm{d}d} \tag*{eq. (3.3)}$$

$$v = \frac{\mathrm{d}d}{\mathrm{d}t} \tag*{eq. (3.4)}$$

leading to:

$$\dot{T} = \frac{\mathrm{d}T}{\mathrm{d}t} = G \cdot v \tag*{eq. (3.5)}$$

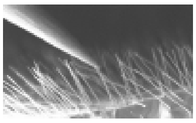

where T is the temperature, t is the time, and d is the distance between the hot and cold zones.

The maximum growth speed can be estimated by adding the diffusion constant D of the material in question, leading to eq. (3.6) where the maximum speed of the sample v_{max} through the temperature gradient G is determined by the ratio of the gradient multiplied by the diffusion constant and the temperature difference between hot and cold zones, ΔT:

$$v_{max} \cong \frac{G \cdot D}{\Delta T} \qquad \text{eq. (3.6)}$$

Finally, convection in the melt affects the transport of both heat and matter and therefore also affects the solidification conditions. In general, the main causes for convection in melts are:

- temperature gradients and concentration gradients
- precipitation of solid, liquid, or gaseous phases of varying densities
- changes in volume during phase transition
- external forces (such as electromagnetic fields, stirring)

The most important of these factors is the first one, pertaining to density shifts in the material due to the mentioned gradients. Precipitations and volume contraction/expansion do not pose problems during directional solidification of eutectics. Applying external fields can help control convection during processing.

During eutectic solidification, thermal convection is primarily involved and constitutional convection can be disregarded. Again, the crucible geometry is crucial for directional solidification as it is possible to influence convection by adjusting the crucible shape and positioning.

Applying external forces such as magnetic fields can help suppress convection. In other cases, rotating the sample can induce coriolis forces that will also influence convection in the melt [82, p. 176 et seqq., et sqq.].

More details on directional solidification and diffusion-coupled growth can be found in the literature. Recent publications include work done by Liu and Elliot [100], an overview by Böttinger *et al.* [101] as well as papers by Cadirli *et al.* [102], Hassel *et al.* [73], and Milenković *et al.* [103].

3.3 A (very short) Excursion into Crystallography

Knowledge of the crystallographic nature of a material's surfaces is useful for understanding its chemical reactivity, mechanical stability, etc. In order to discuss the crystallography of the investigated materials, a short description of crystallography and crystallographic nomenclature will follow.

A crystal is defined as a material whose atomic constituents have a long range order in all three dimensions forming a lattice. To describe the structure of the crystal, it is sufficient to know the structure of the smallest ever-repeating unit cell as well as the length and direction of the three vectors that describe the distances between the unit cells. The lattice constants *a, b, c* are given by the norm of the three basic vectors as well as by the three angles α, β, γ between the vectors. The positions of the atoms in the unit are designated by using the coordinates *x, y, z* which are fractions of the lattice constants (see fig. 3.4) [104].

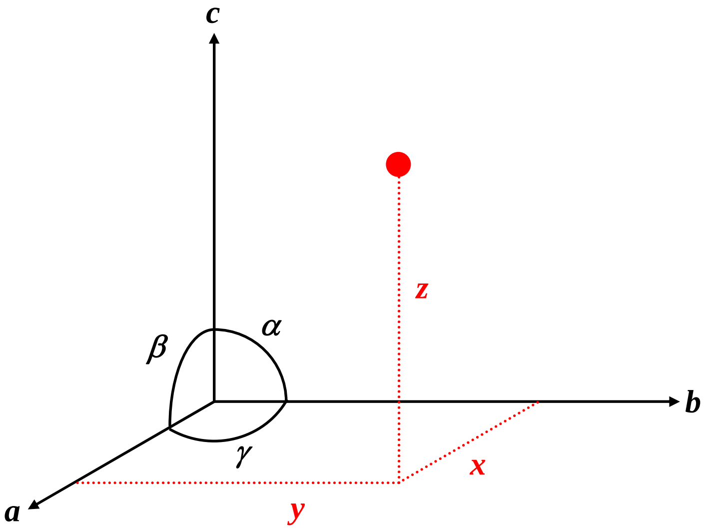

Figure 3.4: Describing crystal lattice unit cells and fractional atomic coordinates.

Furthermore, the so-called Miller Indices are used to characterize crystal surfaces. These indices are derived from arbitrarily placed imaginary planes that intersect with the atoms of the crystal. Each of these planes is stacked among parallel planes so that each atom in the unit cell is contained within the array of planes. The indices are determined by choosing the plane closest to the origin of the unit cell and locating its intersects with the axes of the unit cell. The indices are given as the reciprocal values of these intersects (hkl). If one of these indices is zero, then this means that the intersect lies in infinity, resulting in a plane which is parallel to that axis. Figuratively speaking, the Miller Indices give information on what direction the crystal is being viewed from (fig. 3.5).

As indicated in section 3.2, the relationship of both components' crystal structures to eachother is an important factor during diffusion-coupled growth. In fact, "[the] extreme regularity of both the cross-sectional shape and the distribution of phases in many *in situ* composites suggests that there must be preferred orientation relationships between the constituent phases" [105, p. 95]. This assumption is supported by the idea that interfaces with good crystallographic orientation relationships will have low boundary energies between the phases [106].

Straumanis and Braksš also showed that microstructure of the solidified eutectic is related to a preferred crystallographic orientation [79]. The energy of the grain boundary between crystal grains depends on the orientation relationship of the two grains as well as the orientation relationship of the boundary itself. Therefore, the relationship of two grains to each other is defined by five degrees of freedom: three degrees from the orientation of the grains to one another and two degrees from the orientation of the boundary with respect to the two grains [107–109]. It was shown that low energy interfacial planes lead to stable growth of organized microstructures. Also, Kraft [110, 111] found that interfaces between different phases with widely spaced, densely packed planes and low energies should yield stable growth [112, 113].

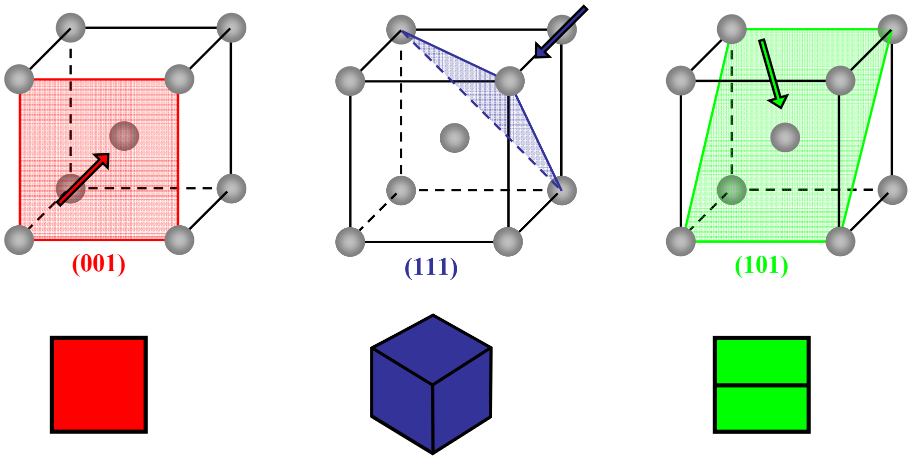

Figure 3.5: Miller indices for describing the different crystallographic planes.

Investigations of the development of certain crystallographic relationships during directional solidification of eutectics have shown that anything from strict epitaxial to completely independent growth can occur depending on the system. The quasi-binary alloy NiAl-Mo shows a unique epitaxy and is characteristic of eutectic alloys with phases of similar crystal structures. The lattice mismatch is accommodated by dislocations at the interfaces between the phases. Depending on this mismatch, the morphology of the resulting microstructure is different. The closest extensively studied related system is NiAl-Cr, where Walter *et al.* [114–116] found that the lattice parameter of Cr is smaller than that of NiAl. However, additions of other metals can increase (Mo, V, W) or decrease (Fe, Cr) the lattice parameters. Exceeding the lattice parameter of NiAl causes the growth of faceted structures (rods and lamellae) instead of round rods produced using the basic alloy [105, 117, 118].

The structure of NiAl is given in fig. 3.6. It "possesses the ordered cubic B2 (space group Pmgm, CsCl prototype) crystal structure, which consists of two interpenetrating primitive cubic cells, where Al atoms occupy the cube corners of one sublattice and Ni atoms occupy the cube corners of the second sublattice" [83]. As can be seen from the lattice constants listed in fig. 3.6, the alloy is somewhat denser than the individual materials. It has a melting temperature of over 1600°C [119] which is high compared to the melting temperatures of Ni and Al (1455°C and 933°C, respectively) [120].

The crystal structures of NiAl and NiAl-alloys were investigated in great detail by various authors. Recently, one prominent method for these investigations has been atomic probe field ion microscopy (APFIM). In this method, a thin needle of the material of interest is placed in an evacuated chamber with a screen on one side. A low concentration of an "imaging gas" is injected into the chamber and an electric field is applied. The gas molecules drift around the chamber - when they touch the needle they are immediately charged and subsequently accelerated toward the screen. The molecule's trajectory is affected by the facet the gas molecule hits. This creates a pattern of spots on the screen from which the crystallographic parameters can be determined [121]. The investigation of NiAl-Re by Deges *et al.* showed that the Re atoms inhabit Ni sites in the alloy [122]. The NiAl-Cr alloy as well as other intermetallic NiAl compounds were investigated by Fischer *et al.* and Liu *et al.* [123, 124]

An important fact to note is that, as mentioned above, the chemical and electrochemical behavior of certain materials is dependent on the crystallographic

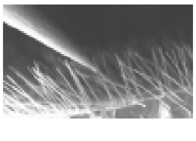

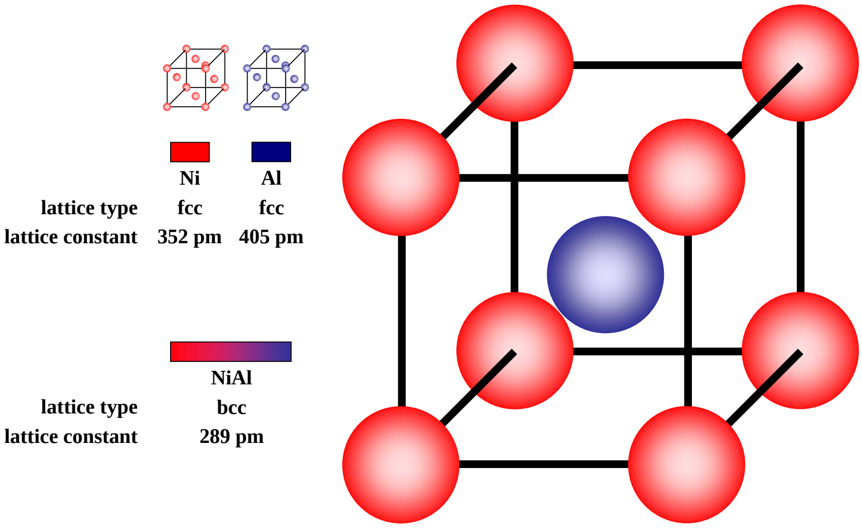

Figure 3.6: Crystal structure of Ni, Al and NiAl.

nature of the exposed surface. Sometimes a preferential etching of a certain crystallographic plane will lead to unusual surface morphologies as shown in fig. 3.7.

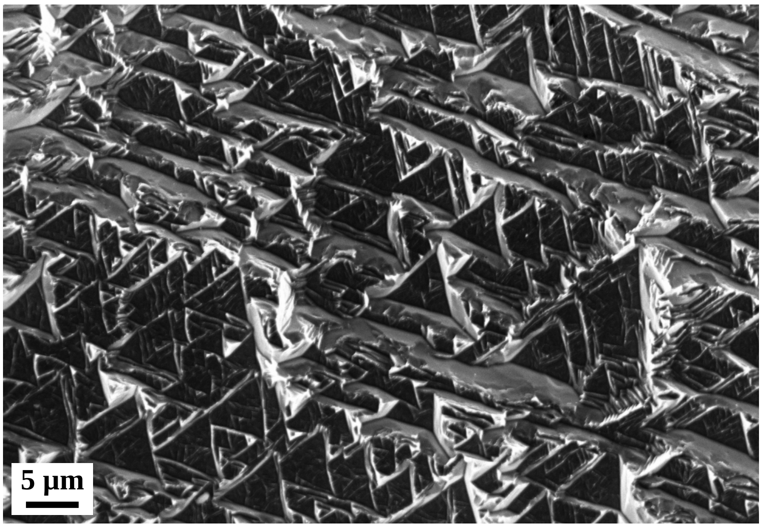

Figure 3.7: (111) surface of a NiAl sample exposed to 1 M HCl at 200 mV SHE for one hour.

3.4 Electrochemical Processing

After dealing with the theoretical aspects concerning the fabrication and growth of samples with self-organized, nanoscopic structures, it is time to turn to the electrochemistry involved in exposing these structures.

The structures obtained through directional solidification (*ds*) consist of two phases. Differences in their chemical and electrochemical properties were utilized in order to selectively dissolve either of the phases, while leaving the other one intact. This was mainly achieved by choosing and applying chemical and electrochemical conditions that would passivate one phase while aggressively corroding the other.

3.4.1 Electrochemistry Basics

Electrochemistry is a branch of chemistry that focuses on the reactions which take place at electrode surfaces in contact with an electrolyte. The electrode is typically a metal or semiconducting material. Typical electrolytes are aqueous solutions of salts (e.g. KNO_3), although non-aqueous liquids are also used in some cases. The main thrust of electrochemical research is the study of electron transfer reactions (ETR) and ion transfer reactions (ITR) at the interface between the electrode and the electrolyte.

From thermodynamics it is known that the Gibbs free energy ΔG_r^0 is equal to the standard potential multiplied by the number of electrons transfered n and the Faraday constant F. The free reaction enthalpy is calculated from the standard free formation enthalpies $\Delta G_{f,x}^0$:

$$\Delta G_r^0 = \Delta G_{f,products}^0 - \Delta G_{f,reactants}^0 \qquad \text{eq. (3.7)}$$

$$E_0 = \frac{\Delta G_r^0}{n \cdot \mathrm{F}} \qquad \text{eq. (3.8)}$$

The Faraday constant F is in turn derived from the elemental charge e (the charge per electron: $1.602 \times 10^{-19}\mathrm{C}$) multiplied by Avogrado's number $\mathrm{N_A}$ (the number of particles to a mole: $6.023 \times 10^{23}\mathrm{mol}^{-1}$) yielding a value for F of $96\,485.34\,\mathrm{C} \cdot \mathrm{mol}^{-1}$.

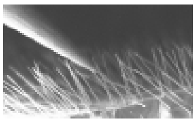

By applying the laws of chemical potential and adding the electrical work necessitated by the presence of differently charged ions, next to an excess or a depletion of electrons in an electrode inserted to an electrolyte, the processes at the electrode/electrolyte interface can be described and the Nernst equation can be derived [125, p. 67 ff.]:

$$E = E_0 + \frac{\mathrm{R} \cdot T}{n \cdot \mathrm{F}} \cdot \ln \frac{a_{ox}}{a_{red}} \qquad \text{eq. (3.9)}$$

E : electrode potential
E_0 : standard potential for the reaction
R : ideal gas constant
T : absolute temperature
n : number of electrons transferred
F : Faraday constant
a_{ox} : activity of the oxidized species
a_{red}: activity of the reduced species

Having mentioned this, it is important to note that it is not possible to directly measure the potential difference between an electrode and an electrolyte, as the measuring device would have to be in contact with both phases simultaneously. Inserting any probe into the system causes a new phase boundary between a metal and the electrolyte, with a new equilibrium and its own potential difference. Therefore, all potentials are measured against a constant reference point. In order to achieve this, electrochemical experiments involving flowing currents are carried out in a three-electrode-cell consisting of the working electrode (the sample, the material of interest), a counter electrode (usually a foil or wire made of a noble metal (e.g. Au, Pt) that is inert at the desired conditions), and a reference electrode. The reference electrode is a so-called ‘reference electrode of the second kind’. These electrodes consist of a metal in a solution of ions of that metal. The solution also contains a second solid phase of a poorly soluble salt of the same metal, so that the activity of the metal ions $a_{\mathrm{M}^{n+}}$ is determined by the solubility product K_s of the salt. Thus, substituting $a_{\mathrm{M}^{n+}}$ in the Nernst equation

$$E = E_0 + \frac{\mathrm{R} \cdot T}{n \cdot \mathrm{F}} \cdot \ln a_{\mathrm{A}^{n+}} \qquad \text{eq. (3.10)}$$

with

$$K_s^{\mathrm{A}^{n+}\mathrm{B}^{m-}} = \left(a_{\mathrm{A}^{n+}}\right)^n \cdot \left(a_{\mathrm{B}^{m-}}\right)^m \qquad \text{eq. (3.11)}$$

rearranged to

$$a_{\mathrm{A}^{n+}} = \sqrt[n]{\frac{K_s^{\mathrm{A}^{n+}\mathrm{B}^{m-}}}{\left(a_{\mathrm{B}^{m-}}\right)^m}} \qquad \text{eq. (3.12)}$$

yields:

$$E = E_0 + \frac{\mathrm{R} \cdot T}{n \cdot \mathrm{F}} \cdot \ln \sqrt[n]{\frac{K_s^{\mathrm{A}^{n+}\mathrm{B}^{m-}}}{\left(a_{\mathrm{B}^{m-}}\right)^m}} \qquad \text{eq. (3.13)}$$

Since the solubility products of various salts are tabulated and the activity of X^- can be adjusted and kept constant, the potential of the electrode can be determined precisely. The system using hydrogen in equilibrium with water - on a Pt or Au surface - was arbitrarily chosen as the origin for the potential scale (standard hydrogen electrode, SHE). In practice, other electrode systems which are easier to maintain and use (such as Ag|AgCl|3M KCl) are employed [125, p. 86].

Having established the electrochemical potential and measurements, it is useful to point out that the standard potential E_0 (see eq. (3.9)) for a given reaction is the potential at which the reaction is in equilibrium. These values are listed in the electrochemical series (see [125, p. 85]). Polarizing a sample to values below the standard potential causes the reaction to be driven to the reduced species (right in the equilibrium listed below), while polarizing to potentials above the standard potential drives the reaction toward the oxidized species (to the left in the equilibrium listed below):

$$\mathrm{Ag}^+ + \mathrm{e}^- \rightleftharpoons \mathrm{Ag} \qquad E_0 = +0.7996\,\mathrm{V}$$

3.4.2 Passivation of Metals

When anodically oxidizing (dissolving) metals, the concentration of metal ions directly in front of the electrode may grow very high. If the solubility product

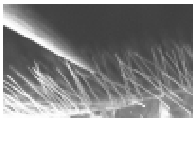

of a metal oxide or metal hydroxide is exceeded, this species may precipitate. Should the precipitate form a dense, uniform layer of sufficient thickness, the anodic current density will drop down to a very small value. The potential at which this occurs is called the Flade potential E_F. The current density i as a funtion of the applied potential E is shown schematically in fig. 3.8. $E_0^{\mathrm{Me|Me}^{n+}}$ marks the standard potential and the onset of corrosion for the reaction:

$$\mathrm{Me} \rightleftharpoons \mathrm{Me}^{n+} + n\,e-$$

The small current flow following the Flade-potential (so-called residual current or passive current i_p) results from ionic conduction in the passive layer. As shown in fig. 3.8, the current density vs. potential plot can be divided into three distinct parts: The first part is the region of active corrosion, beginning with the onset of anodic dissolution at $E_0^{\mathrm{Me|Me}^{n+}}$ and ending when the Flade-potential E_F is reached. At potentials greater than E_F the passive region begins. As the potential increases, the field strength (and therefore the driving force) for charge carriers to pass through the passive layer increases - until, at some point, the driving force is strong enough to allow transpassive current flow. This current usually results from the evolution of oxygen, as in

$$\mathrm{H_2O} \longrightarrow 2\,\mathrm{H^+} + \tfrac{1}{2}\mathrm{O_2}\uparrow + 2\,\mathrm{e^-}$$

at the layer. This is only true if the layer is able to conduct electrons, as is the case for e.g. Fe, Ni, Co, and Zn. When considering valve metals, such as Al, Ti, or Ta, the oxides can grow to very thick layers at ever increasing potentials [125, p. 199]. In this case, voltages of 150 V and more can be applied [126]. The prevailing theory of the mechanism of oxide growth is the ‘high field model’ based on the research of Güntherschulze, Verwey, Mott, and Cabrera [127–131]. More recently, the model was re-evaluated, e.g. by DiQuarto [132] and reviewed in great detail by Lohrengel [133]. Another important factor when dealing with passive layers is the employed electrolyte. For instance, while aluminum will form a passivating barrier layer in neutral solutions, it will vigorously corrode in alkaline solutions since the oxide is soluble at higher pH values. Additions to the electrolyte can also affect the protective layers. The addition of chlorides to a neutral electrolyte will cause the passive layer on aluminum to break down.

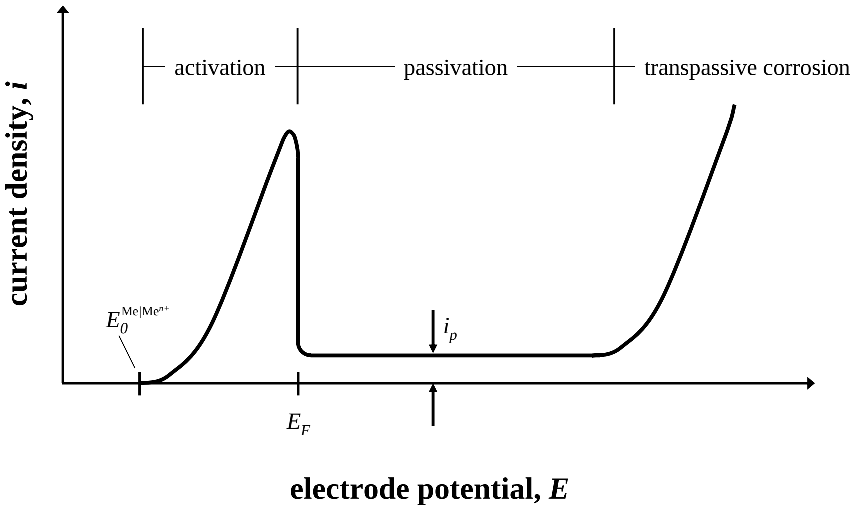

Figure 3.8: Schematic of the current vs. potential behavior during anodic polarization. $E_0^{\mathrm{Me|Me}^{n+}}$ marks the standard potential for the reaction $\mathrm{Me} \rightleftharpoons \mathrm{Me}^{n+} + ne-$ and the onset of corrosion; E_F is the Flade-potential; i_p the residual passive current [125, p. 199].

Passive layers are useful in this work since they are able to protect a metal phase from further corrosion. This will be discussed in the next section in greater detail. In general, the passivation of various metals, including all the metals employed here, has been a topic of great interest in the last 50 or more years, simply because passivity is a very basic form of corrosion protection, yielding longer lifetimes for materials. The reader is referred to the literature for more details on surface oxides and thier properties: DiQuarto, Biaggio, and MacDonald for thier work on tungsten [134–136], Metikos-Hukovic and Babic for molybdenum [137], Giraudea *et al.* for rhenium [138], Ng and Abelev *et al.* for there research on copper [139–142], MacDougal *et al.*, D'alkaine and Santanna, and Cassayre for investigations on the passivity of nickel [143–146], Badawy *et al.*, Tan *et al.*, Akiyama *et al.*, Smith *et al.*, and Hassel *et al.* performed research on the passivity of aluminum [147–152], as well as many other works published in recent years. It should be emphasized that this short list is nowhere near complete or comprehensive, but rather should be seen as a starting point for further reading.

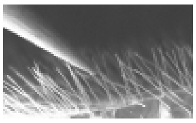

3.4.3 Pourbaix Diagrams

The most basic starting point for the selection of appropriate conditions for selective dissolution of a certain phase is a Pourbaix diagram. These stability diagrams are derived from thermodynamic considerations concerning the equilibria of assumed species of a certain element [153]. A very simple example is aluminum: in this case five equilibria are considered (see table 3.1).

Table 3.1: Equilibria considered for determining the electrochemical stability diagram (Pourbaix diagram), see fig. 3.9.

1. $\mathrm{Al}^{3+} + 3\,\mathrm{e}^- \rightleftharpoons \mathrm{Al}$
2. $\mathrm{Al_2O_3} + 6\,\mathrm{H}^+ \rightleftharpoons 2\,\mathrm{Al}^{3+} + 3\,\mathrm{H_2O}$
3. $\mathrm{Al_2O_3} + 6\,\mathrm{H}^+ + 6\,\mathrm{e}^- \rightleftharpoons 2\,\mathrm{Al} + 3\,\mathrm{H_2O}$

4a. $2\,\mathrm{AlO_2^-} + 2\,\mathrm{H}^+ \rightleftharpoons \mathrm{Al_2O_3} + \mathrm{H_2O}$
4b. $2\,\mathrm{AlO_2^-} + \mathrm{H_2O} \rightleftharpoons \mathrm{Al_2O_3} + 2\,\mathrm{OH}^-$
5a. $\mathrm{AlO_2^-} + 4\,\mathrm{H}^+ + 3\,\mathrm{e}^- \rightleftharpoons \mathrm{Al} + 2\,\mathrm{H_2O}$
5b. $\mathrm{AlO_2^-} + 2\,\mathrm{H_2O} + 3\,\mathrm{e}^- \rightleftharpoons \mathrm{Al} + 4\,\mathrm{OH}^-$

As already introduced in section 3.4.1, the standard potential E_0 for a given reaction is calculated from the Gibbs free energy ΔG_r^0 which is in turn derived from the standard free formation enthalpies $\Delta G_{f,x}^0$ of the involved species (s. eq. (3.7) and eq. (3.8) on page 23). The resulting value for E_0 is inserted into the Nernst equation, eq. (3.9), yielding a value for the potential. In the case of aluminum, only reaction #1 is independent of the pH value, resulting in a horizontal line at a potential between $-1.6\,\mathrm{V}$ and $-1.8\,\mathrm{V}$, depending on the concentration assumed for a_{ox} (in this case, a_{red} is $1\,\mathrm{mol{\cdot}l^{-1}}$ since it is solid Al). Similarily, reactions #2 and #4 are solely dependent on the pH and result in vertical boundaries for the regions of stability of the respective species. Reactions #3 and #5 depend on both the applied potential and the pH so that the regions of stability are bordered by sloped lines.

The pH values are derived from the law of mass action and the fact that the value for the equilibrium constant K can be calculated from the Gibbs free energy as given in equation eq. (3.14) e.g. for reaction #2.

$$K = \exp\left(-\frac{\Delta G_r^0}{R \cdot T}\right) \qquad \text{eq. (3.14)}$$

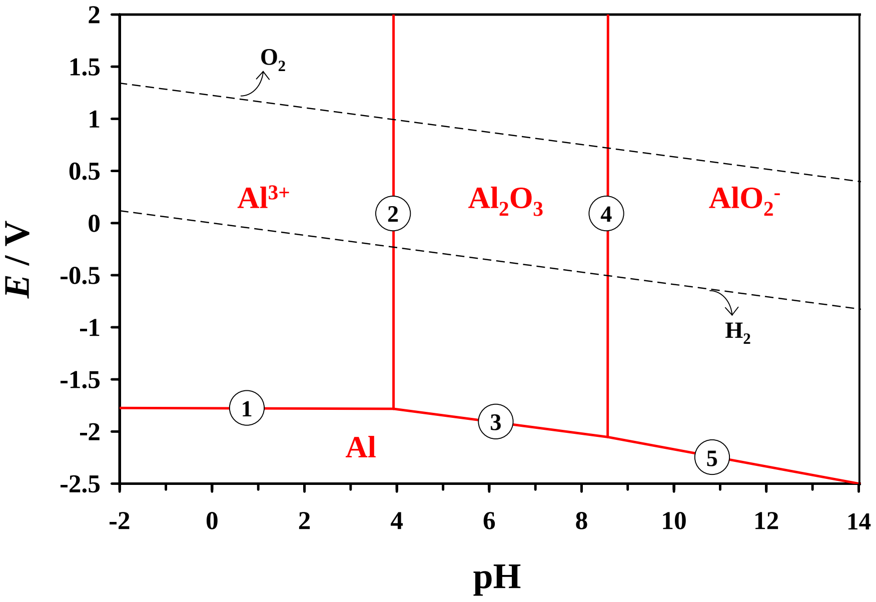

Figure 3.9: Schematic of the electrochemical stability diagram for aluminum; please refer to table 3.1 for the declaration of the equilibria 1 through 5.

Inserting that value into equation eq. (3.15) yields the activity of the H^+ ions (in turn giving the pH) for the transition of alumina to the ionic Al_3^+ species as a function of the concentration of the ionic species.

$$K = \frac{a^2_{Al^{3+}}}{a^6_{H^+}} \Rightarrow a_{H^+} = \sqrt[6]{\frac{a^2_{Al^{3+}}}{K}} \qquad \text{eq. (3.15)}$$

By performing these calculations for all considered equilibria, the regions of thermodynamic stability can be plotted in a potential-pH diagram (fig. 3.9). The regions plotted in fig. 3.9 are calculated for concentrations of 10^{-6} mol·l^{-1}

It is customary to include two more lines on Pourbaix diagrams - the two dashed lines in fig. 3.9. These designate the so-called "electrochemical window" for aqueous solutions. At potentials lying above the upper dashed line, oxygen gas is evolved at the working electrode. Conversely, hydrogen is evolved at potentials lower than the values defined by the lower dashed line. While performing electrochemical measurements is possible outside of the "electrochemical window", a quantitative evaluation of the charge consumed is difficult. This is due to the fact that side reactions (gas evolution) consume charges that cannot be assigned to the reaction of interest.

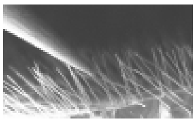

Combined Pourbaix Diagrams

Since the investigated systems consist of two or three materials, it is necessary to consider the Pourbaix diagrams for each material when determining appropriate conditions for selective dissolution of either the matrix or the fibrous phase. This was made easier by superimposing the stability diagrams for the appropriate elements into one diagram, as shown for NiAl-W in fig. 3.10.

Using this diagram, conditions for selectively dissolving either phase were chosen. Similarly, the diagrams for the elements Ni, Al and Re, Ni, Al and Mo as well as Cu and Ag were superimposed (figs. 3.11, 3.12, and 3.13).

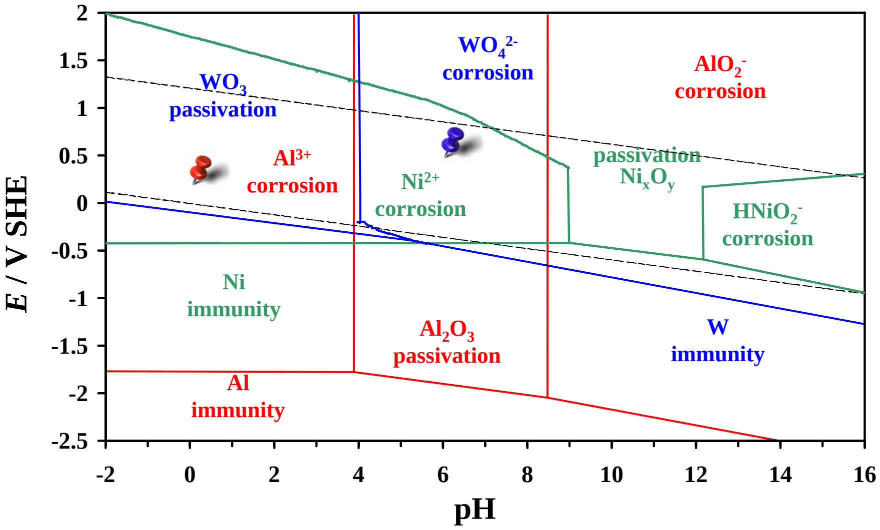

Figure 3.10: Combined Pourbaix-diagram for Ni, Al and W; the red pin designates the chosen conditions for dissolving Ni and Al while passivating W; the blue pin marks the conditions for corroding W and passivating Al.

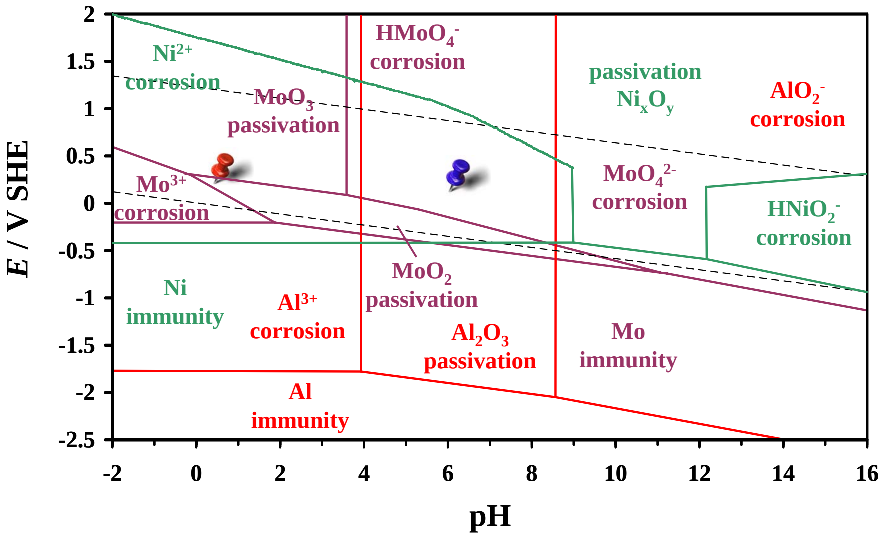

Figure 3.11: Combined Pourbaix-diagram for Ni, Al and Mo; the red pin designates the chosen conditions for dissolving Ni and Al while passivating Mo; the blue pin marks the conditions for corroding Mo and passivating Al.

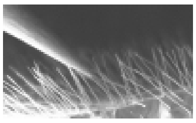

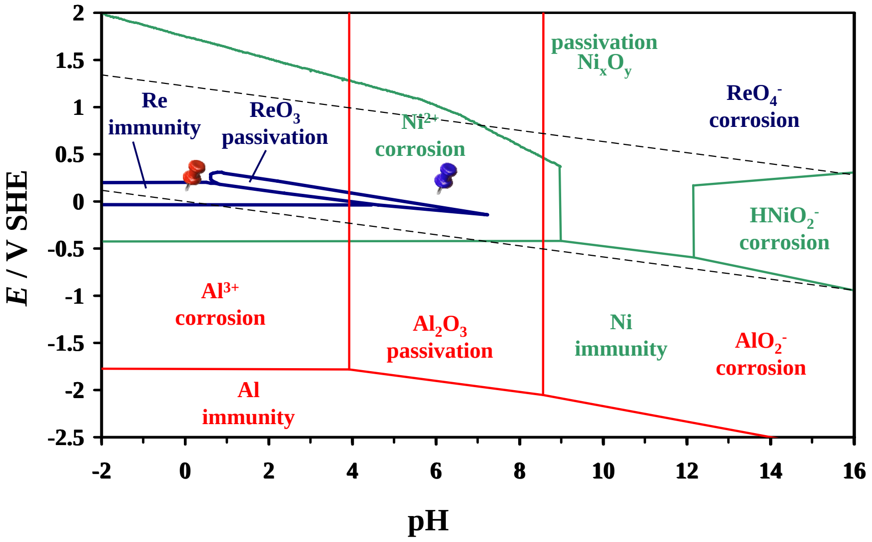

Figure 3.12: Combined Pourbaix-diagram for Ni, Al and Re; the red pin designates the chosen conditions for dissolving Ni and Al while passivating Re; the blue pin marks the conditions for corroding Re and passivating Al.

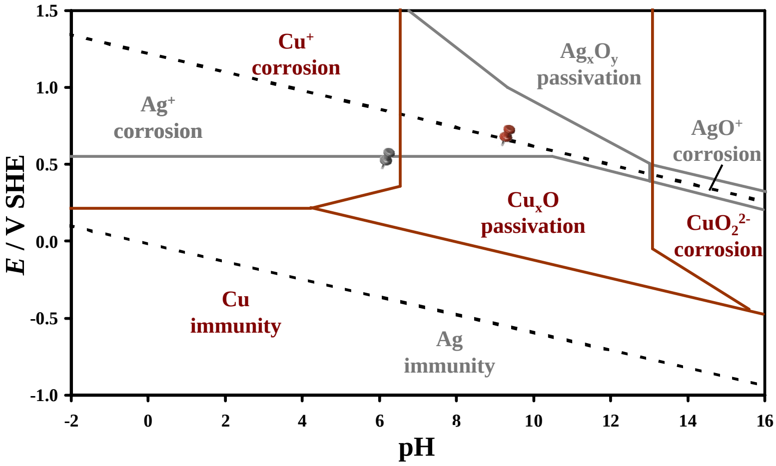

Figure 3.13: Combined Pourbaix-diagram for Ag and Cu; the brown pin designates the chosen conditions for dissolving Ag while passivating Cu; the grey pin marks the conditions for corroding Cu at conditions where Ag is stable.

4 Experimental

Before describing the performed experimental procedures in detail, an overview of the experimental prerequisites will be given in this chapter.

4.1 Equipment

This section lists the equipment employed in the experiments described in the subsequent chapters. The methodology of the experiments is that of standard electrochemistry, necessitating the use of potentiostats, reference electrodes, and counter electrodes as well as other electrical measuring devices. Where successful experiments depended on special, custom-made measuring solutions, the developed set-ups are described in the respective chapters.

4.1.1 Reference Electrodes

Commercial reference electrode Potentials were measured against a commercial reference electrode manufactured by Metrohm. The electrode used was a silver|silver chloride |3 M potassium chloride electrode system with a potential of 207 mV SHE. When using custom-made reference electrodes, these were calibrated using the commercial reference electrode (Deutsche Metrohm GmbH & Co, Filderstadt, Germany).

Mercury|mercurous acetate|sodium acetate electrode system Measurements requiring chloride-free solutions necessitated the use of another reference electrode system. As most of these measurements were performed in acetate buffer solution, a mercury|mercurous acetate electrode system was fabricated. This system was first characterized by Larson and MacDougall in [154] and later optimized by Hassel in [155, p. 19].

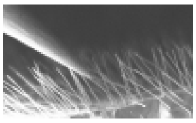

µ-reference electrodes Whenever preparations of very small samples were performed, home-made µ-reference electrode systems (Ag|AgCl and Hg|HgAc) were employed. These were manufactured according to the methods communicated by Hassel *et al.* and Lill *et al.* in [156, 157]. A short description of the procedure is given below (see section 4.3).

4.1.2 Electrical Equipment

Potentiostats

Electrochemical experiments were performed with potentiostats manufactured by Princeton Applied Research, Ivium Technologies, and Radiometer Analytical. In the following section a short description of the different devices used is given:

EG&G Pstat / Gstat 283 This potentiostat utilizes the IEEE 488 bus standard (GPIB). In combination with Scribner Associates International's software *CorrWare* and *CorrView*, a wide range of electrochemical techniques is possible.

- current range: 1 nA to 120 mA
- scan rates: $1\,\mu V{\cdot}s^{-1}$ to $1\,V{\cdot}s^{-1}$
- scan range: $-10\,V$ to $+10\,V$

(AMETEK Princeton Applied Research, Oak Ridge, TN, USA and Scribner Associates, Southern Pines, NC, USA).

IviumStat The IviumStat potentiostat utilizes the much more widespread USB port making it much more flexible to use. Also, the IviumStat has a built in frequency response analyzer (FRA) for performing impedance measurements. The IviumSoft control software offers all the required electrochemical methods.

- current range: 1 pA to 10 A
- scan rates: $1\,\mu V{\cdot}s^{-1}$ to $10\,V{\cdot}s^{-1}$
- scan range: $-10\,V$ to $+10\,V$

(Ivium Technologies, Eindhoven, The Netherlands)

CompactStat This potentiostat is almost identical to the IviumStat with slightly reduced current and potential ranges. The device is very small and can be powered by the USB port, making it extremely versatile for applications requiring only low currents.

- current range: 1 pA to 10 A
- scan rates: $1\,\mu\mathrm{V{\cdot}s^{-1}}$ to $10\,\mathrm{V{\cdot}s^{-1}}$
- scan range: -4 V to $+4$ V

(Ivium Technologies, Eindhoven, The Netherlands)

VoltaLab PST050 The VoltaLab PST050 utilizes the high-speed write-through RS-232 interface. It is controlled by VoltaMaster software, offering a wide range of electrochemical methods.

- current range: 1 pA to 1 A
- scan rates: $1\,\mu\mathrm{V{\cdot}s^{-1}}$ to $20\,\mathrm{V{\cdot}s^{-1}}$
- scan range: -15 V to $+15$ V

(Radiometer Analytical SAS, Villeurbanne Cedex, France)

Other Electrical Devices

Solartron / Schlumberger DMM 7150plus Digital multimeters were used for logging current and voltage data during electropolishing.

- maximum sensitivity: 100 nV
- input resistance: $> 10\,\mathrm{G\Omega}$
- ranges: 0.2 V to 1000 V

(Solartron Analytical, Farnborough, Hampshire, England)

Power supply E0300-0.1 Power supply manufactured by Delta Elektronika, analog controls was used for electropolishing.

- maximum current output: 100 mA
- maximum voltage output: 300 V

(Delta Elektronika BV, Zierikzee, The Netherlands)

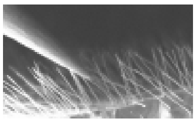

Voltcraft DPS-8003PFC Power supply manufactured by Conrad Elektronik, digital controls, was used during electropolishing.

- maximum current output: 2.5 A, step size 10 mA
- maximum voltage output: 80 V, step size 10 mV

(Conrad Elektronik SE, Hirschau, Germany)

4.1.3 Electron Microscopy

Zeiss / LEO 1550 VP Scanning electron microscopy was performed using both "InLens" and "MPSE" (Multi Pressure Secondary Electron) detectors (Zeiss, Oberkochen, Germany).

Zeiss / LEO 1540 XB with FIB Preparations requiring ultra-flat surfaces or local metal deposition were performed using a Focused Ion Beam (FIB) in a crossbeam configuration. Deposition was achieved by utilizing a Gas Inlet System (GIS). Electron Backscatter Diffraction (EBSD) measurements were also performed in this microscope (Zeiss, Oberkochen, Germany).

FEI CM20 S/TEM Investigations of material properties were also performed using a transmission electron microscope model CM20 S/TEM manufactured by FEI. The microscope is equipped with an energy dispersive x-ray (EDX) system, model DX4 manufactured by EDAX (FEI Deutschland GmbH, Kassel, Germany and EDAX, Mahwah, NJ, USA).

4.1.4 Micro and Nanomanipulation

Süss MircoTec PM5 and Mitutoyo LD microscope The combination of the micro prober (SÜSS MicroTec) with micromanipulators and a high performance long distance (LD) light microscope (Mitutoyo) allowed preparation and manipulation (see Kleindiek-equipment below) of samples down to the sub-micron range (SUSS MicroTec Test Systems GmbH, Sacka, Germany and Mitutoyo, Tokyo, Japan).

Kleindiek Manipulation System Both Zeiss microscopes have capabilities for employing piezo-driven manipulators (MM3A-EM) and a piezo-driven gripper (MGS2-EM) - each with sub-nanometer precision - manufactured by Kleindiek Nanotechnik GmbH. The Kleindiek equipment was also used in combination with the long distance light microscope (Kleindiek Nanotechnik GmbH, Reutlingen, Germany).

Picoprobes The standard tool tips for the MM3A-EM manipulators were so-called picoprobes. These probes consist of a tinned copper shaft (0.51 mm) to which a 10 μm tungsten wire is attached. The tungsten wire has a pointed tip with a nominal diameter less than 0.1 μm (GGB Industries, Inc., Naples, FL, USA).

4.1.5 Miscellaneous

Digital SLR Images from the Mitutoyo LD microsope were taken using a Pentax ist Ds digital single lens reflex (SLR) camera (PENTAX Europe GmbH, Hamburg, Germany).

CCD camera Capturing movies while manipulating nanowires was achieved using a CCD camera manufactured by Mintron (Mintron, Taipei, Taiwan).

HDD recorder In order to record videos from the Mitutoyo LD microscope, a CCD camera was used (as a substitute for the digital SLR) in combination with a HDD/DVD recorder RH199 manufactured by LG Electronics (LG Electronics Deutschland GmbH, Willich, Germany).

Capillary puller A Narishige PC-10 capillary puller was used to locally melt glass capillaries and pull them into very thin shapes (Narishige, Tokyo, Japan).

Microgrinder A Narishige EG-400 microgrinder was used to shape the glass capillaries after pulling (Narishige, Tokyo, Japan).

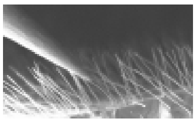

Ultrafiltration system The filtration unit was used in combination with a standard water jet pump and cellulose acetate filters with a pore size of 0.2 µm (Sartorius AG, Göttingen, Germany).

Dual jet electropolishing set-up A Tenupol-2 manufactured by Struers was used for thinning metal samples (Struers GmbH, Willich, Germany).

ICP-OES Trace analysis was performed using Inductively Coupled Plasma Optical Emission Spectroscopy in a Thermo Iris Intrepid Duo HR (Thermo Fisher Scientific, Inc., Waltham, MA, USA).

4.2 Materials

Chemicals, materials, and the compositions of the employed solutions and electrolytes are listed in this section.

4.2.1 Chemicals

All chemicals were obtained from VWR International GmbH, Darmstadt, Germany:

- acetic acid (glacial, 100%, anhydrous)
- agar
- hydrochloric acid (32%)
- hydrogen peroxide (30%)
- mercury
- mercury nitrate
- perchloric acid (60%)
- potassium chloride
- sodium acetate trihydrate
- sodium borate

Purified water was produced using a “Purelab plus” manufactured by USF, Ransbach-Baumbach, Germany.

Electrolytes

1 M **hydrochloric acid** Hydrochloric acid (32%) was diluted 1:10 yielding a 1 M HCl solution. This electrolyte was used for digesting the NiAl matrix under potentiostatic control.

Acetate buffer 1 M acetate buffer with a pH value of 6.0 was prepared by mixing 122.4 g of sodium acetate trihydrate with 2.9 g glacial acetic acid in 1 l of deionized water. This mixture was used for passivating the matrix of all samples [155, p. 24].

Borate buffer Selective dissolution of the Cu wires in the Ag-Cu samples was performed in a borate buffer. It consisted of a 0.1 M $Na_2B_4O_7 \cdot 10\,H_2O$ solution with a pH of 9.2.

Other Solutions

Solution for digesting NiAl A chemical approach for selectively dissolving the NiAl matrix was realized by using a mixture of H_2O:HCl:H_2O_2 with a ratio of 80:10:10. Chloride ions from the hydrochloric acid attack the passive oxide layer on NiAl, while the chemical potential of the solution is slightly increased due to the addition of hydrogen peroxide, thus increasing the oxidizing power of the solution and facilitating the digestion of the matrix.

Electropolishing solution A mixture of glacial acetic acid with 6% perchloric acid was used for electropolishing NiAl-X samples.

Electropolishing solution (dual jet set-up) Electropolishing ultrathin samples in the dual jet set-up was performed using a mixture of methanol and nitric acid (70:30).

4.2.2 Samples

All pre-alloys were prepared by induction melting and casting of metal powders in a water-cooled copper mold. They were subsequently processed in a Bridgman-type crystal growth oven. After directional solidification, the samples were cut in the desired manner (see section 4.4).

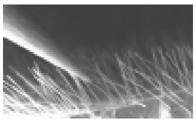

NiAl-*X* Ni and Al were always used in equiatomic amounts. The percentage of refractory metal (X) added to the alloys and the final compositions were:

X	at%	composition
W	1.5	49.25 Ni 49.25 Al 1.5 W
Re	1.5	49.25 Ni 49.25 Al 1.5 Re
Mo	9.0	45.50 Ni 45.50 Al 9.0 Mo

Nickel was obtained from GfE Gesellschaft für Elektrometallurgie mbH, Nürnberg, Germany. Aluminium was obtained from VAW Aluminium AG, Bonn, Germany. Tungsten was obtained from Goodfellow GmbH, Friedberg, Germany. Rhenium and molybdenum were obtained from H. C. Starck GmbH, Goslar, Germany.

Ag-Cu The Ag-Cu system has its eutectic at a composition of 60.1 at.% Ag and 39.9 at.% Cu. This composition is very close to the theoretical boundary between lamellar and fibrous growth (see p. 16). Therefore, these samples yielded domains with self-ordered wires next to areas with stacked lamella. Ag was obtained from Goodfellow GmbH, Friedberg, Germany. Cu was obtained from Haines & Maassen Metallhandelsgesellschaft mbH, Bonn, Germany.

4.2.3 Other Materials

Silicon wafers Silicon wafers were supplied by CrysTec. The wafers were used as substrates and holders for various preparations (CrysTec GmbH Kristalltechnologie, Berlin, Germany).

Silicone rubber Masking samples and fabricating gaskets on capillary tips was achived using SCRINTEC® 901 RTV-1 Silicone Rubber, supplied by RALICKS Industrie- und Umwelttechnik (Rees-Haldern, Germany).

Glass capillaries Sodium carbonate glass capillaries with a diameter of 1 mm were used for preparing µ-reference electrodes (Hilgenberg, Malsfeld, Germany).

Metal wires High purity gold (99.999%) and silver (99.999%) wires for the fabrication of µ-reference electrodes were obtained from Wieland Dentaltechnik and Goodfellow, respectively (Wieland Dental & Technik GmbH & Co. KG, Pforzheim, Germany and Goodfellow GmbH, Friedberg, Germany).

4.3 Manufacturing µ-reference Electrodes

Preparing a reference electrode requires placing a metal in equilibrium with ions of the same metal and controlling the concentration of those ions (s. section 3.4.1). In order to measure potentials in small liquid droplets or in very small electrochemical cells, it is necessary to have small reference electrodes. These µ-reference electrodes were manufactured by using glass capillaries that were drawn out to pointed tips using a capillary puller (Narishige PC-10), subsequently ground to the right shape using a microgrinder (Narishige EG-400), and finally filled with reference electrode materials. Two types of µ-reference electrodes were manufactured: a miniature silver|silver-chloride system and a mercury|mercurous acetate version.

µ-Ag|AgCl reference electrode For these reference electrodes, silver wires with a diameter of 125 µm were placed in an electrochemical cell with a commercial Ag|AgCl|3 M KCl reference electrode, a platinum foil counter electrode and 1 M HCl as the electrolyte. First, the wires were roughened by cycling them between −0.1 V SHE and 0.5 V SHE at a scan rate of $10\,\mathrm{mV{\cdot}s^{-1}}$. Subsequently, they were coated with a layer of AgCl by polarizing to a potential of 0.1 V SHE for 120 s and to 0.3 V SHE for 600 s. The wires were rinsed thoroughly with water and stored in a saturated KCl solution. As described above, the capillaries were drawn and ground to yield the desired tip shape and diameter (200 µm). These capillaries were then filled with saturated KCl which was solidified by boiling it with 4 wt·% agar. Finally, the wires were inserted into the solidified electrolyte and fixed in place with glue. The µ-reference electrodes were stored in a saturated KCl solution [156].

µ-AuHg|$\mathbf{Hg_2(CH_3COO)_2}$ reference electrode In order to obtain chloride-free µ-reference electrodes, the mercury | mercurous acetate system was chosen. The preperation of these electrodes is almost identical to that of the Ag|AgCl

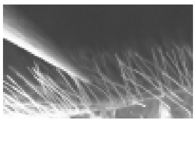

µ-reference electrodes described above. In this case, Au-wires (diameter 200 µm) were used. First, these wires were amalgamated by polarizing them to 0.2 V SHE for 180 s in 0.1 M $Hg_2(NO_3)_2$. Next, the wires were rinsed with water and coated with $Hg_2(CH_3COO)_2$ by immersing them into 1 M $NaCH_3COO$ at 0.58 V SHE for 600 s. The prepared wires were inserted into glass capillaries filled with electrolyte. The electrolyte consisted of saturated $NaCH_3COO$ which was solidified with agar. The µ-reference electrodes were stored in a 1 M $NaCH_3COO$ solution [157].

4.4 Sample Preparation - Basic Orientation of µ-structure

As described in sections 3.2 and 3.3, the samples obtained after directional solidification consist of cells with diameters in the order of 300 µm, depending on the fabrication conditions. Each cell consists of an ordered array of nanowires. By cutting a sample in a direction perpendicular to the growth direction, cross-sections of the wires are obtained. When viewed with a microscope these wires appear as discs embedded in a matrix (see fig. 4.1). If the sample is cut in a direction parallel to the growth direction, the exposed surface will show flat sections of nanowires (see fig. 4.2). This is due to the fact that it is very difficult to cut the sample in precisely the same plane as that of the wire growth.

In most cases described in this work, the samples were cut perpendicular to the growth direction, initially yielding nanodisc arrays. The further processing of these samples will be discussed in the following chapters.

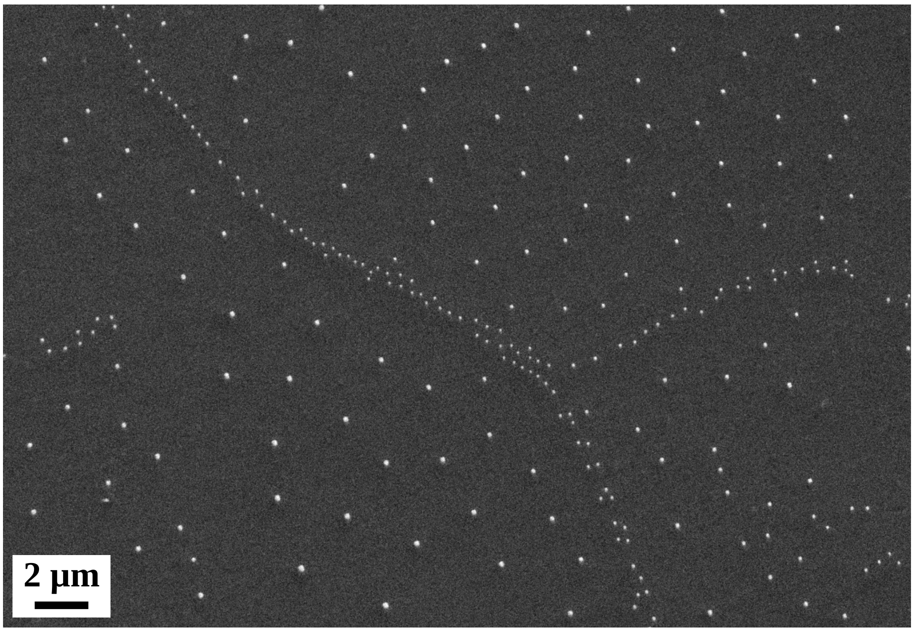

Figure 4.1: SEM image of a cross-sectionally cut *ds*-NiAl-W sample.

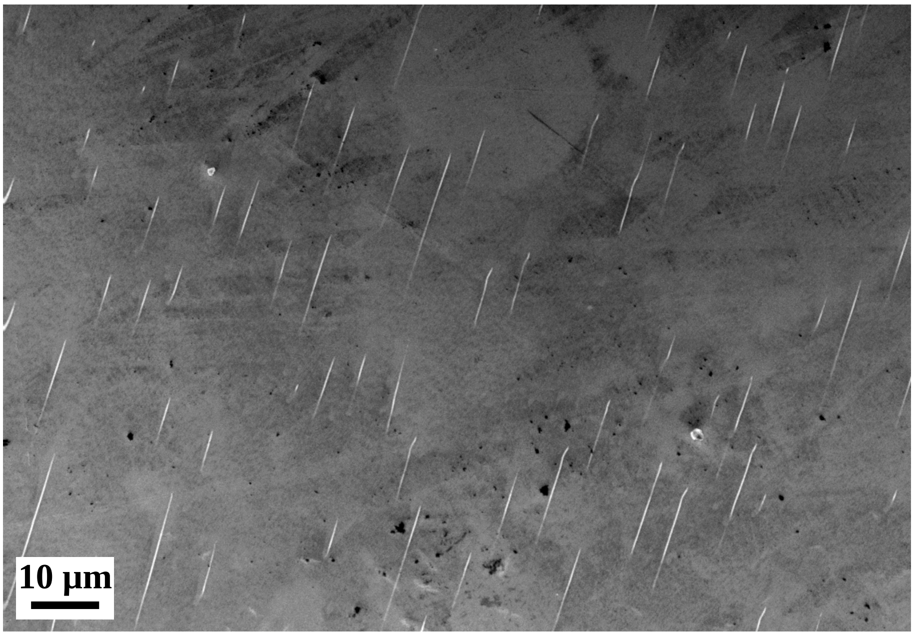

Figure 4.2: SEM image of a *ds*-NiAl-W sample cut in the longitudinal direction.

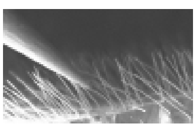

5 Selective Matrix Dissolution

Selectively dissolving the matrix phase is achieved by applying conditions which are corrosive for the matrix elements and simultaneously have a passivating effect on the fibrous phase, or none at all if the elements of the minor phase are immune to the chosen (electro-)chemical conditions. The appropriate conditions were determined by studying the Pourbaix diagrams as discussed in section 3.4.3. For the NiAl-X systems, dissolving the matrix was always performed in hydrochloric acid solution while applying mildly anodic potentials. This could be achieved by submersing samples in a solution of hydrogen peroxide and hydrochloric acid or by using an electrochemical set-up. The latter method allows better control of the dissolution process. In either set-up, both Ni and Al corroded while the refractory elements Mo, Re, and W were oxidized slightly or not influenced at all.

Similarly, for the Ag-Cu system, conditions were chosen where the silver and silver oxides were soluble while copper was passivated. Mildly anodic potentials were again applied using an electrochemical cell but in this case, a borate buffer with a pH of 9.2 was used. The results of treating the materials in the manner described here, as well as the different structures obtained, are discussed in the following sections.

5.1 Partial Matrix Dissolution

After directional solidification, the alloys were cut as described in section 4.4 and mechanically ground prior to performing the selective etching procedures described above. The various morphologies obtained depending on the experimental set-up are shown in the following sections.

The research on these nanostructured materials yielded a multitude of fascinating images - mostly obtained using scanning electron microscopy. Only a small selection of these images can be shown here.

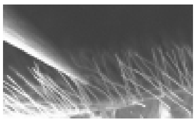

5.1.1 "Forests"

The most basic procedure following directional solidification and investigating the samples' ground cross-sections (see fig. 4.1, on page 43) is partially releasing the nanowires from the matrix in order obtain information about the wire morphology. As indicated in section 3.3, the wire's morphology is dependent on the crystallographic orientation relationship between the matrix phase and the wire phase. Various morphologies were found in the course of the performed investigations; these will be shown on the next few pages.

***ds*-NiAl-Re** The first system to be characterized was *ds*-NiAl-Re. This alloy has been extensively studied in the last 15 years due to its excellent high temperature stability while maintaining favorable mechanical properties. Directional solidification yielded self-ordered arrays of nanowires with diameters of approx. 400 nm. As discussed in detail in section 3.2, the size and spacing of the nanowires can be adjusted within certain experimental boundaries.

Figure 5.1 **A** shows the ground surface of a *ds*-NiAl-Re cross-section. The white dots are the front surfaces of the Re wires; the dark area is the NiAl matrix. A closer look reveals that the Re "discs" protrude slightly - this is due to the fact that Re is much harder than NiAl and therefore less Re is worn away during grinding. The lower image (fig. 5.1 **B**) shows exposed Re wires after 15 minutes of digestion in the H_2O / HCl / H_2O_2 solution (80:10:10). The regularly spaced wires have a length of approx. 5 µm. The images in fig. 5.2 depict Re wires of different lengths after different periods of digestion in the solution mentioned above. Figure 5.2 **A** shows wires with a length of approx. 20 µm obtained after digestion for 30 min; fig. 5.2 **B** shows wires with a length of approx. 50 µm which were observed after 2 hours of digestion. At these lengths, the wires fall over due to their own weight.

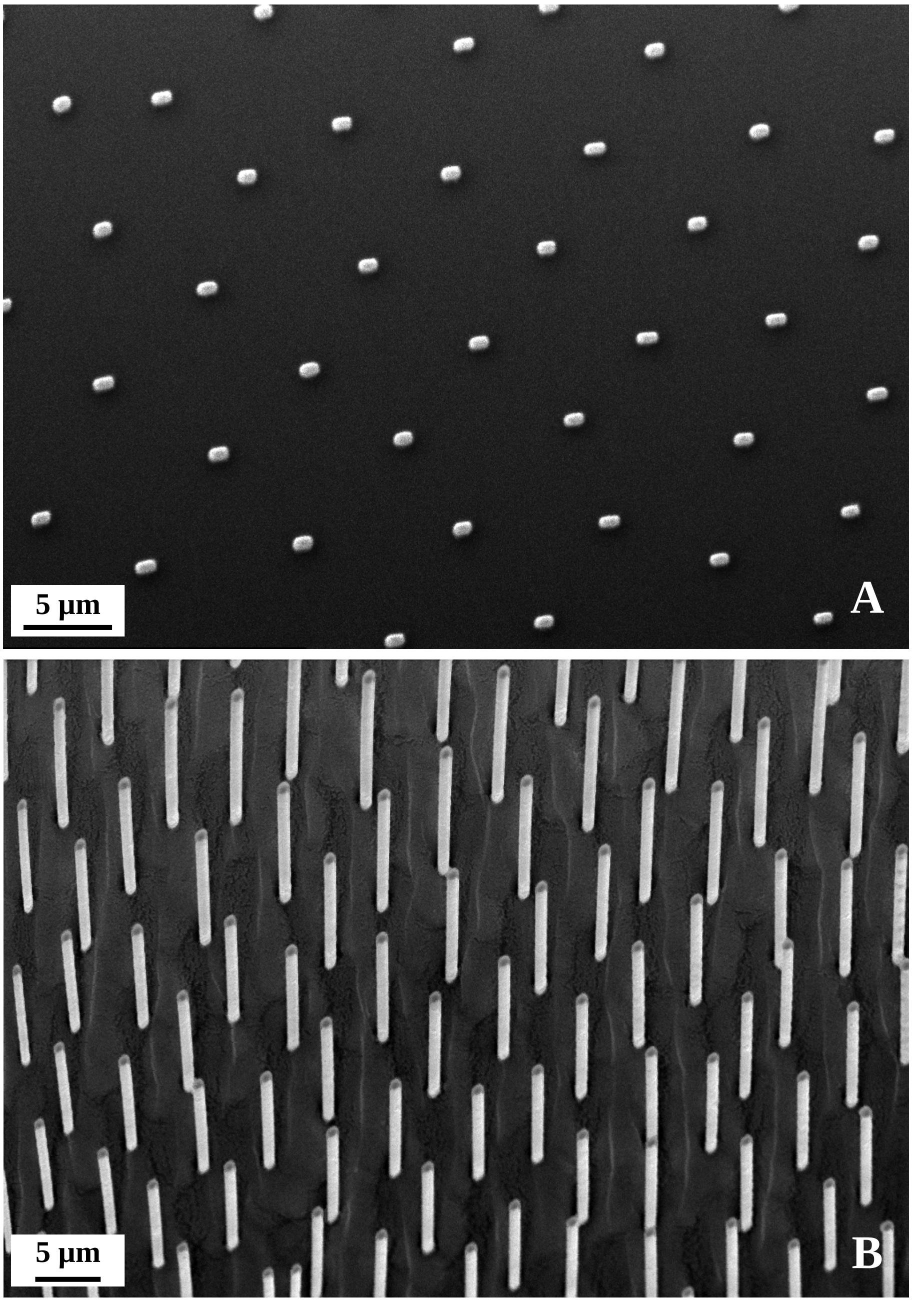

Figure 5.1: SEM images of a *ds*-NiAl-Re sample. **A**: Polished sample; the cross-sections of the Re wires protrude slightly due to their greater hardness compared to NiAl. **B**: Sample after selective matrix digestion in HCl / H_2O_2 for 15 min· [103].

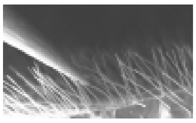

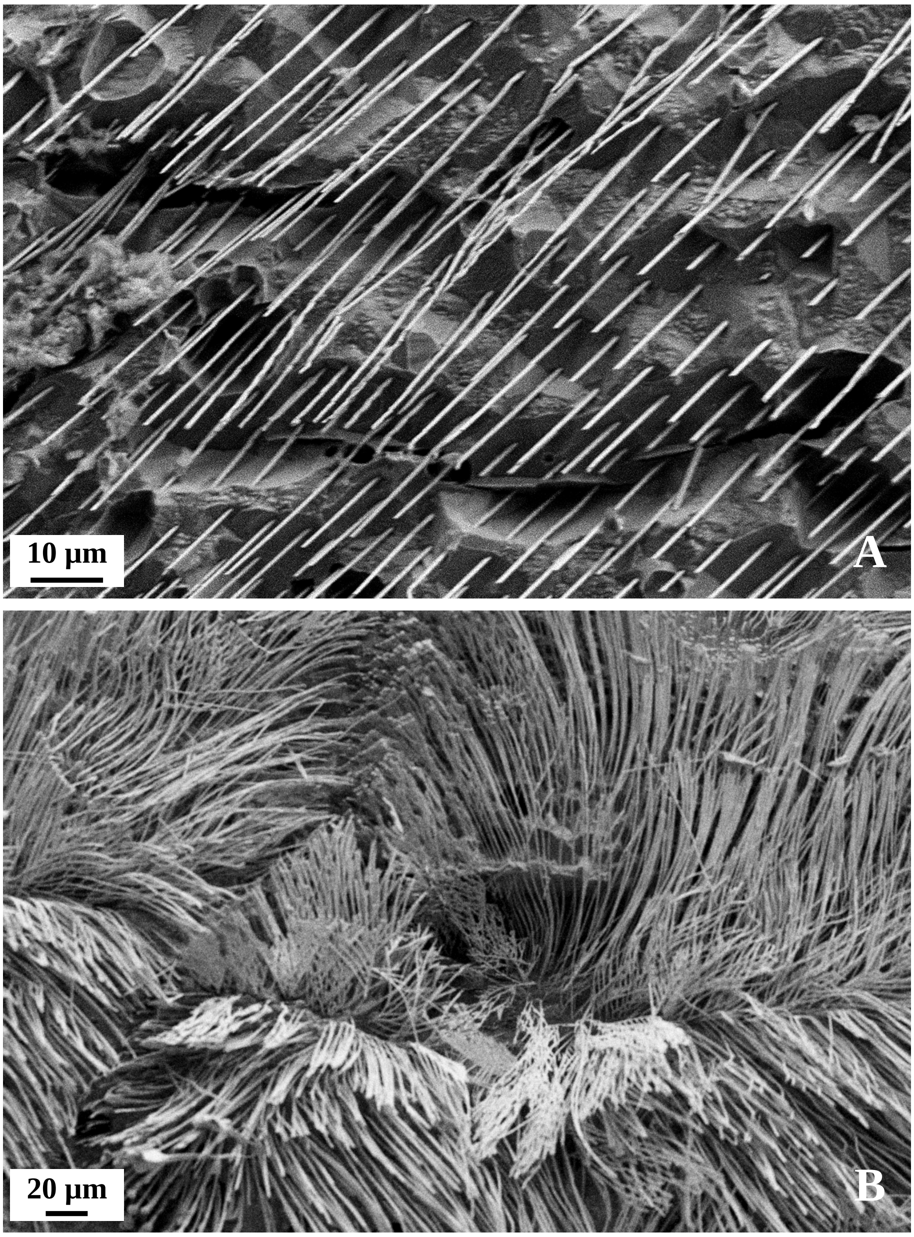

Figure 5.2: SEM images of a *ds*-NiAl-Re sample **A**: Sample after selective matrix digestion in HCl / H_2O_2 for 30 min. **B**: Sample after selective matrix digestion in HCl / H_2O_2 for 2 hours.

***ds*-NiAl-Mo** Another system investigated in this work was *ds*-NiAl-Mo. This system yields slightly larger wires with a very high degree of regularity in spacing.

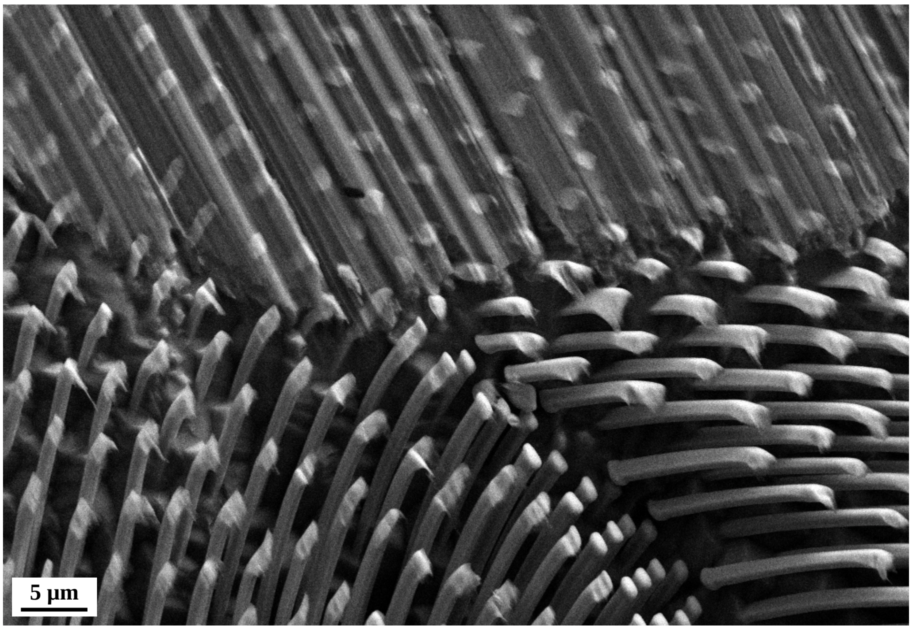

Figure 5.3: SEM image of a *ds*-NiAl-Mo sample after selective matrix digestion in 1 M HCl for 5 min at a potential of 250 mV SHE. The upper part of the image shows the ground, non-etched sample surface. The lower part shows a cell boundary with wires of different orientations.

The image in fig. 5.3 is very interesting since it shows a close-up view of a eutectic cell boundary, as well as a non-etched portion of the sample. The sample was submitted to selective matrix dissolution in 1 M HCl for 5 min at a potential of 250 mV SHE. It can be seen nicely that the grooves on the sample surface, which result from mechanical grinding of the samples, are also present in the face surfaces of the wires themselves. This proves the very selective nature of the chosen etching conditions.

A closer look at the high resolution image in fig. 5.4 shows the very distinct rectangular shape of the exposed Mo wires. Once again, the tips of the wires show morphologies resulting from surface treatments prior to selective etching. The selective etching procedure yielded regular wire arrays. The wires have a diameter of approx. 500 nm and a length of approx. 5 µm.

***ds*-NiAl-W** The main alloy of interest in this work was *ds*-NiAl-W. Another special feature of the nanowires investigated in this project is that they are

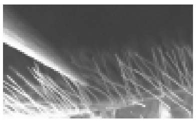

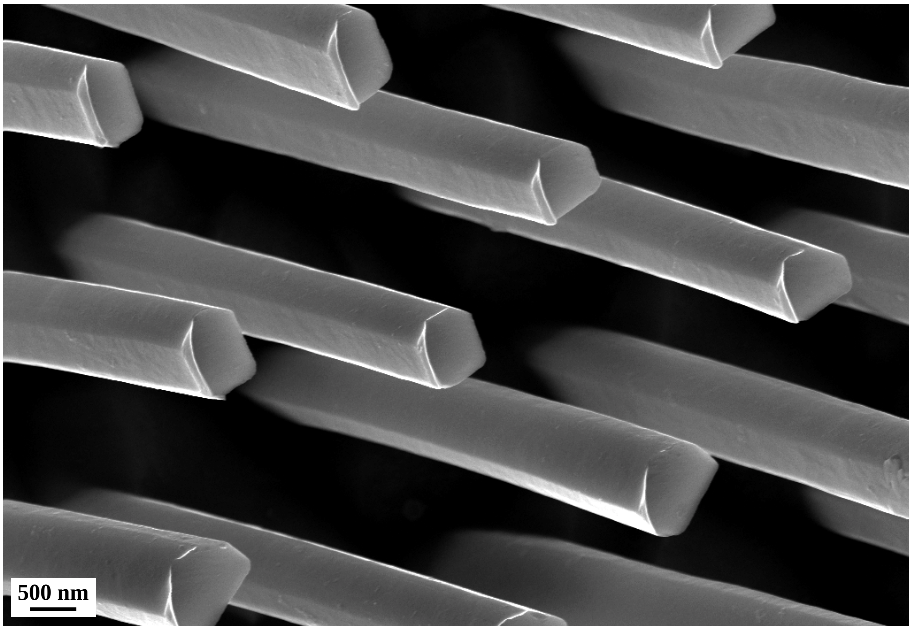

Figure 5.4: SEM image of a *ds*-NiAl-Mo sample after selective matrix digestion in 1 M HCl for 5 min at a potential of 500 mV SHE. The exposed wires have a diameter of approx. 500 nm and a length of approx. 5 µm.

visible under a light microscope, even though their diameters are significantly smaller than the wavelengths of visible light (fig. 5.5). The reason they are visible despite their small dimensions is that the shiny metallic surface scatters the light making the wires visible [158]. The result is that the wires appear larger than they actually are. This feature allowed the use of the SÜSS microprober (see section 4.1.4) for performing many *in situ* experiments and for quickly observing initial results and intermediate steps during various preparations.

The images in figures 5.6, 5.7, and 5.8 show a sample of *ds*-NiAl-W after electrochemical etching for 30 min. Figure 5.6 shows a side view of the sample. Figure 5.7 **A** is an overview of the sample showing the eutectic cells. This image, as well as fig. 5.7 **B**, shows the tendency of the wires to be well aligned in the center of the cells, but to bend toward the cell boundary in the outer regions of each cell [159].

The images in fig. 5.8 are close-up views of the wires. The exposed wire length is approx. $10 - 12$ µm. Figure 5.8 **B** shows a high resolution image of a wire section. The periodic difference in shading is a result of fluctuations in thickness. These fluctuations are caused by undercooling effects. Two concurrent types of undercooling control the solidification process: crystallographic undercooling and concentration undercooling [80]. Due to a mismatch between the crystal structures of the fibrous phase and the matrix, crystallographic undercooling becomes more dominant, shifting the mechanism toward concentration undercooling [103]. These concurring effects lead to the observed fluctuations in thickness.

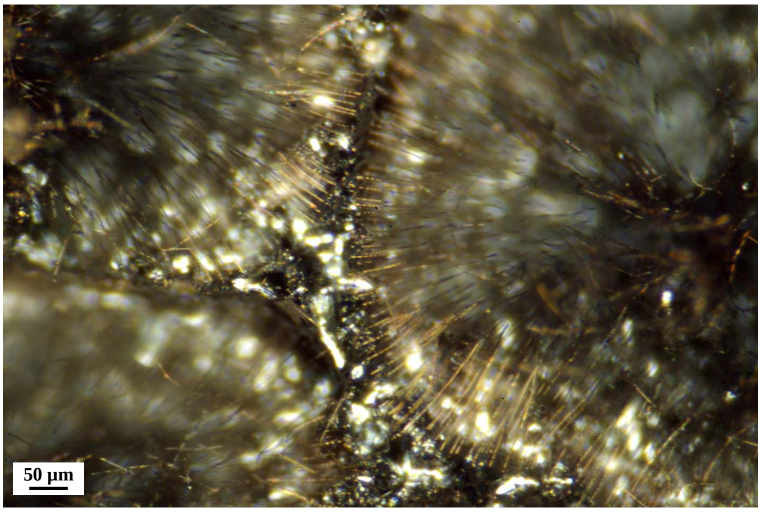

Figure 5.5: Light microscope image of *ds*-NiAl-W after 30 min of selective dissolution. The microscope's limited depth of field is the cause for the poor focus of this image.

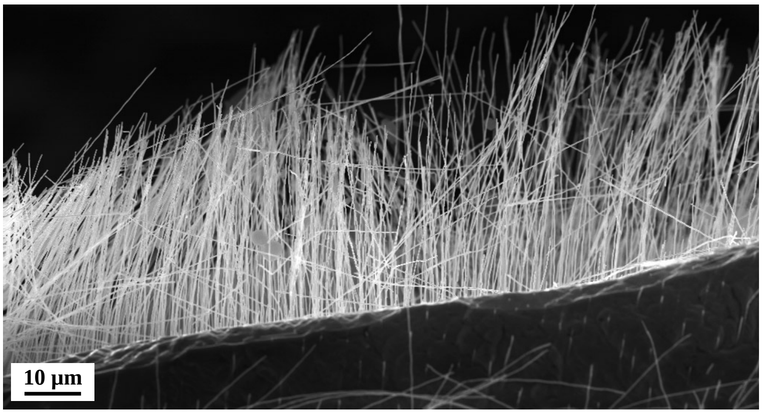

Figure 5.6: Side view of *ds*-NiAl-W sample after 30 min of selective dissolution.

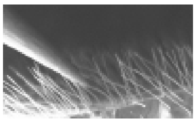

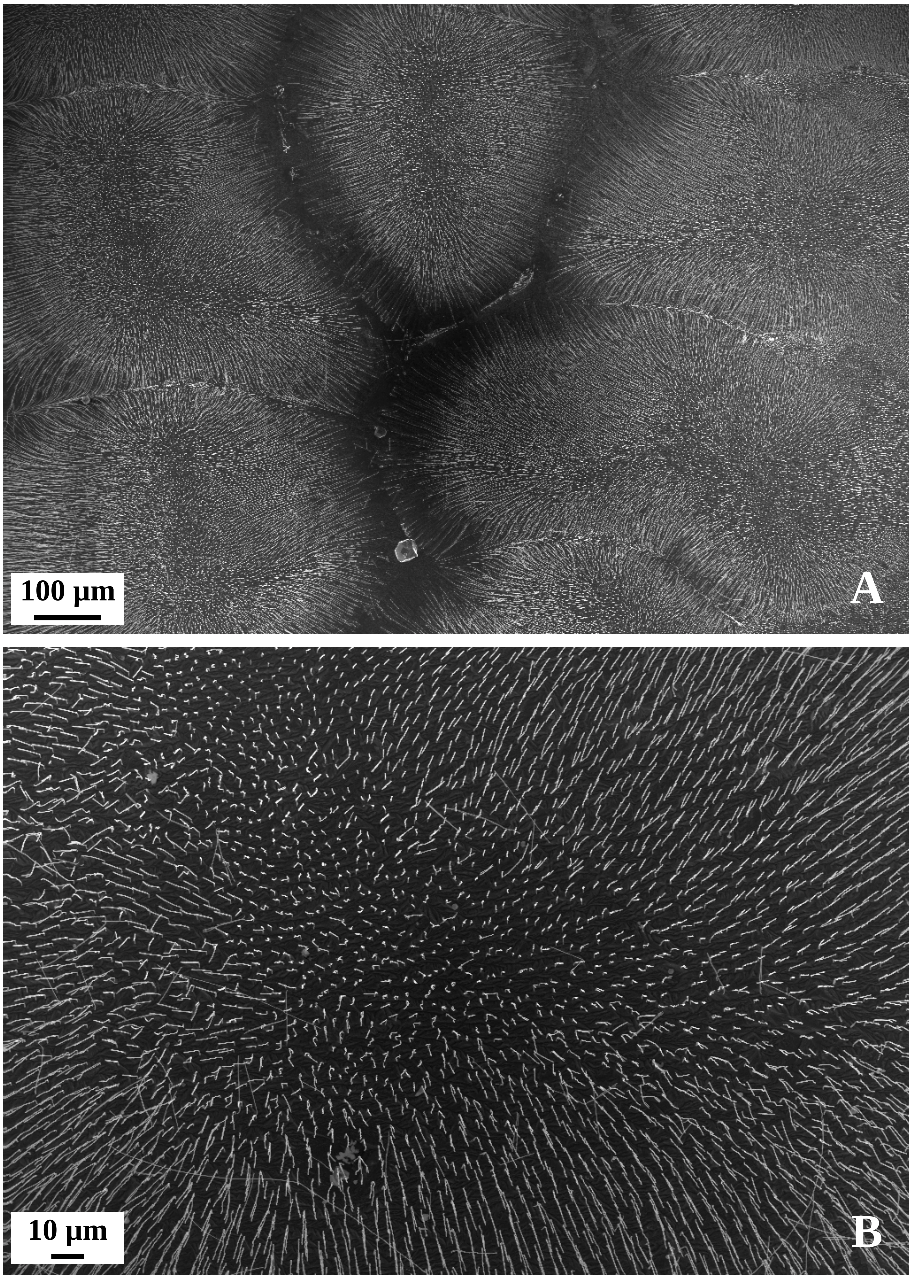

Figure 5.7: SEM images of a *ds*-NiAl-W sample after 30 min of selective dissolution. **A**: Overview of multiple eutectic cells. **B**: Close-up view of a single eutectic cell.

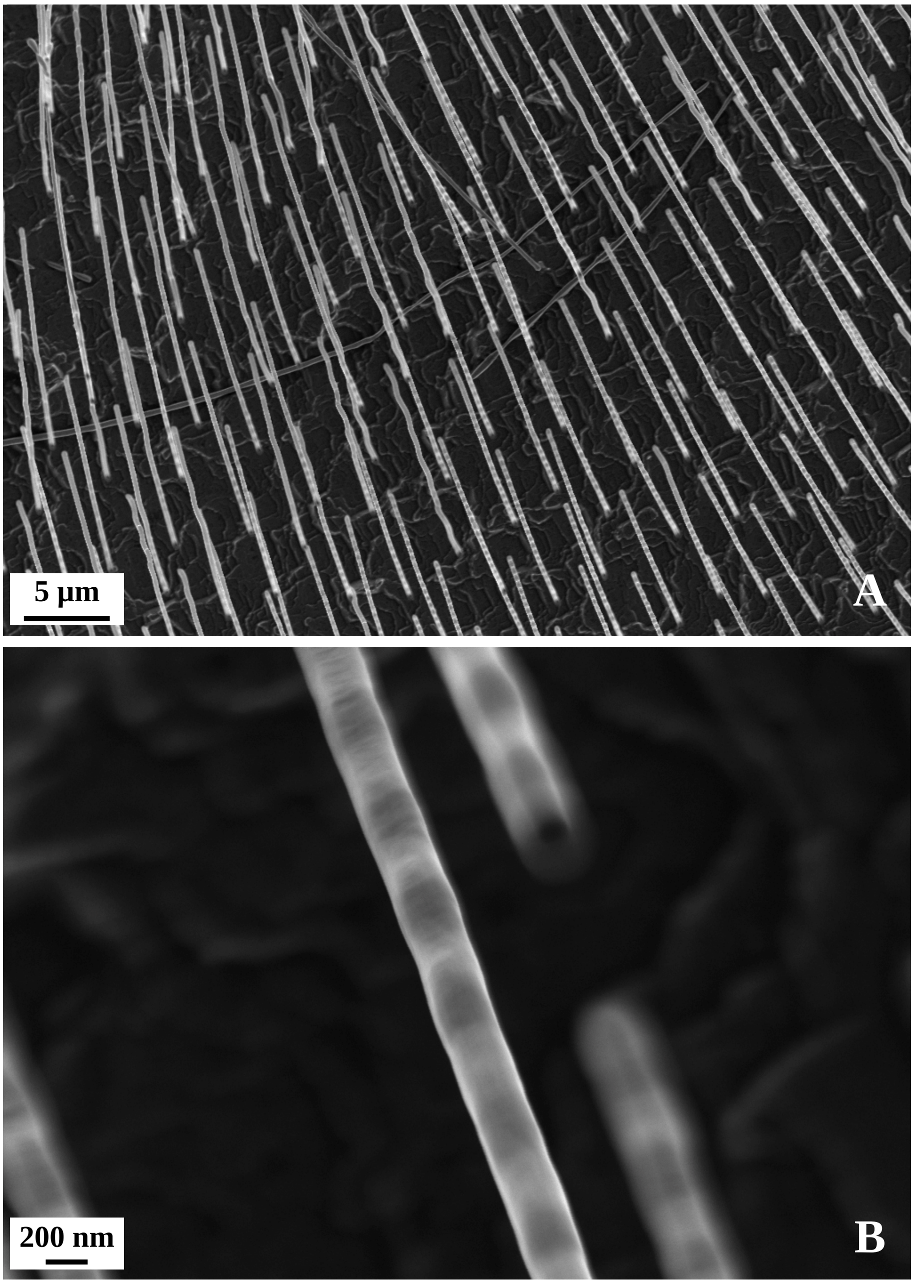

Figure 5.8: SEM images of a *ds*-NiAl-W sample after 30 min of selective dissolution. **A**: Close-up view of W nanowires protruding from the matrix surface. The exposed wires' length is approx. $10 - 12\,\mu\text{m}$. **B**: High resolution image of a single nanowire. The wires' diameter can be determined from this image to be 200 nm.

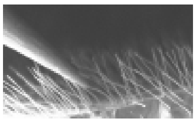

***ds*-Ag-Cu** Another investigated alloy was the the silver-copper system. As mentioned in section 3.2, this system is special due to the fact that its eutectic composition is very close to the theoretical boundary between fibrous and lamellar systems. As a consequence, the structures obtained from the directional solidification process are partly fibrous and partly lamellar. This can be seen nicely in fig. 5.9 where the left side of the image shows lamellar structures while the right side shows Cu nanowires with a diameter of approx. 300 nm. Preparing these exposed structures was performed by submersing the samples into borate buffer (pH 9.2) and polarizing to 700 mV SHE. This system is discussed in more detail in [99].

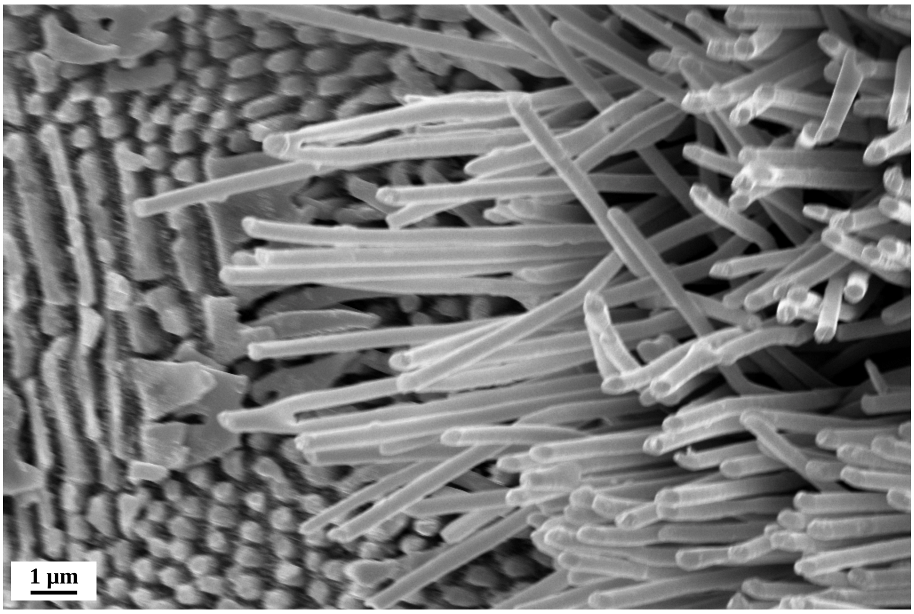

Figure 5.9: Exposed copper wires after dissolution of the silver matrix for time segments totaling nearly 48 h. The left part of the image shows lamellar structures.

5.1.2 Crossed Pits and Holes

After the initial geometrical characterization of the nanowires, an attempt was made to prepare grids composed of several wires. Since the wire diameters are smaller then the wavelength of visible light, special diffraction effects were expected to occur when irradiating this type of nanogrid.

_ds_-NiAl-Re pit A first attempt at creating a crossed pit involved the use of a scanning droplet cell (SDC) [160, 161]. This was achieved by using a simplified version of the SDC on a longitudinally cut sample of *ds*-NiAl-Re. In the original version the SDC contains a full electrochemical set-up. A small capillary was prepared as described in section 4.3 and mounted into an acrylic block. The block also contains a reference electrode and a counter electrode and channels that connect the electrodes and the capillary tip with an electrolyte supply. Since a purely chemical disgestion of the matrix was performed, the capillary was filled with the H_2O / HCl / H_2O_2 solution mentioned above, eliminating the necessity for the electrochemical accessories. In this case, a capillary with a tip diameter of approx. 100 µm was employed, mounted in an acrylic block and only the electrolyte supply channel was used. The capillary tip was coated with a thin layer of silicone in order to guarantee good sealing between the capillary and the *ds*-NiAl-Re substrate. The silicone was applied to the tip by dipping the capillary into a thin layer of silicone on a glass substrate and blowing nitrogen gas through the capillary in order to prevent blockage.

The capillary was filled with etching solution from the supply channel and set down on the sample. After 10 minutes, the capillary was removed and the sample surface was rinsed and investigated using SEM. A selectively etched pit had formed under the capillary tip. The pit is shown in fig. 5.10.

_ds_-NiAl-Mo hole A grid comprised of nanowires was prepared from a *ds*-NiAl-Mo sample. The sample was cut in such a manner as to obtain longitudinal wires. Next, a rod with a diameter of 3 mm and a length of 4 cm was cut from this material. The rod was then sliced into discs with a thickness of approx. 500 µm. These discs were mechanically ground in order to thin them down to thicknesses of approx. 150 µm. Finally, a Tenupol-2 dual-jet set-up (described in detail in section 6, p. 71) was used to selectively etch the matrix.

All three steps described here (mechanical polishing, electropolishing, dual-jet selective dissolution) were performed on the *ds*-NiAl-Mo discs described above. Selective dissolution of the matrix was performed under electrochemical conditions (1 M HCl, 250 mV SHE) using a Ag|AgCl|sat. KCl-µ-reference electrode.

The result of selective etching for 5 min is shown in fig. 5.11. Unfortunately, the exposed wires' spacing and alignment was not regular enough to see the desired diffraction effects.

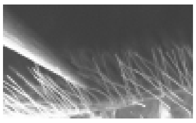

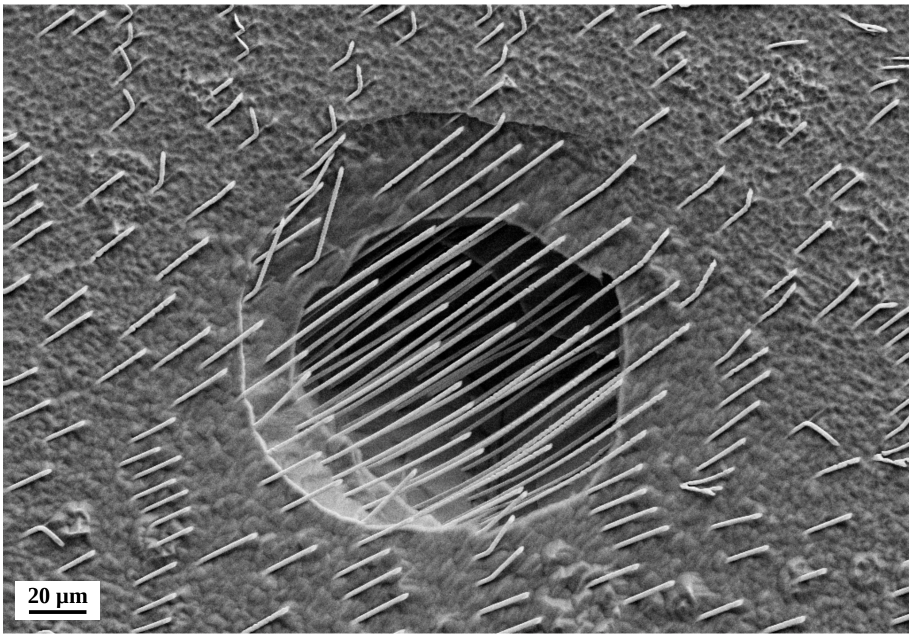

Figure 5.10: Longitudinally cut *ds*-NiAl-Re after 10 min of selective dissolution using HCl / H_2O_2-solution.

Another attempt at manufacturing a nanowire grid using single W wires is described in section 7.1 (p. 83).

5.1.3 "Bridges"

Starting from stick-shaped samples of *ds*-NiAl-*X*, an attempt was made to fabricate so-called "nanobridges". The intention was to obtain a sample with which it would be possible to easily measure the nanowire's resistivity by having very few exposed wires (some 5-20 wires, ideally only one wire) connecting two bulk ends with wires bridging the gap between two ends of the stick-shaped sample. Since the chosen material is stable at very high temperatures, heating the samples and measuring their emission of light is also feasible.

These "nanobridges" were fabricated from directionally solidified material cut into sticks with the dimensions 0.5 mm x 0.5 mm x 20 mm with the orientation of the wires parallel to the long axis of the samples. The samples were contacted at four points by soldering thin copper wires to the sticks (fig. 5.12 **A**) and then mounted to a substrate. After masking all contact points with silicone (fig. 5.12 **B**), the samples were electropolished (fig. 5.12 **C**) in order to create a

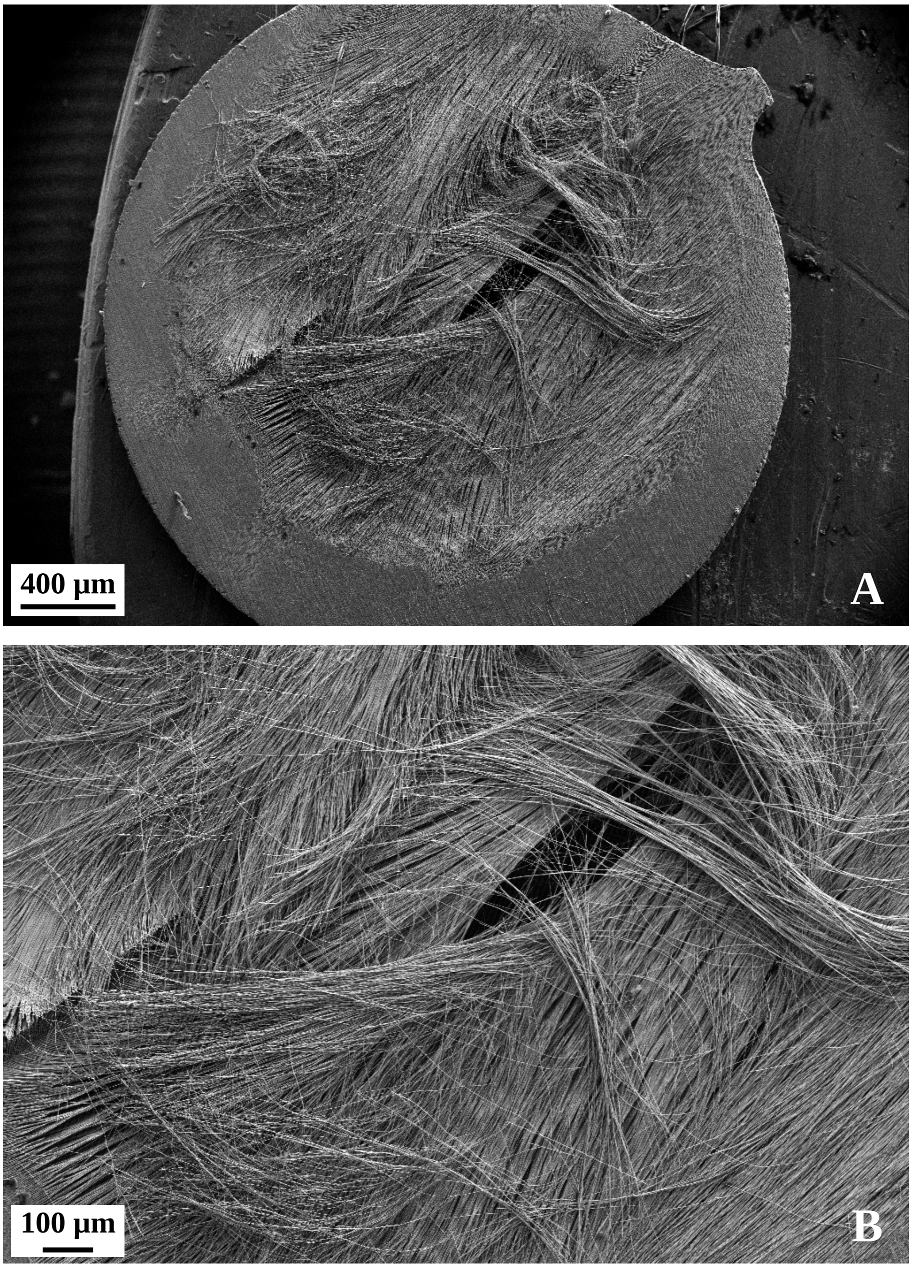

Figure 5.11: Longitudinally cut *ds*-NiAl-Mo sample after 2.5 min of selective dissolution at a potential of 250 mV SHE in 1 M HCl. **A**: Sample overview. **B**: Close-up of the hole crossed by multiple wires.

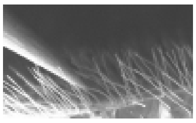

tapered shape (fig. 5.12 **D**). This was achieved by submersing the sample halfway in an electropolishing solution (CH_3CH_2COOH / $HClO_4$, p. 39) and applying a current between the sample and a Pt counter electrode in a temperature controlled cell (green leads in fig. 5.12). Galvanostatic cell currents (I_c) were applied using an analog DC power supply (Delta Elektronika, p. 35). The sample was consequently etched. Due to kinetics, the etching proceeded fastest at the boundary between electrolyte and air. Therefore, the samples became tapered during this step.

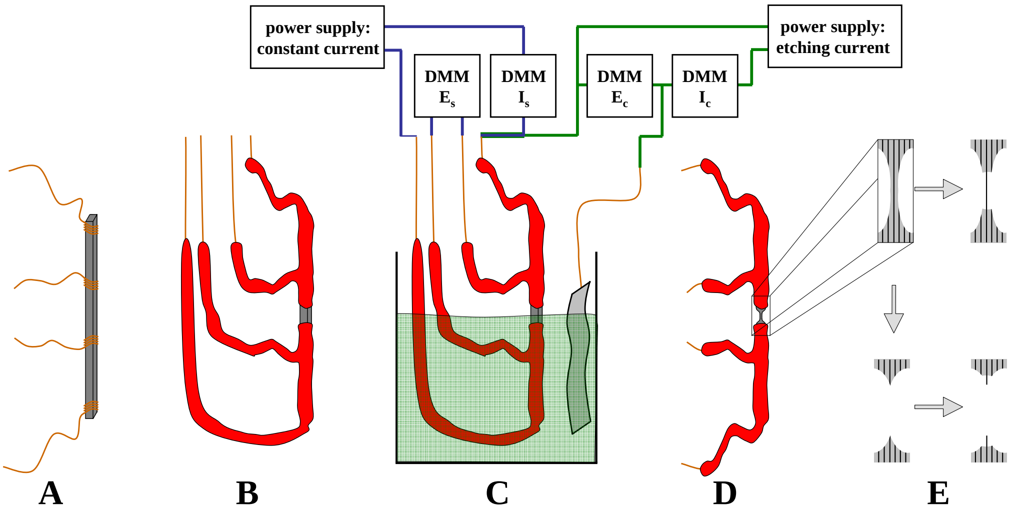

Figure 5.12: Schematic of the sample tapering process: **A**: Four copper wires are soldered to the sample. **B**: The wires are masked using silicone. **C**: The sample is electropolished. The sample resistance is monitored using a four point resistance measurement. **D**: Tapered sample. **E**: Further processing in the form of selective dissolution yields “nanobridges” or tips (s. section 5.1.4)

The aim of electropolishing was to make the tapered section of the sample as thin as possible. Since optical monitoring of the sample thickness during electropolishing was very difficult, a four point resistance measurement was performed *in-situ*. The absolute resistance of the sample is a function of its thickness, so that this parameter could be used to determine the optimum end point of electropolishing. Using an additional power supply (Voltcraft, p. 35), a constant current (I_s) of approx. 1 A was driven through the sample via the two outer leads. At the same, time the potential drop inside the sample (E_s)was measured from the two inner leads (fig. 5.12 **C**). Using Ohm’s law, it was then possible to calculate the sample resistance:

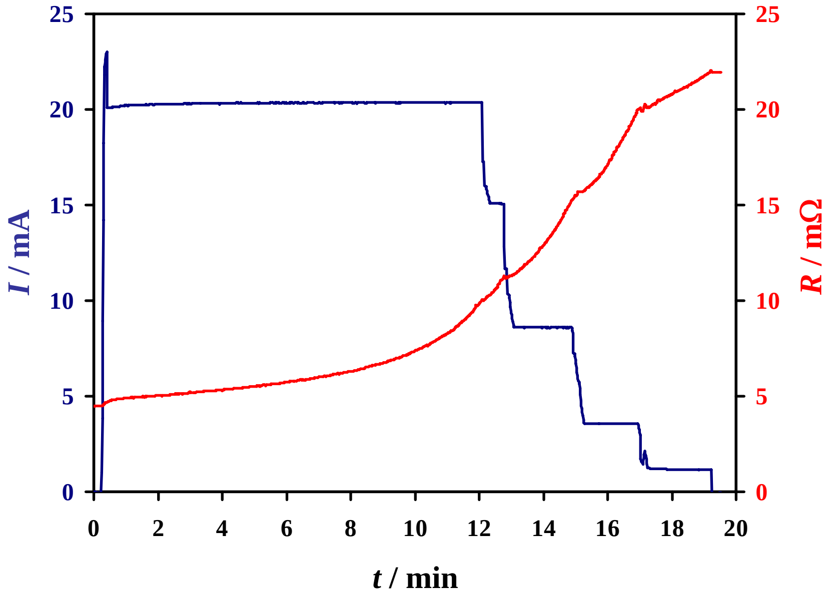

Figure 5.13: Transients of galvanostatic current (blue line) and sample resistance (red line). The current was manually controlled. The resistance was calculated from the potential drop measured by applying approx. 1 A to the *ds*-NiAl-W sample (see fig. 5.12).

$$R = \frac{E_s}{I_s} \qquad \text{eq. (5.1)}$$

All data was logged using digital multimeters (Solartron / Schlumberger DMM 7150plus, p. 35) which were in turn connected to a PC and controlled with a self-written LabVIEW program. Data logged while etching a *ds*-NiAl-W sample is shown in fig. 5.13. The blue curve shows the current profile. The applied current was controlled manually. The red curve shows the sample resistance calculated from eq. (5.1).

Data logging was initiated and after 20 s the sample current I_s was set to 20 mA. Following an initial etching period, the sample resistance rose exponentially while a constant current was applied. This meant that the critical phase of etching (toward the end of the experiment, when the samples were very thin), would pass very quickly. Therefore, the etching current I_c was reduced every time the increase in resistance became steep. This can be seen clearly from the blue line in fig. 5.13. After a little over 19 minutes, the experiment was stopped. The sample's final resistance was 21.9 mΩ, corrosponding to a thickness of approx. 10 µm.

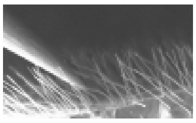

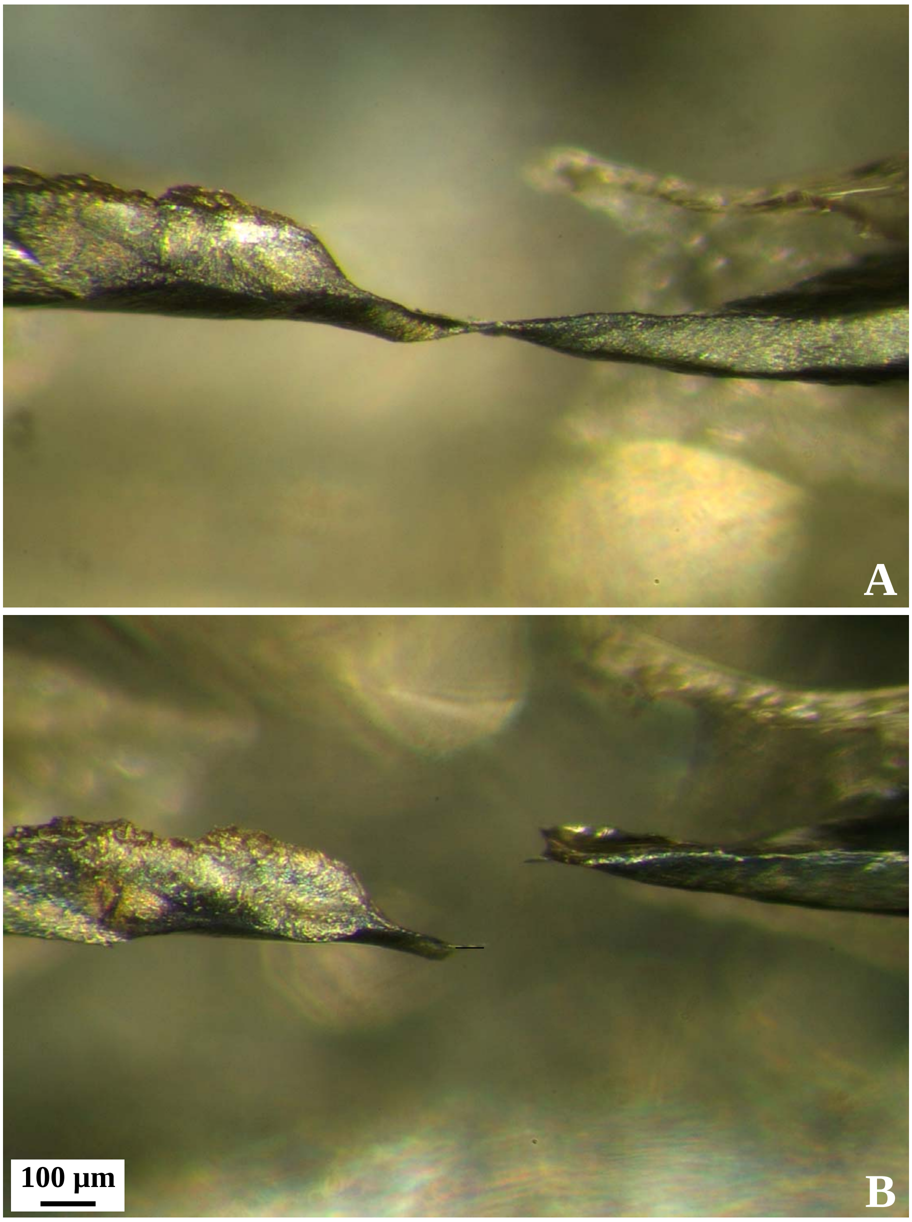

Figure 5.14: **A**: A stick-shaped *ds*-NiAl-W sample processed according to the procedures described in fig. 5.12. **B**: Removal of the matrix phase causes the “bridge” to break.

Finally, the wires were released from the matrix by selective dissolution of NiAl (fig. 5.12 **D**). Since it was also important to monitor the etching process during this step, selective dissolution was carried out in a miniature cell on the stage of the SÜSS microprober (p. 36) and could be observed using the Mitutoyo microscope. The miniature electrochemical cell consisted of a sample holder mounted to the microscope stage, a platinum wire serving as the counter electrode, and a µ-reference electrode (Ag | AgCl | sat. KCl). Both the counter and the reference electrodes were mounted to micromanipulators for easy positioning in close vicinity to the tapered sample. Selective dissolution was performed by polarizing the sample to the appropriate potential (depending on the nature of the minor phase) in a droplet of 0.1 M HCl covering the tapered section of the sample as well as the above mentioned electrodes.

The closest attempt at fabricating a bridge-type sample is shown in fig. 5.14. Figure 5.14 **A** shows the sample after electropolishing and prior to selective removal of the matrix phase. After removal of the matrix phase, residual internal stress - either from cutting or from mounting the sample - caused the sample to break as shown in fig. 5.14 **B**. The single wire which previously connected the sample is visible at the two opposing tips.

5.1.4 Tips

The most straight forward approach to utilizing a single nanowire for various applications was the fabrication of a macroscopic sample with a single wire protruding from the tip. Again, the material of interest was cut to yield stick-shaped samples (such as the ones used in section 5.1.3). When tapering the samples, as described in the previous section, it was common to “overshoot” while electropolishing and yield two tips as indicated in the lower part of fig. 5.12 **E**. An additional selective dissolution step was sufficient to release a small number of wires or even a single wire from the tips of these samples. This step was carried out by immersing the tip in 0.1 M HCl in an electrochemical cell containing a platinum foil counter electrode and a commercial Ag | AgCl | 3 M KCl reference electrode and polarizing the sample to the required potential.

A tip with multiple protruding tungsten wires is shown in fig. 5.15. In this case, all wires surrounding the most prominent one were cut away using a focused ion beam (FIB).

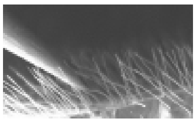

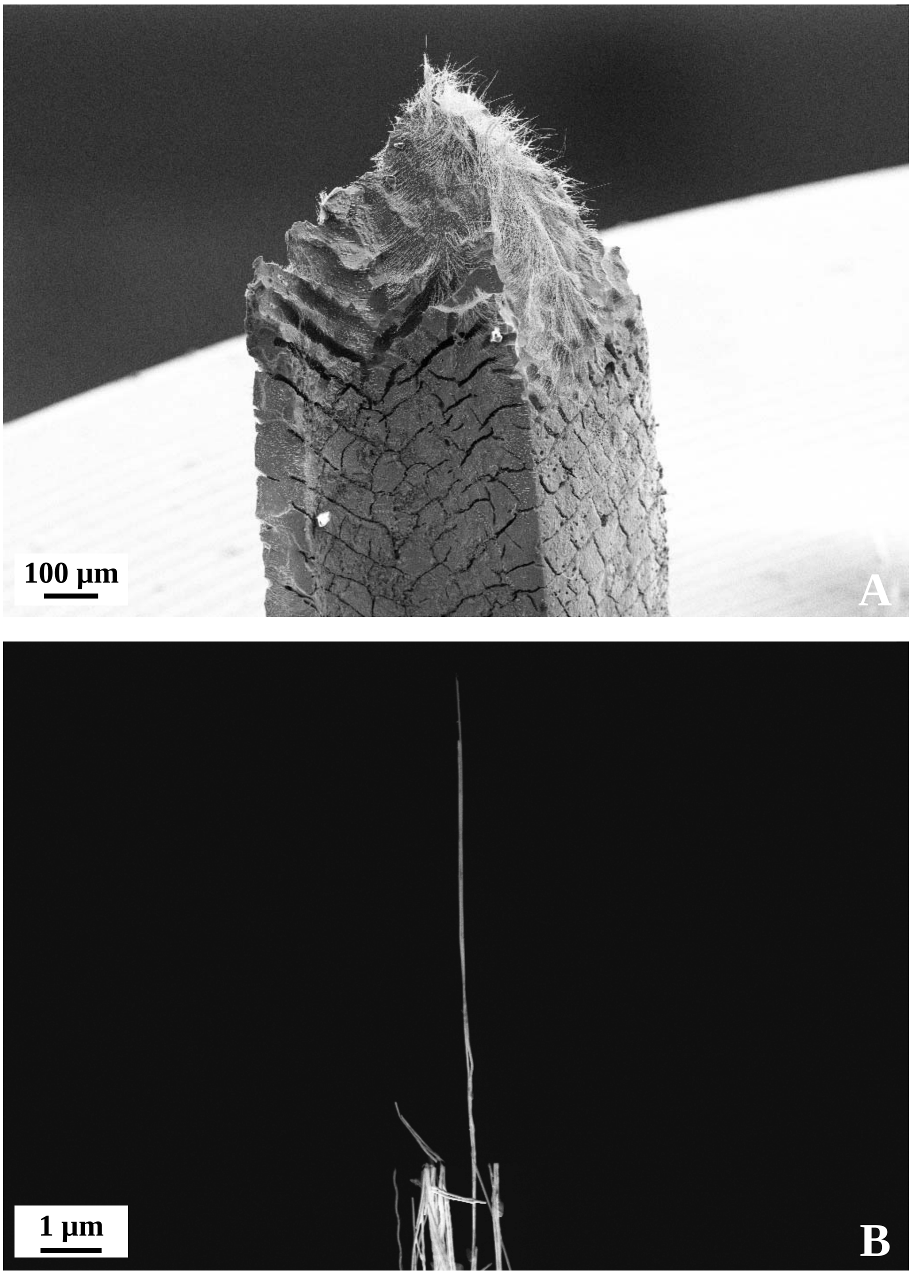

Figure 5.15: **A**: A stick-shaped *ds*-NiAl-W sample etched and processed using FIB to obtain a single tungsten wire protruding from the tip. **B**: Close-up image of the sample.

Alternatively, tips could be fabricated by partially immersing the stick-shaped samples into hydrochloric acid and polarizing them, thereby selectively dissolving the matrix. As observed in section 5.1.3, the reaction rate is highest at the three-phase-boundary. By combining this behavior with a slow upward motion of the tip, a pointed shape with protruding wires was easily achieved. In this manner, stick-shaped samples with few or single wires protruding from the tips could be prepared.

The utilization and potential applications of these samples will be discussed in sections 7.1 and 8.4.

5.2 Complete Matrix Dissolution

Preparing loose wires - completely freed from the matrix - is achieved by simply performing the procedures for selective dissolution, as described in the previous sections, but for longer periods of time. As before, there are two methods for releasing the wires: chemically, using a H_2O / HCl / H_2O_2 solution (see, e.g., section 5.1.1, p. 46) or electrochemically by applying a slightly anodic potential in a mildly corrosive electrolyte (see, e.g., section 5.1.1, p. 49). The latter method proved to be more convenient since the oxidizing power of hydrogen peroxide changes over time due to consumption during the dissolution reaction as well as side reactions.

Loose wires were prepared from nearly all alloys described in this work. Only the results for *ds*-NiAl-W will be shown in this section.

After the NiAl matrix was completely dissolved, it was necessary to separate the wires from the solution / electrolyte. This was achieved by using an ultrafiltration unit (p. 37) and cellulose acetate filter papers with a nominal pore size of 0.2 µm. Depending on the amount of wires in the solution, the filter papers showed a slightly gray or even black color after filtration. This coloration was due to the fact that large amounts of nanowires were on the filter. An image taken from the light microscope of such a filter is shown in fig. 5.16. As mentioned in section 5.1.1 (p. 51), the wires were visible under the light microscope despite their small dimensions due to the fact that their shiny, metallic surfaces scatter light. The wires appear to have larger diameters when observed under the light microscope.

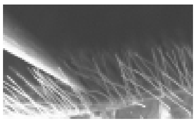

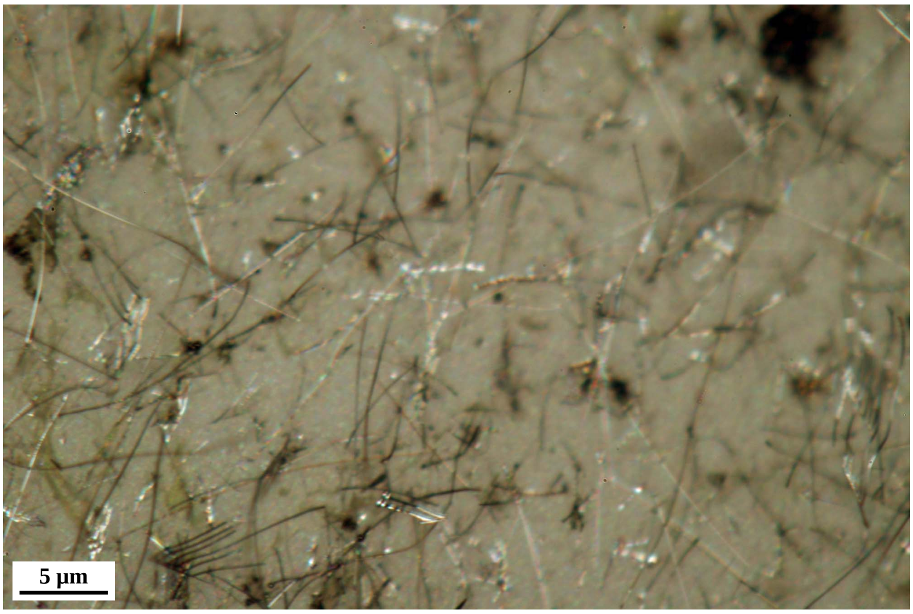

Figure 5.16: W nanowires on filter paper after complete dissolution of the matrix phase and subsequent filtration.

Mass production of nanowires - the "1 gram synthesis" As mentioned above, selective dissolution under electrochemical conditions proved to be very effective. Therefore, this method was employed for scaling-up the process in order to "mass produce" W nanowires. The initial goal was to produce 1 gram of W nanowires.

Assuming the following reactions,

$\mathrm{Al} \longrightarrow \mathrm{Al}^{3+} + 3\,\mathrm{e}^-$ and $\mathrm{Ni} \longrightarrow \mathrm{Ni}^{2+} + 2\,\mathrm{e}^-$ (*anodic reactions*)

as well as

$2\,\mathrm{H}^+ + 2\,\mathrm{e}^- \longrightarrow \mathrm{H}_2\uparrow$ (*cathodic reaction*)

it is obvious that for each mole of NiAl that is dissolved 5 electrons are produced and therefore 5 moles of H^+ ions are consumed. An estimation of the amount of hydrochloric acid required for processing 20 g of *ds*-NiAl-W was performed.

The molar mass of NiAl was calculated from the molar masses of Ni and Al [120]:

$$\begin{aligned} \mathrm{M(NiAl)} &= \mathrm{M(Ni)} + \mathrm{M(Al)} \\ \mathrm{M(NiAl)} &= 58.6934\,\mathrm{g{\cdot}mol^{-1}} + 26.9815\,\mathrm{g{\cdot}mol^{-1}} \\ \mathrm{M(NiAl)} &= 85.6749\,\mathrm{g{\cdot}mol^{-1}} \qquad \text{eq. (5.2)} \end{aligned}$$

The number of moles of NiAl, Ni, and Al is given by:

$$\begin{aligned}
\mathrm{n(NiAl)} &= \frac{\mathrm{m(NiAl)}}{\mathrm{M(NiAl)}} \\
\mathrm{n(NiAl)} &= \frac{20\,\mathrm{g}}{85.6749\,\mathrm{g{\cdot}mol^{-1}}} \\
\mathrm{n(NiAl)} &= 0.2334\,\mathrm{mol} && \text{eq. (5.3)}
\end{aligned}$$

$$\begin{aligned}
\mathrm{n(NiAl)} &= \mathrm{n(Ni^{2+}) = n(Al^{3+})} \\
\mathrm{n(Ni^{2+},\, Al^{3+})} &= \mathrm{n(Ni^{2+}) + n(Al^{3+})} = 0.4668\,\mathrm{mol} && \text{eq. (5.4)}
\end{aligned}$$

Equation 5.4 shows that the total number of moles of cations that are produced when processing this amount of material is 0.4668 mol. Due to the stoichiometry of the reactions mentioned above, this number must be multiplied by a factor of 5 to obtain the number of moles of H^+, and from that number the amount of 1 M hydrochloric acid necessary for dissolving the matrix completely:

$$\begin{aligned}
\mathrm{n(HCl)} &= \mathrm{n(Ni^{2+},\, Al^{3+})} \cdot 5 = 2.334\,\mathrm{mol} \\
\mathrm{c(HCl)} &= 1\,\mathrm{mol{\cdot}l^{-1}} \\
\mathrm{V(HCl)} &= \frac{\mathrm{n(HCl)}}{\mathrm{c(HCl)}} \\
\mathrm{V(HCl)} &= \frac{2.334\,\mathrm{mol}}{1\,\mathrm{mol{\cdot}l^{-1}}} = 2.334\,\mathrm{l} && \text{eq. (5.5)}
\end{aligned}$$

In order to accommodate this amount of electrolyte, a temperature-controlled electrochemical cell with a total volume of 2.5 l was employed. It was fitted with a gas inlet to purge the electrolyte with argon. Since processing these large amounts of material required many hours of polarization, the Luggin capillary which connected the commercial Ag | AgCl | 3 M KCl reference electrode to the cell was filled with an electrolyte (sat. KCl) which was solidified with agar. This prevented blockage of the Luggin capillary by hydrogen bubbles. A large Pt net was employed as a counter electrode. The pieces of *ds*-NiAl-W were placed in a platinum basket and processed individually. Initial currents of approx. 500 mA were measured. The dissolution current diminished gradually as the amount of residual NiAl decreased. After approx. 12 h, the current dropped to half the

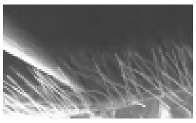

initial value; after approx. 38 h, the current dropped to one tenth of the initial value. These values correspond to a nearly linear decrease in current over time. After approx. 55 h, the current decay was complete - no further charge was consumed. The experiment was continued for several hours to ensure complete matrix dissolution. Finally, the solution was filtered using the ultrafiltration unit mentioned above.

Figure 5.17: Digital photograph of the precipitated W nanowire “fleece” partially removed from the filter paper. Close-up views of these nanowires are shown in fig. 5.18.

An estimation of the number of wires obtained was done by calculating the length of a virtual wire weighing 1 g. First the volume of tungsten V is determined from the material’s density ρ [120]:

$$\begin{aligned} V &= \frac{m}{\rho} \\ &= \frac{1\,\mathrm{g}}{19\,250\,000\,\mathrm{g{\cdot}m^{-3}}} \\ &= 5.19 \times 10^{-8}\mathrm{m}^3 \end{aligned} \qquad \text{eq. (5.6)}$$

Assuming an average wire diameter w of 200 nm, the cross-sectional surface A is calculated:

$$\begin{aligned} A &= \pi \cdot r^2 \\ &= 3.1416 \cdot (1 \times 10^{-7}\mathrm{m})^2 \\ &= 3.1416 \times 10^{-14}\mathrm{m}^2 \qquad \text{eq. (5.7)} \end{aligned}$$

The length f of a single wire with a diameter of 200 nm weighing 1 g is:

$$\begin{aligned} f &= \frac{V}{A} \\ &= \frac{5.19 \times 10^{-8}\mathrm{m}^3}{3.1416 \times 10^{-14}\mathrm{m}^2} \\ &= 1.6535 \times 10^{6}\mathrm{m} = 1653.5\,\mathrm{km} \qquad \text{eq. (5.8)} \end{aligned}$$

Assuming an average wire length g of 300 µm, the number of wires W in 1 g is:

$$\begin{aligned} W &= \frac{f}{g} \\ &= \frac{1.6535 \times 10^{6}\mathrm{m}}{3 \times 10^{-4}\mathrm{m}} \\ &= 5.5119 \times 10^{9} \qquad \text{eq. (5.9)} \end{aligned}$$

Therefore, the estimated number of tungsten nanowires in 1 g is approx. 5.5 billion.

The solid phase obtained from filtration solely consisted of W nanowires. These formed a sort of “fleece” that could be handled with “bare hands”, i.e. using tweezers but without the help of special tools (fig. 5.17). Figure 5.18 gives an impression of the quantity of wires obtained. It should be noted that the wires shown in fig. 5.18 are only a small fraction of the total amount of wires obtained in these experiments. All in all, the total amount of wires produced was 0.98 g.

Compositional analysis An added benefit of entirely dissolving well-defined amounts of directionally solidified material was the possibility to carry out compositional analyses

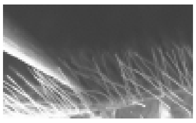

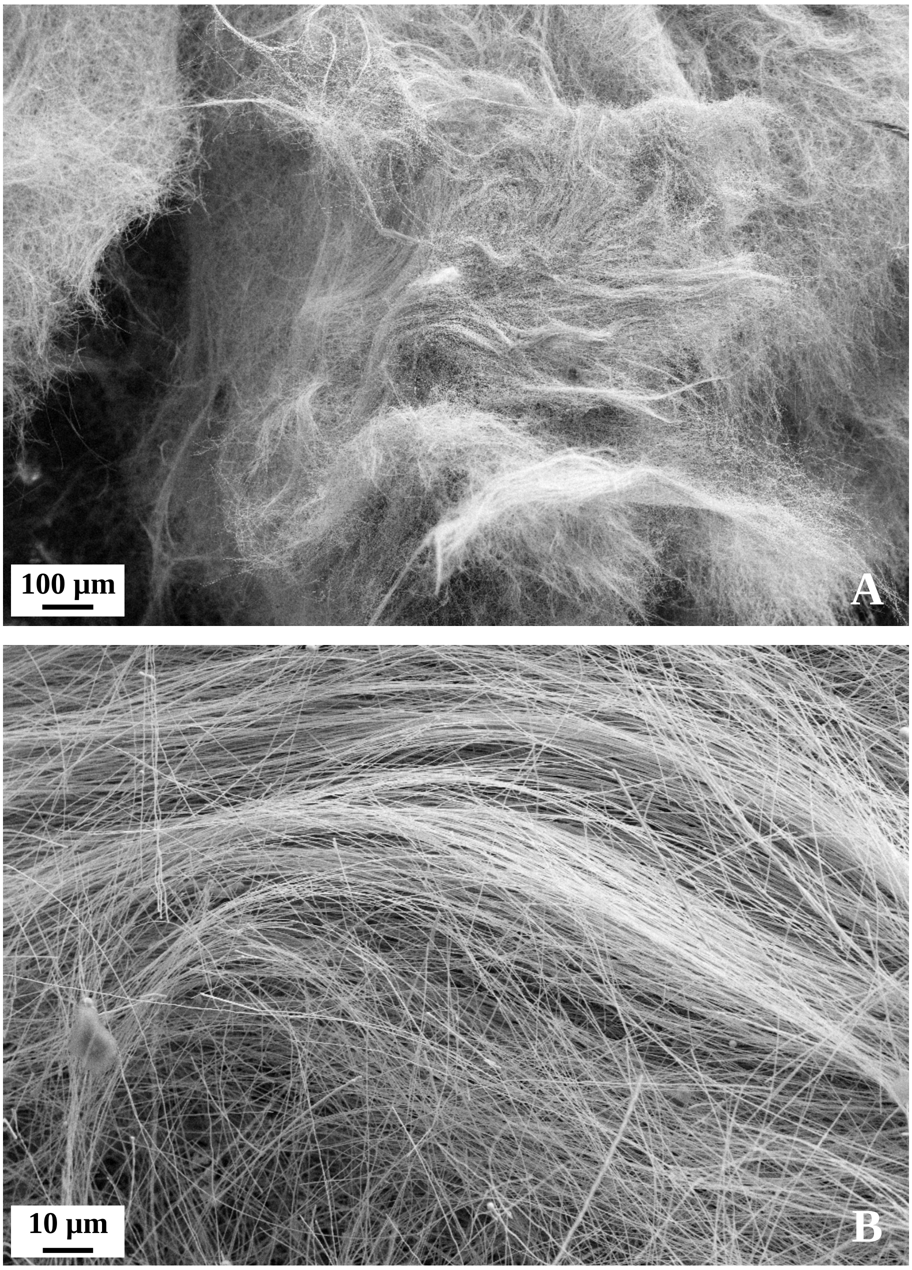

Figure 5.18: Large amounts of W nanowires. **A**: A surface of approx. 1 mm^2 covered by a “fleece” of W nanowires. **B**: Close-up view of free W nanowires; the wires’ extreme aspect ratios are shown nicely in this image.

It was of interest to find out whether the applied conditions for selective dissolution were really *selective*. Also, it was of interest to determine the amount of residual matrix material in the obtained wires. These values were determined by performing trace analysis using optical emission spectroscopy in an ICP-OES (p. 38). Analysis of the electrolyte used for selective dissolution showed a content of 0.04 % W. This value is consistent with the expected value of the solubility of tungsten in the matrix phase. Residual tungsten atoms or small clusters of tungsten released from the matrix during selective dissolution will have slipped through the filter paper and therefore one would expect to find these amounts of tungsten in the filtrate.

After disintegration of the wires taken from the filter paper, chemical analysis was performed showing residual contents of 0.17 % and 1.38 % for Ni and Al, respectively. These values are most probably due to residual, undissolved matrix or residual nickel and aluminum salts in the sample.

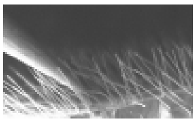

6 Selective Wire Dissolution

The treatments of the directionally solidified samples described so far were all focused on releasing the nanoscopic wires from the surrounding matrix, yielding wire arrays. The reverse approach - dissolving the wires while leaving the matrix intact - yields arrays of pores. This approach will be described in this chapter.

Analogous to the procedures described in chapter 5, selective dissolution of the minor phase is achieved by applying conditions which will corrode the minor phase. In the case of the silver-copper system, the chosen electrochemical conditions are within the region of immunity for silver. Processing the nickel-aluminium based alloys was performed at conditions that corrode the wires while simultaneously passivating the matrix. The appropriate conditions were again determined by studying the Pourbaix diagrams discussed in section 3.4.3. The wires were always dissolved in acetate buffer solutions while applying mildly anodic potentials. The applied potential depended on the minor element being investigated. This treatment allowed Mo, Re, W, or Cu to be dissolved while retaining the matrix.

6.1 Partial Wire Dissolution

Treating samples in the above mentioned manner yielded arrays of nanopits. Since the pits were created by removing the fibrous phase from the material, the same rules concerning diameter and spacing discussed for the wires apply. In contrast to matrix dissolution, the etching time does not give such precise control over the pore depth. Where it was shown that polarization for extended periods of time yielded complete dissolution of the matrix phase, the dissolution of the fibrous phase stagnates after a relatively short time. This is probably due to a build up of dissolved metal ions in the pore. A high concentration of cations in the pore provides a counter balance the driving force for further dissolution. A typical wire dissolution transient will be discussed below.

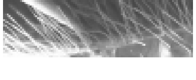

***ds*-NiAl-W** The *ds*-NiAl-W system yielded well-ordered arrays of nanopits with pit diameters of roughly 200 nm as shown in fig. 6.1. Figure 6.1 **A** shows a section of approx. 600 µm^2; the residual scratches from grinding the sample show that the matrix material is not corroded under the chosen conditions (acetate buffer, pH 6.0), anodic polarization to 200 mV SHE). Figure 6.1 **B** shows a close-up view of a single nanopore.

As mentioned above, the dissolution of the wire phase is not a continuous process as it is in the case of dissolving the matrix. A typical current transient recorded while polarizing a *ds*-NiAl-W sample to 200 mV SHE in acetate buffer is shown in fig. 6.2. The current drops from an initial current of 35 µA to a current of 5 µA within the first 100 s of the experiment. After a little over 5 h of polarization, the current drops further to values under 1 µA [159].

After leaving the sample at its open circuit potential (0.035 V SHE) for 10 min, the potential was stepped to 0.5 V SHE and held for 30 h. The given pH provides optimum conditions for the passivation of Al

$$2\,\mathrm{Al} + 3\,\mathrm{H_2O} \longrightarrow \mathrm{Al_2O_3} + 6\,\mathrm{H}^+ + 6\,\mathrm{e}^- \qquad \text{eq. (6.1)}$$

whereas nickel, the second matrix element, would still corrode according to eq. (6.2).

$$\mathrm{Ni} \longrightarrow \mathrm{Ni}^{2+} + 2\,\mathrm{e}^- \qquad \text{eq. (6.2)}$$

Aluminum is a valve metal that can form very thick oxide layers. Under these conditions, one would expect a dealloying that causes an enrichment of the aluminum on the surface resulting in an aluminum oxide film on top of the equiatomic NiAl alloy. At the same time tungsten and tungsten oxide are dissolved according to the following chemical equations:

$$\mathrm{W} + 3\,\mathrm{H_2O} \longrightarrow \mathrm{WO_3} + 6\,\mathrm{H}^+ + 6\,\mathrm{e}^- \qquad \text{eq. (6.3)}$$

$$\mathrm{W} + 4\,\mathrm{H_2O} \longrightarrow \mathrm{WO_4^{2-}} + 8\,\mathrm{H}^+ + 6\,\mathrm{e}^- \qquad \text{eq. (6.4)}$$

$$\mathrm{WO_3} + \mathrm{H_2O} \longrightarrow \mathrm{WO_4^{2-}} + 2\,\mathrm{H}^+ \qquad \text{eq. (6.5)}$$

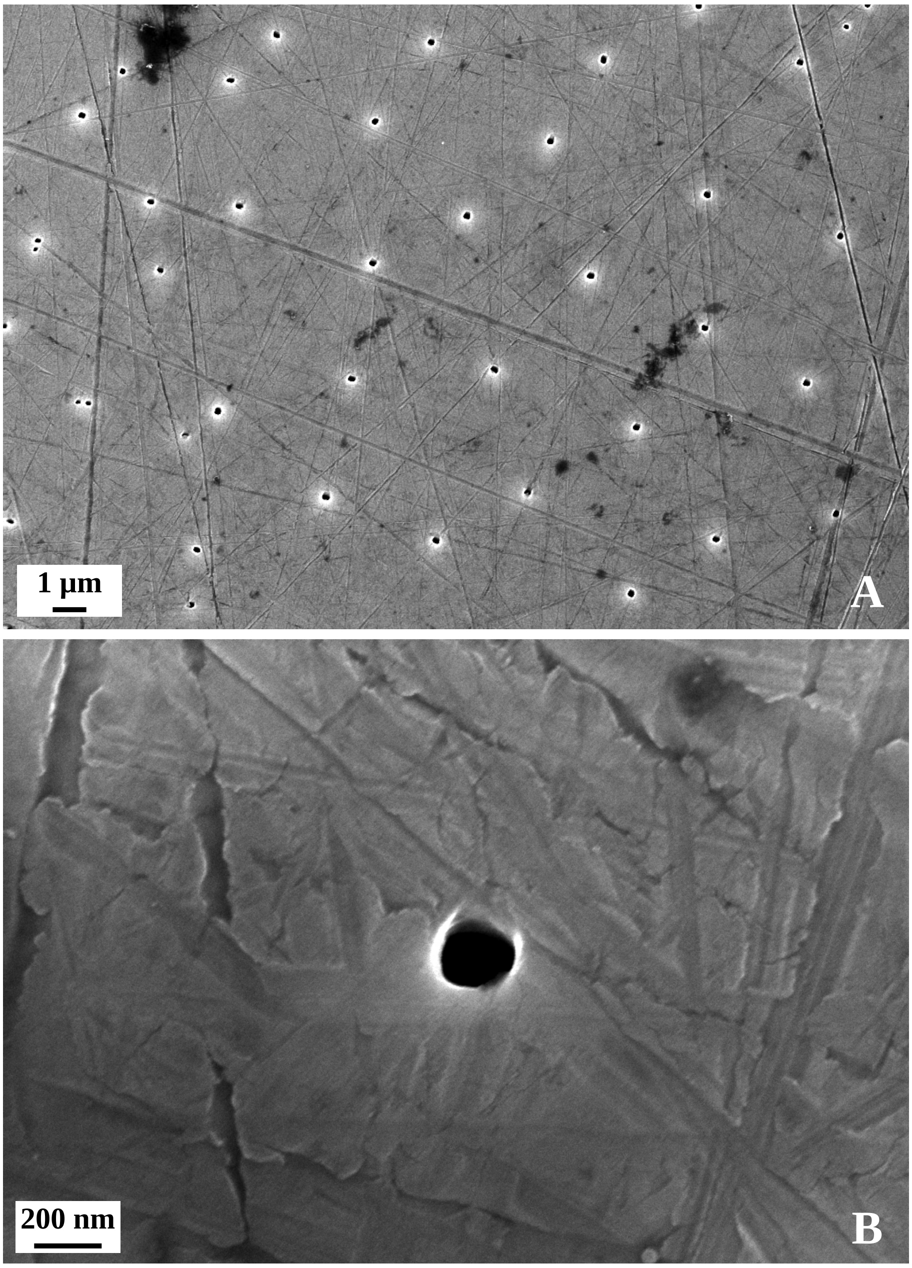

Figure 6.1: Nanopits in *ds*-NiAl-W. **A**: Pore array; the visible scratches - resulting from grinding - are visible, proving that the matrix is not corroded. **B**: Close-up view of a single pit with a diameter of approx. 200 nm.

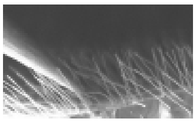

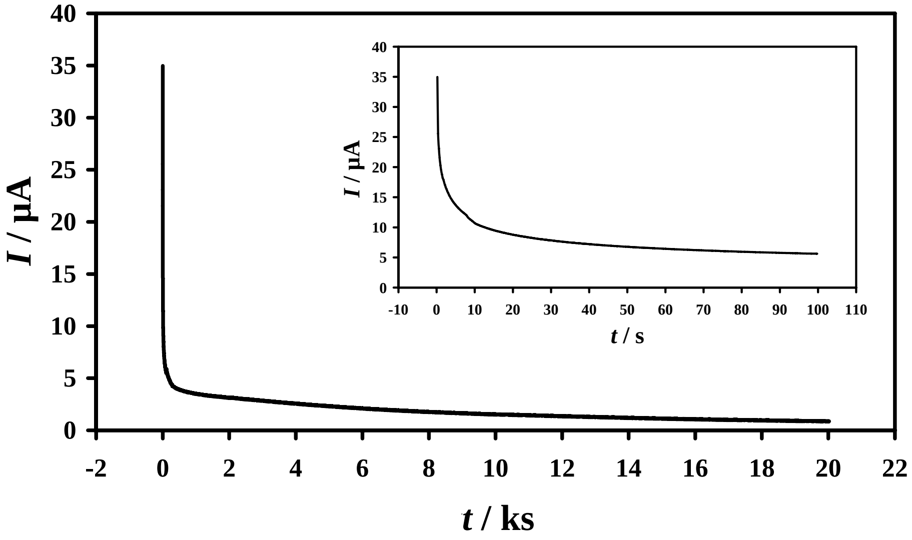

Figure 6.2: Current transient of selective tungsten dissolution; the inset shows a close-up of the first 100 s.

Figure 6.1 **A** shows a SEM image of a *ds*-NiAl-W sample after this treatment. Pores are formed in the channels of the embedded tungsten wires. The pores are evenly distributed across the surface. The surface shown has a size of 511 µm^2, which corrosponds to a wire density of 8×10^{10}m^{-2}. Small scratches on the matrix resulting from the grinding are still visible demonstrating that the matrix does not dissolve. A closer view into one of these pores is shown in fig. 6.1 **B**. The cross-section shows that the hole is slightly elongated in one direction; the longer pore diameter is 245 nm and the shorter 170 nm. The two longer walls appear parallel; a strong hint of the faceted nature of the wire-matrix interface. A surface ratio of 0.3 %W is calculated from these results. On average, each pore has an area of 12 µm^2. All these values are important geometrical factors for the application of these electrodes as sensors in electroanalytical chemistry.

Figure 6.3 shows the current transient recorded during polarization. The potential jump causes the simultaneous dissolution of nickel and tungsten according to eqs. 6.2 and 6.4 while passivating aluminum (eq. (6.1)). This is indicated as region A in fig. 6.3.

Aluminum oxide is known to grow according to the high field model. This implies a -1 slope in a double logarithmic plot of current over time. Such a slope is not observed since all three processes occur simultaneously and the time resolution is insufficient to see the very early stages, which are probably dominated by the passivation current.

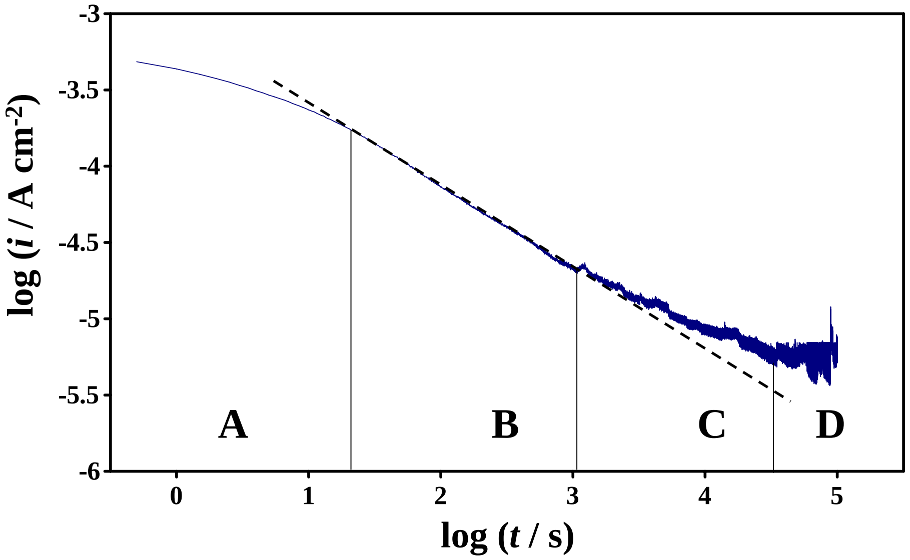

Figure 6.3: Double logarithmic current transient of the electrodissolution of *ds*-NiAl-W eutectic alloy during selective electrodissolution of the tungsten phase in acetate buffer (pH 6.0) at 0.5 V SHE for 30 h.

A direct comparison to a high resolution current transient of pure aluminum in an acetate buffer from the literature gives important information [133]. It shows that Debye charging of the oxide, dielectric relaxation of the oxide, charge carrier emission from the interfaces and initial high field oxide growth already take place during the first second after stepping the potential to 0.5 V SHE. As a result of this self-inhibiting process, the current density is in the range of 1 mA·cm^{-2} and must be expected to further decrease with a -1 slope. It thus falls below the current observed for the *ds*-NiAl-W alloy in region B.

This means that the alloy is already significantly passivated at the very beginning of the transient shown in fig. 6.3. In region B of the transient, the slope of the curve is almost exactly -0.5 indicating a diffusion-controlled process. It is most likely that tungsten is initially dissolved according to eq. (6.4). This will create pores and a significant acidification in these pores, and thus a shift in the equilibrium of eq. (6.5) to the left side.

For anodic potentials, the Pourbaix diagram in fig. 3.10 (p. 31) shows a vertical equilibrium line for eq. (6.5) at pH 4.0. The diffusion of protons into the bulk solution is linked to an increase of the pH within the pore. This shifts the equilibrium in eq. (6.5) toward the soluble WO_4^{2-}. With increasing pore depth, the diffusion length increases as well. This leads to a further decrease in current. After 1000 s, the slope becomes flatter and flatter in region C, indicating that

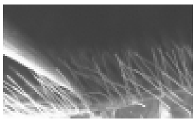

the current density of the stationary aluminum oxide corrosion becomes more and more predominant. Finally, in region D, the current becomes constant - a phenomenon well known from pure aluminum [133].

_ds_-NiAl-Re Preparing pore arrays in *ds*-NiAl-Re was achieved by polarizing the samples in acetate buffer at a potential of 200 mV SHE [74]. A typical result is shown in fig. 6.4.

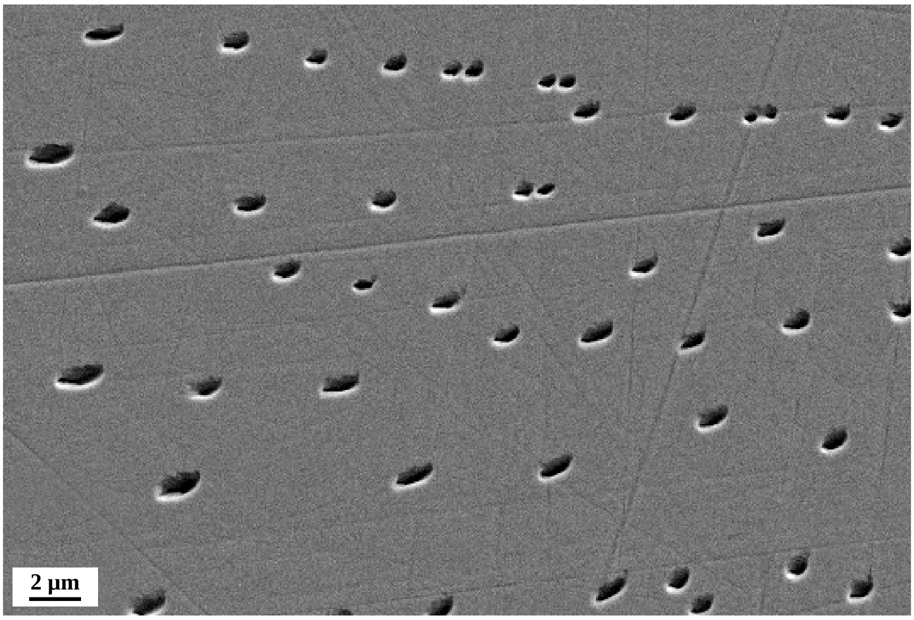

Figure 6.4: Pore array obtained from selective dissolution of the wire phase of a *ds*-NiAl-Re sample

It should be mentioned here that other researchers within the project frame work have established some very interesting micro-/nanostructures using *ds*-NiAl-Re material. One of these structures consisted of gold hemispheres electrochemically deposited onto the rhenium wires yielding arrays of mushroom-like structures of sub-microscopic dimensions [162].

_ds_-NiAl-Mo In the case of selectively dissolving the fibrous phase, the *ds*-NiAl-Mo system was studied most extensively. Again, the minor phase was dissolved by polarizing the samples to 200 mV SHE in acetate buffer. Polarizing for shorter periods of time yielded partially dissolved wires as shown in fig. 6.5.

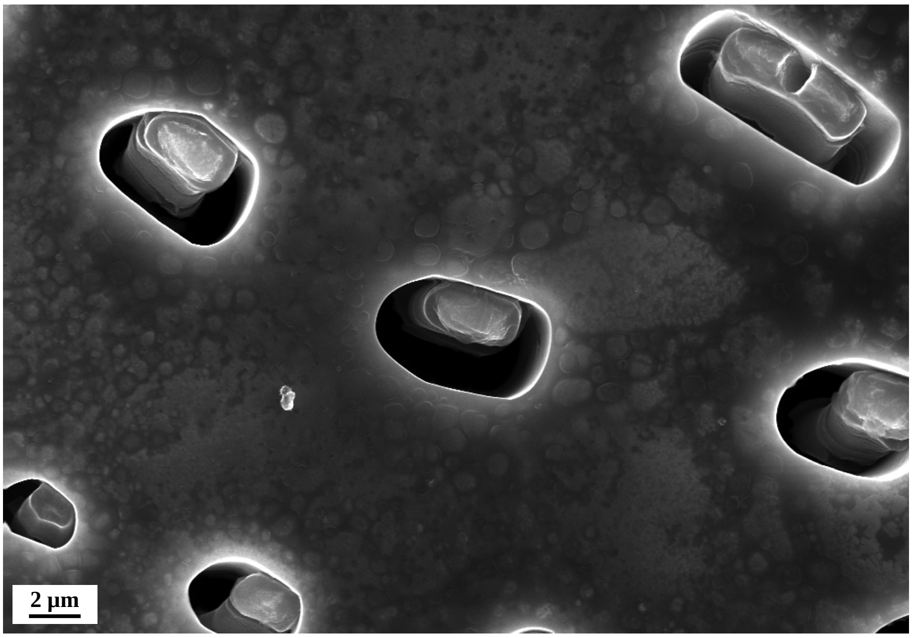

Figure 6.5: Selective dissolution of the wire phase of a *ds*-NiAl-Mo sample; the wires are partially dissolved.

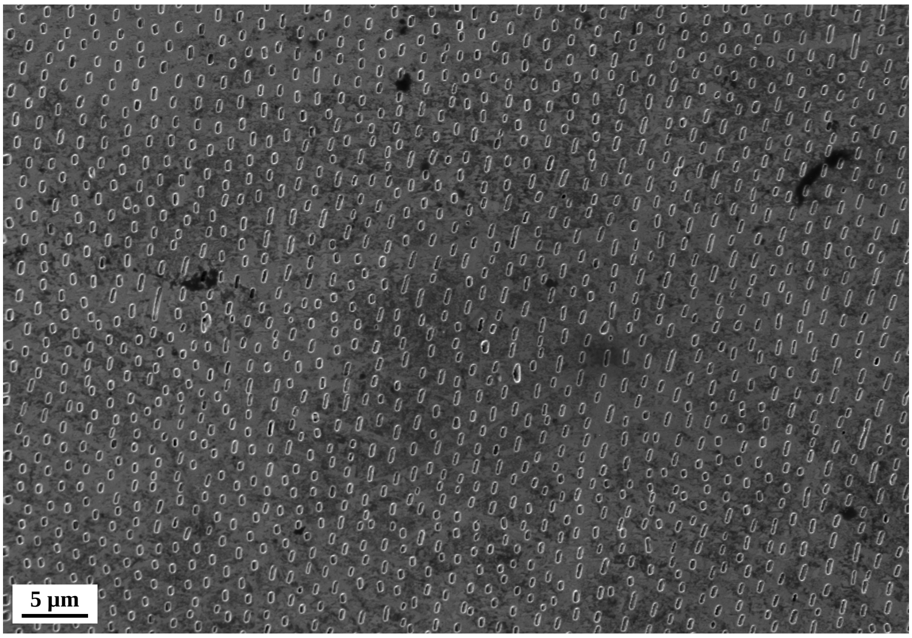

Figure 6.6: Selective dissolution of the wire phase of a *ds*-NiAl-Mo sample yields arrays of nanopores.

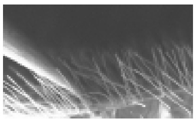

As in the case of *ds*-NiAl-W and *ds*-NiAl-Re, the dissolution currents stagnated after the first few minutes of polarization. The obtained pore arrays are shown in fig. 6.6.

Further results on selectively dissolving molybdenum from *ds*-NiAl-No will be discussed in section 6.2.

***ds*-Ag-Cu** Selective dissolution of the copper phase was achieved by polarizing the directionally solidified material to 500 mV SHE in acetate buffer. As can be seen from the combined Pourbaix diagram for silver and copper (fig. 3.13, p. 32), the chosen conditions lie within the region of immunity for silver and within the region of corrosion for copper. In this case, the matrix is not passivated, as it is when processing the nickel-aluminum based alloys. The obtained pores were relatively large with diameters of approx. 700 nm.

Both phases are pure elements in the copper group, the first sub group of the periodic table, and therefore possess high nobility. The greater nobility of silver made the selective dissolution of copper relatively straightforward. The dissolution is assumed to occur by the direct oxidation of the copper at a potential insufficient for oxidizing the silver. As the acetate salts of both metals are sufficiently soluble, no layers formed to coat the surfaces of the metals. Dissolution proceeded with the sky-blue tinting of the electrolyte characteristic of hydrated cupric cations [99].

6.2 Complete Wire Dissolution

Besides fabricating pore arrays, an attempt was made to completely dissolve the wire phase, thus yielding an array of holes - a nanofilter.

As described in the previous section, the dissolution of the wires tended to stagnate after relatively short periods of time. Therefore, attempts at fabricating hole arrays were performed on ultra thin samples. Preparing these ultra thin samples was achieved using techniques established for the preparation of samples for transmission electron microscopy.

The initial step consisted of cutting the samples into pieces of the required dimensions. In this case, disc-shaped samples with the wires oriented perpendicular to the disc plane were cut. The discs were approx. 3 mm in diameter and

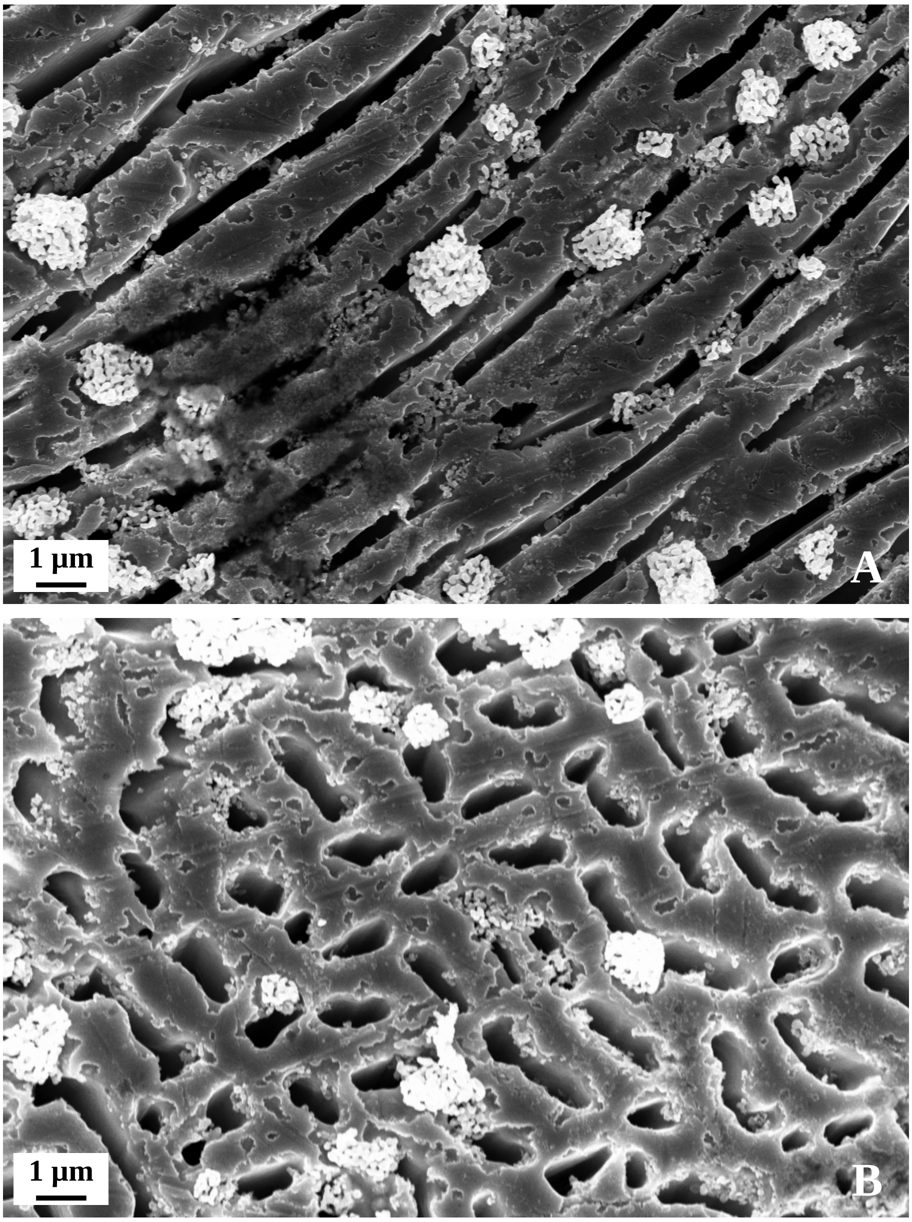

Figure 6.7: Microstructure of a *ds*-Ag-Cu sample after selective dissolution of copper. **A**: A eutectic cell with lamellar structures. **B**: A eutectic cell with fibrous structures.

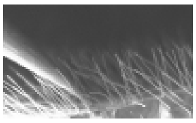

slightly under 1 mm thick. The samples were mechanically ground with emery papers of 1000 and 4000 grit. This was achieved by gluing them to a sample holder fitted with a micrometer screw. In this manner, the sample thickness could be controlled while grinding. After the sample thickness was reduced to about half the initial value the samples were turned around, in order to yield a smooth finish on both sides of the disc. The final thickness of the samples was between 100 µm and 150 µm. Further thinning was achieved using an electropolishing set-up:

The Tenupol-2 manufactured by Struers (s. section 4.1.5 on p. 37) is used to further thin samples by placing them in between two jets of electropolishing solution and applying a constant current. Electrodissolution occurs, forming bowl-shaped recesses on both sides of the sample. In the case of transmission electron microscopy this process is continued until a very small hole is formed in the center of the sample. The TEM measurement is then performed on the perimeter of this hole. In the case of fabricating nanohole arrays it was necessary to avoid making a large hole in the sample while achieving a very small sample thickness at the same time. Since the etching rates were different for the grains and the grain boundaries and since slight alterations in the experimental conditions had a large effect on the etching speed, this was very hard to realize.

The second step in making nanohole arrays (or nanofilters) consisted of selectively dissolving the wire phase as described in the previous section. It was convenient to utilize the same sample holder used during thinning for the dissolution step, so as not to damage the very fragile ultra thin samples. Electrochemical polarization of these samples was made possible by fitting the Tenupol-2's sample holder with a µ-reference electrode and switching from electropolishing solution to an appropriate electrolyte for selective dissolution.

A schematic representation of the modified sample holder is shown in fig. 6.8. The sample holder is made of two Teflon pieces that snap into each other. One side of the sample holder is fitted with a platinum strip which is used to contact the sample. The sample is placed over the hole in the platinum strip and the other side of the sample holder is snapped in to place. This part of the sample holder was modified to hold a µ-reference electrode. Once the sample holder was assembled, it was placed in to the Tenupol-2 device, which was fitted with two counter electrodes (also made from platinum). After connecting all electrodes to a potentiostat, electrochemically-driven dissolution of the wire phase commenced under constant flow of acetate buffer electrolyte.

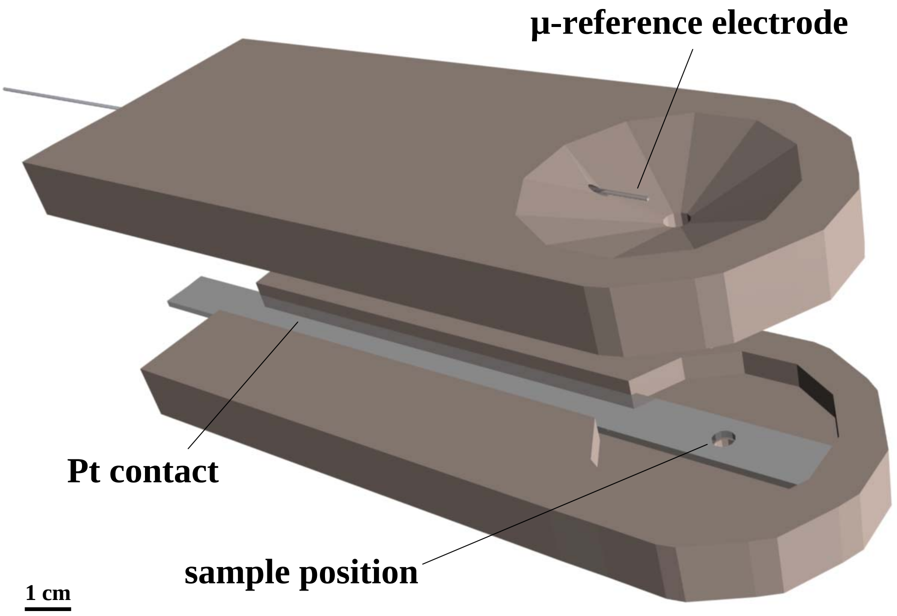

Figure 6.8: Schematic of the Tenupol-2 sample holder fitted with a µ-reference electrode.

Unfortunately, none of the attempts in fabricating a hole array was successful. The result of the most successful experiment is shown in fig. 6.9. The sample ruptured during handling, while transferring it from the Tenupol-2 sample holder to the SEM sample stage. Figure 6.9 **A** shows the entire grain located in the sample center. Figure 6.9 **B** shows a close-up view of the sample center - the hole array is visible.

The experiments described in this section show that the fabrication of filters with nano-sized pores is feasible using ultra thin samples. Furthermore, optimizing the (electro-)chemical conditions used for selective dissolution of the wires may lead to deeper pores as well as nanofilters from slightly thicker, more sturdy samples.

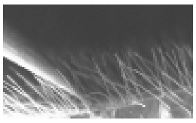

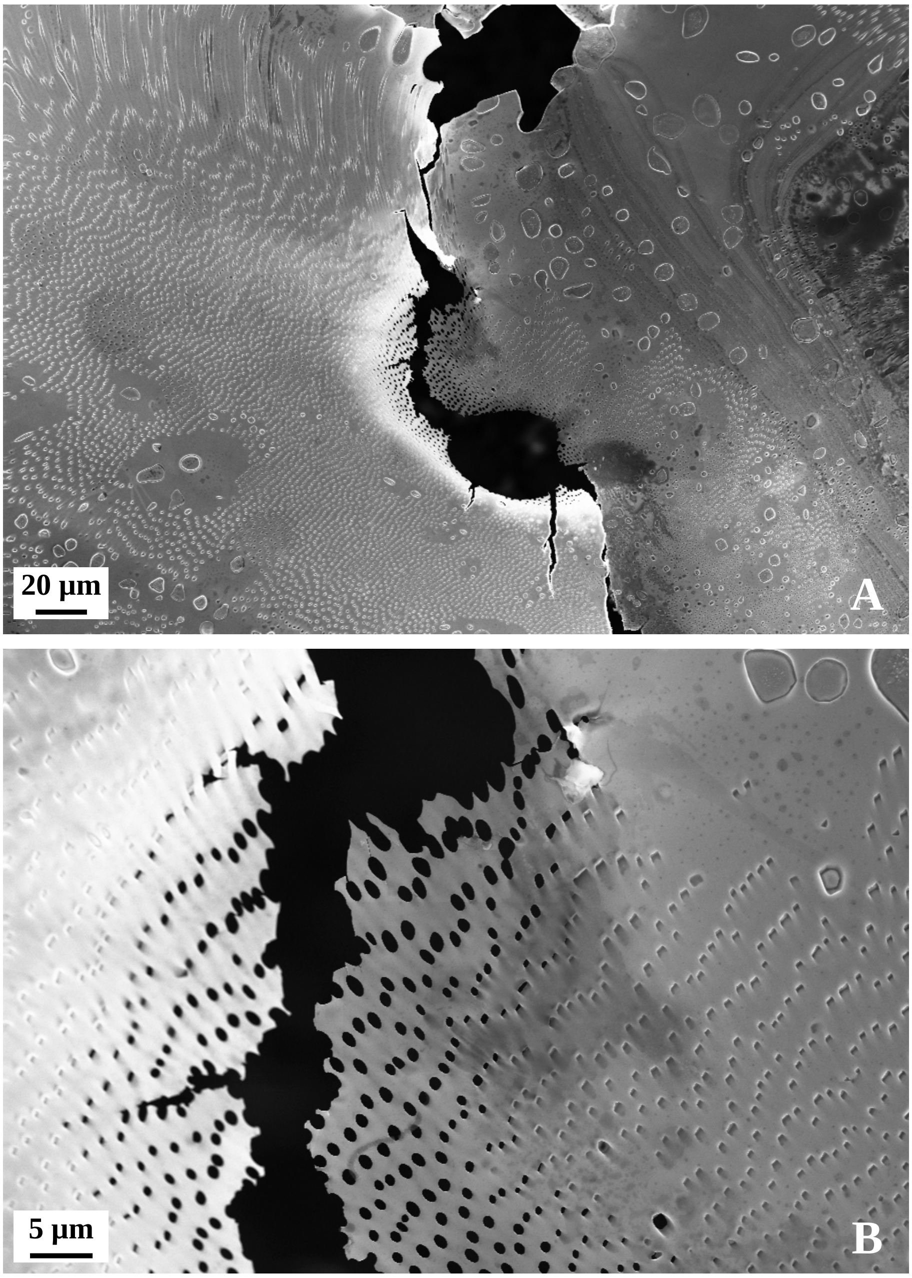

Figure 6.9: SEM images of an ultra thin *ds*-NiAl-Mo sample. **A**: Unfortunately, the sample ruptured during handling. **B**: Close-up view of the sample center; the hole array is visible.

7 Experimental Procedures Subsequent to Electrochemical Processing

The previous chapters showed a sampling of the multitude of structures obtainable from electrochemical processing of directionally solidified eutectic alloys. Further experiments involving various techniques were performed to characterize the materials and further explore the properties and possibilities of the obtained structures. These experiments will be described in the following sections.

7.1 Manipulation

This section lists all experiments involving the use of micro and nanomanipulators as well as the focused ion beam technique to handle, arrange or modify single nanowires.

The employed micromanipulators (see section 4.1.4, p. 36) consist of three sleds arranged along the three axes of motion (x, y, z) which are positioned using micrometer screws. A wide range of tools can be mounted to the arms of these manipulators. In most cases, fine tips were used to probe small features, either for pushing single nanowires into position or probing contacts for electrical measurements.

The Kleindiek manipulators give access to even smaller features. Their total range of motion overlaps with that of the SÜSS micromanipulators, but with much higher precision. While operating these piezo-driven manipulators under the light microscope, it was useful to place the nanomanipulators onto the

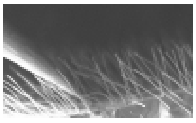

micromanipulators for easy initial positioning. On the other hand, the nanomanipulators offered the possibility of manipulating wires in the scanning electron microscope [163].

The focused ion beam (FIB) was used to prepare, mount, and mark samples for various applications. The FIB is also fitted with a gas inlet system (GIS) for introducing precursor gases which disintegrate under ion beam radiation. This disintegration leads to the precipitation of various compounds - depending on the nature of the precursor. Deposition should occur solely within the irradiated area designated by the user. In this work, platinum was deposited from trimethyl(methylcyclopentadienyl)platinum(IV), the structure of which is shown to the right [164]. The results of these experiments will be described in the following sections.

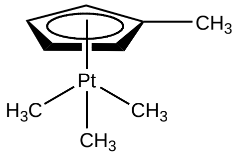

7.1.1 Utilizing Single Nanowires

As discussed in section 5.2, large amounts of nanowires could easily be fabricated. Transferring wires to silicon wafer substrates was achieved by simply pressing the wafer against the filter paper containing free nanowires.

After transferring the wires to the silicon wafers, it was possible to move the wires around on the silicon surface using micromanipulators equipped with Picoprobe tips (see section 4.1.4). Using four of these tips, an attempt was made to measure the resistivity of a single tungsten nanowire. Figure 7.1 shows a light microscope image of the four point measurement set-up. Unfortunately, the contact resistance between the probe needles and the nanowire was very high. Therefore, no useful data was produced during this measurement.

Similar attempts were made using the Kleindiek manipulators inside the SEM. In this case, a much more precise positioning of the needles was possible. Unfortunately, the high contact resistance between the probing needle and the nanowires again prohibited successful measurements. An attempt at overcoming this problem is described in section 7.1.3.

7.1.2 Mounting Single Nanowires to TEM Substrates

Using the Kleindiek manipulators, single wires were transferred to TEM grid substrates for further investigation of the material properties (fig. 7.2). Due to

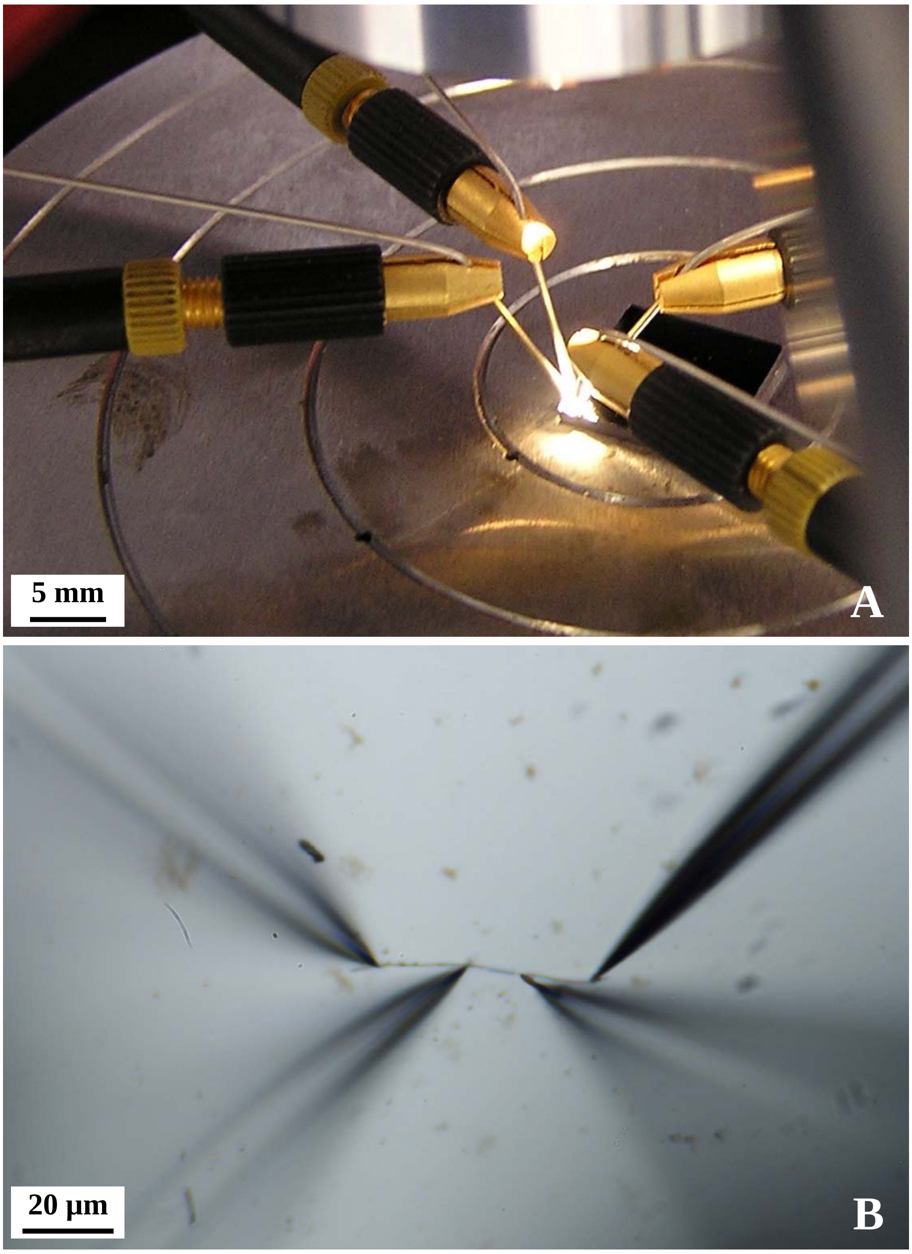

Figure 7.1: **A**: Digital photograph of the four manipulator arms, each holding a Picoprobe. **B**: Light microscope image of a single nanowire in contact with four Picoprobe needles.

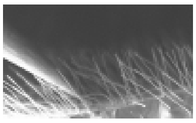

their relatively high density, the refractory metal nanowires were not suited for transmission electron microscopy; even the thinnest tungsten nanowires with diameters under 200 nm were not transmissive for the electron beam.

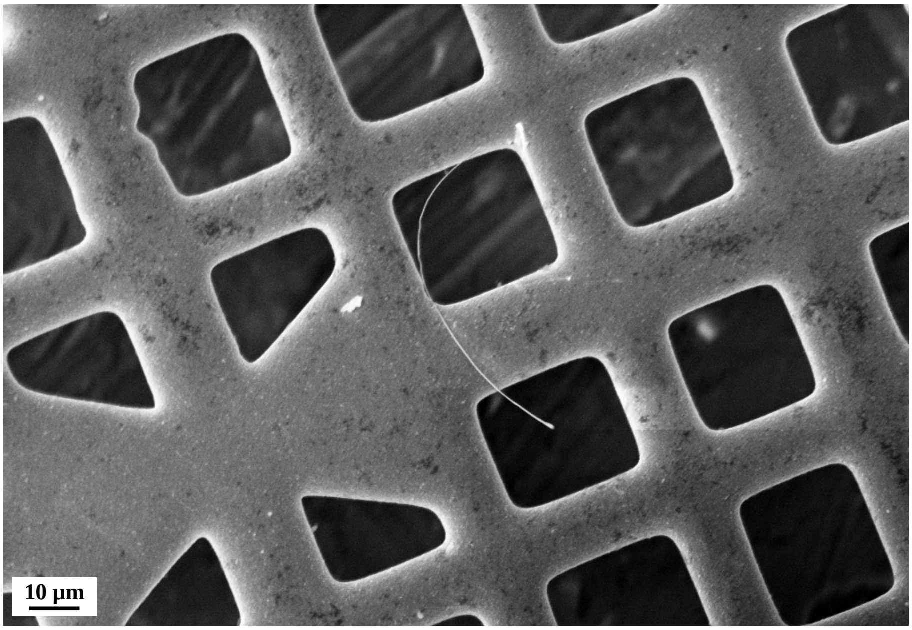

Figure 7.2: Tungsten wire with a length of approx. 120 µm placed on a copper TEM grid substrate using two Kleindiek nanomanipulators.

In order to overcome this problem, a second attempt was launched using the Kleindiek manipulators in combination with the FIB and GIS systems. Wires were taken from a filter paper substrate using a Picoprobe needle mounted to a Kleindiek manipulator. Since the Zeiss / Leo 1540 XB is only equipped with one Kleindiek manipulator, the wires had to be “glued” to the needle by depositing platinum. Next, the needle was lifted up and the substrate replaced with a copper TEM grid. After placing the wire on the TEM grid, it was “glued” to this new substrate by depositing platinum. Then the wire was cut away from the needle using the ion beam. The adjacent end of the wire was “glued” to the substrate by depositing more platinum (fig. 7.3 **A**). Finally, the GIS nozzle was retracted and the ion beam was used to thin the sample (fig. 7.3 **B**).

After mounting the tungsten nanowire to the copper TEM grid, the sample was transferred to the transmission electron microscope. Figure 7.4 shows an overview of the wire section under investigation. The image was assembled from multiple TEM images. At first glance, it is clear that the wire has a phase boundary along the middle - a white strip along the entire sample.

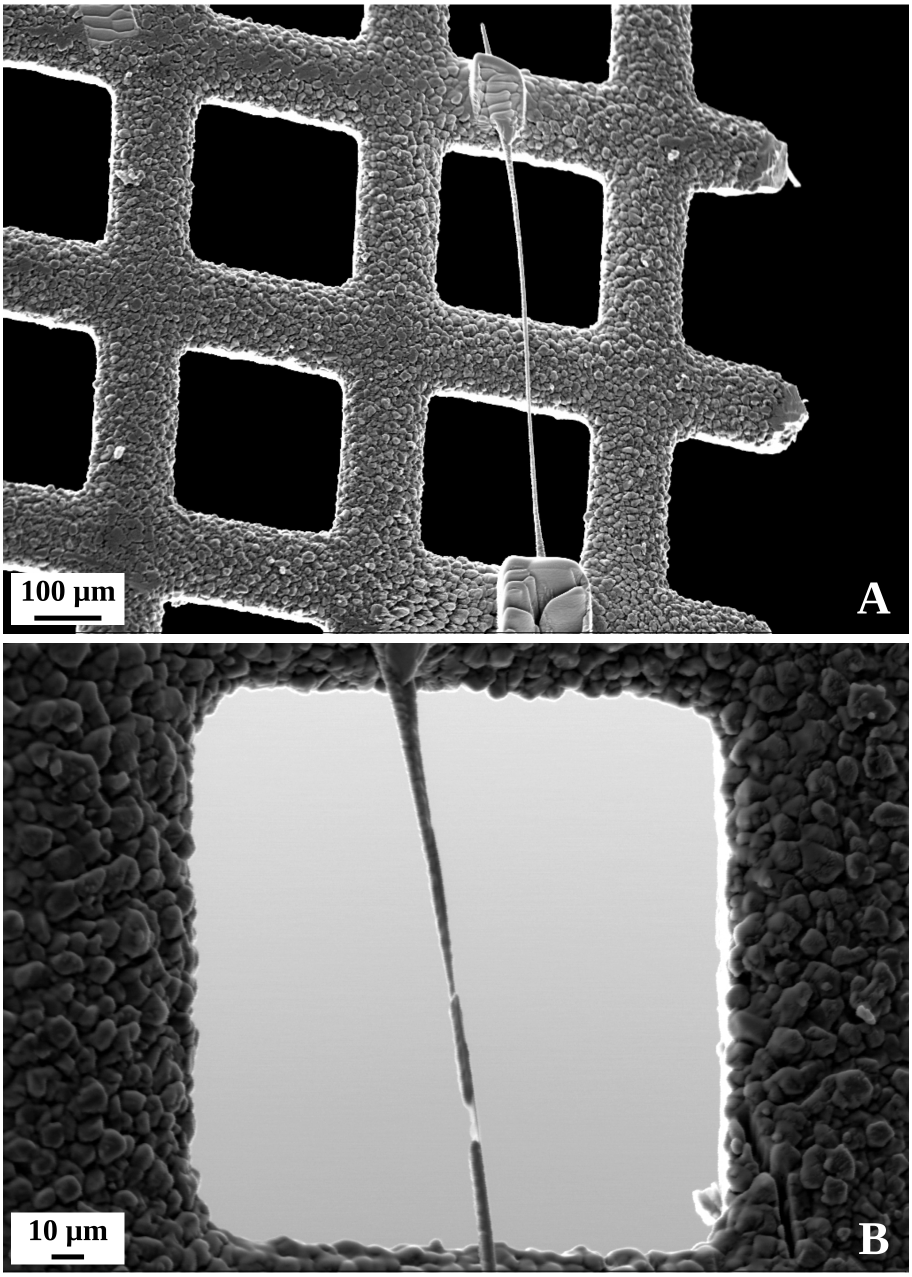

Figure 7.3: Tungsten wire placed on a copper TEM grid substrate using a Kleindiek nanomanipulator. **A**: The wire was fixed in place by depositing platinum "pads". **B**: Milling the wire with the FIB yielded thinned sections of the wire.

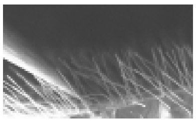

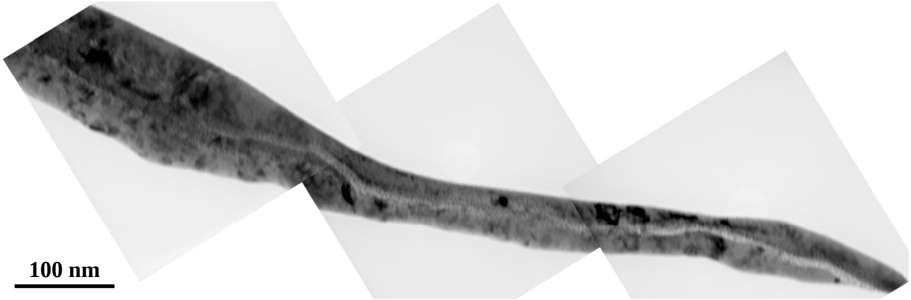

Figure 7.4: Multiple TEM images stitched together showing a small section of the investigated tungsten nanowire.

A close-up view of the wire is shown in fig. 7.5. Again, the phase boundary between the upper and lower part of the sample is clearly visible. Energy dispersive X-ray (EDX) measurements were performed in order to ascertain the nature of both phases. The results of the EDX measurements are shown in fig. 7.6. From these results it is very clear that the upper part of the sample in figures 7.5 and 7.6 is tungsten, while the lower part consists of a mixture of copper, carbon, gallium, and platinum. The latter three elements can all be attributed to the focused ion beam treatment: Gallium ions are used to mill the samples and to decompose the carbon-containing precursor materials for depositing platinum. While thinning the wire, the ion beam was pointed at the copper substrate. Therefore, it is very likely that milled copper redeposited on the sample.

The crystallinity of the sample was determined using selected area diffraction (SAD). The selected area is shown in fig. 7.5 (“spot” size 300 nm). Therefore, the result shown in fig. 7.7 **C** reflects both phases: The single crystalline tungsten yields a diffraction pattern consisting of an array of bright dots, while the deposited phase is polycrystalline and yields ring-shaped diffraction patterns.

In order to determine the crystallographic orientation of the wire, convergent beam electron diffraction (CBED) was applied. This technique utilizes a much smaller spot than SAD. The spot size in these experiments was 70 nm. CBED measurements were performed at four separate places along a 20 µm section of the tungsten wire under investigation. All recorded diffraction patterns indicate that the wire has an orientation close to <001> along the wire’s growth direction.

It should be mentioned here that applying electron backscatter diffraction (EBSD) to polished cross-sections of directionally solidified samples is a more

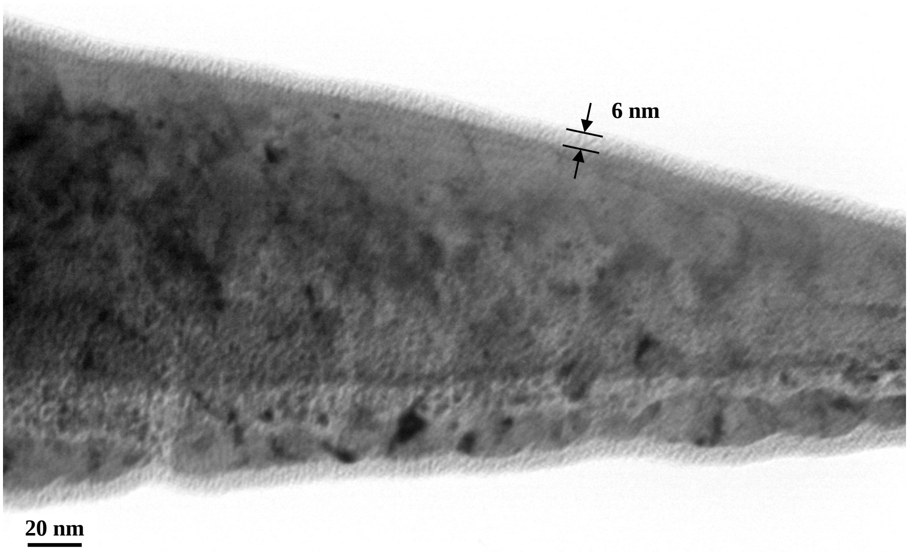

Figure 7.5: High resolution TEM image of the tungsten wire shown in fig. 7.4

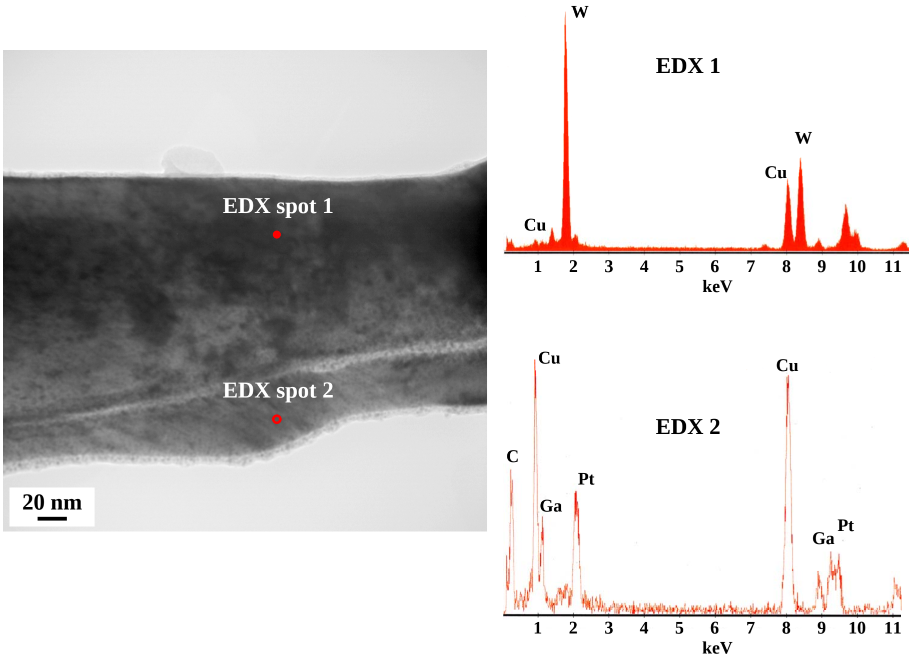

Figure 7.6: Another close-up view of the tungsten wire shown in fig. 7.4 with EDX spot measurements. The upper phase is tungsten with some copper deposits; the lower phase consists of deposits from FIB treatment.

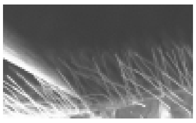

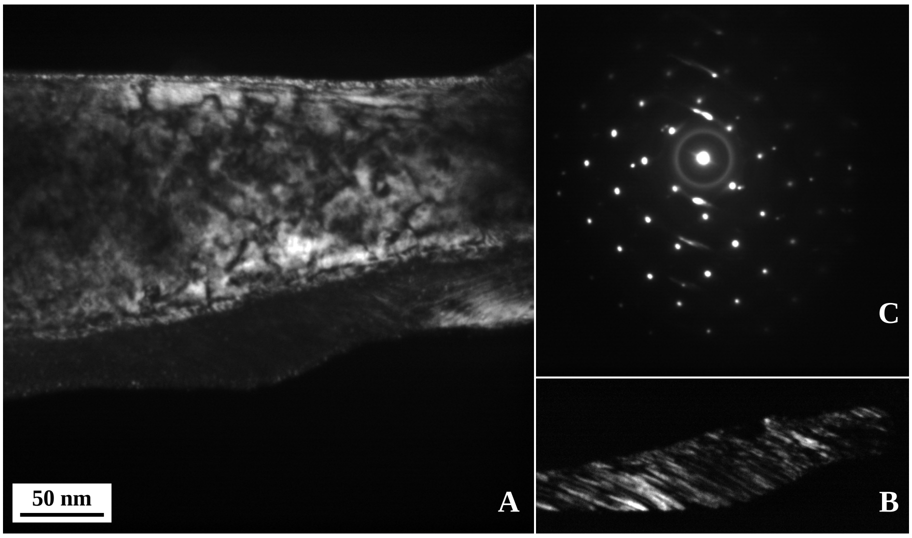

Figure 7.7: TEM investigation of the tungsten nanowire. **A**: DF image of the tungsten wire. **B**: DF image of the carbon, gallium, platinum deposits. **C**: SAD pattern showing two phases. Dots indicate a single crystalline tungsten phase and rings indicate a polycrystalline phase.

convenient way of determining the wires crystallographic orientation [165]. Of course, this is only possible prior to releasing the wires from the matrix.

The TEM results showed that the tungsten wire is a single crystal. The wire is probably covered by a very thin oxide layer, visible as the light-colored layer in fig. 7.5 (thickness approx. 6 nm), although no oxygen was found in the EDX spectra. This is not surprising, as the EDX typically probes a relatively large volume. The interaction of the electron beam with the material reaches depths of up to $2-3\,\mu m$. Due to the depth-dependent probing probability the bulk signal can be assumed to result from an interaction depth of $1\,\mu m$. The oxide thickness comprises only 0.6 % of that depth. When considering the stochiometry of the oxide (WO_3) and the fact that the heavier tungsten atoms will interact more strongly with the electron beam, 50 % of the signal might be attributed to oxygen. Consequently, the amount of detectable oxygen is approx. 0.3 % of the probed volume, while the detection limit of the EDX is above 1 %. Therefore, it is plausible that the amount of oxygen probed is too small to be detected EDX.

The EDX spectra show no nickel or aluminum from the matrix phase present in the wires. Again, the probed sample volume must be compared to the (expected) amount of material. Theoretical considerations based on the phase diagram of the system as well as chemical trace analyses show that the amount of matrix material in the wire phase is very small (s. section 5.2, p. 67). Thus, no traces of nickel or aluminum were found in the tungsten wires using EDX.

A more detailed investigation using Auger-spectroscopy should yield more precise results; unfortunately, this method was not available for this work.

7.1.3 Multi-Point Contacting of Single Nanowires

Similar to the procedure described in the previous section, wires were retrieved from a filter paper (fig. 7.8 **A**), placed on silicon wafers and "glued" into position (fig. 7.8 **B**). Platinum was deposited in two adjacent pads at the ends of each wire (fig. 7.8 **C**). In Addition, platinum strip were deposited perpendicular to the wire. The obtained structures are shown in figures 7.8 **D** and 7.9.

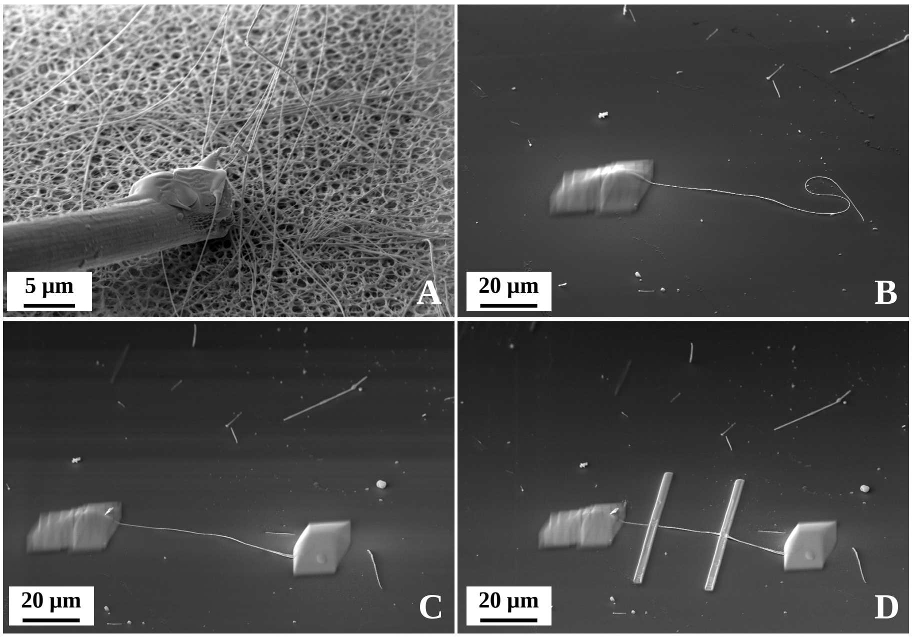

Figure 7.8: Tungsten wire placed on a silicon wafer using a Kleindiek nanomanipulator. **A**: Nanowire pick-up from filter paper. **B**: Nanowire on Si wafer; contacted on one side. **C**: Both sides contacted. **D**: Two additional strips deposited.

Next, the sample was transferred to the SÜSS microprober and four point resistance measurements were conducted. Probing the deposited platinum pads was achieved using commercially available probing needles with tip diameters of approx. 20 µm. The probes were connected to an IviumStat potentiostat and

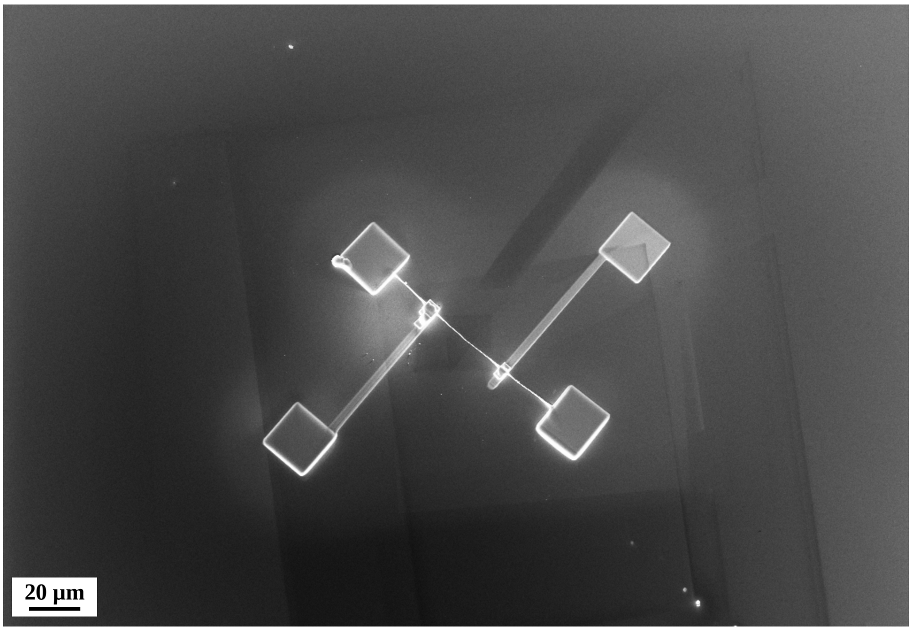

Figure 7.9: Tungsten nanowire with four platinum contact pads.

impedance measurements were performed in order to determine the sample's resistance (as shown in fig. 7.11). Prior to performing measurements on the wires, the resistance of the platinum structures themselves was determined by probing a deposited structure which consists only of platinum (fig. 7.10).

The acquired impedance spectra showed resistances of approx. $2 - 5\,\mathrm{k\Omega}$, depending on the pressure applied to the pads. The expected values for platinum structures of this size, calculated from the bulk resistivity of platinum ($10.6 \times 10^{-8}\Omega{\cdot}\mathrm{m}$, [120]) and the structure's dimensions, were in the range of $50\,\Omega$. Also, the expected values for the wire's resistance were calculated from the bulk resistivity of tungsten and the wire's dimensions, yielding values in the range of $100\,\Omega$.

The high resistance measured on the platinum structure can be understood in light of the TEM results discussed in section 7.1.2, especially the EDX results (fig. 7.6 on p. 89). The EDX spectra show that the deposited platinum is heavily contaminated with gallium originating from the FIB. Gallium is a semiconductor which forms various intermetallic phases with platinum over a wide range of compositions resulting in a complex phase diagram [166]. This alloying leads to a reduction in conductivity.

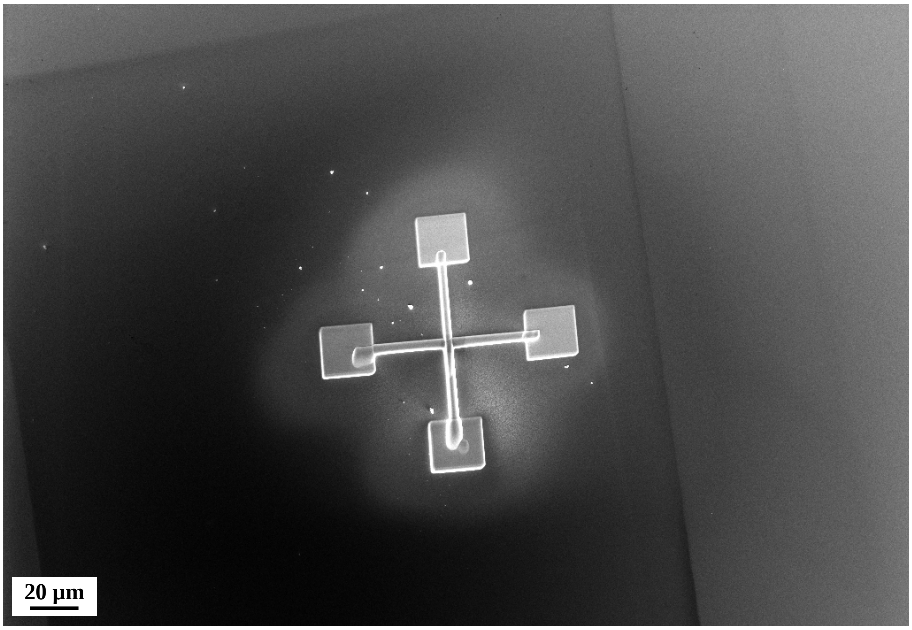

Figure 7.10: Platinum strips and pads without any wires for measuring the resistance of the deposited material

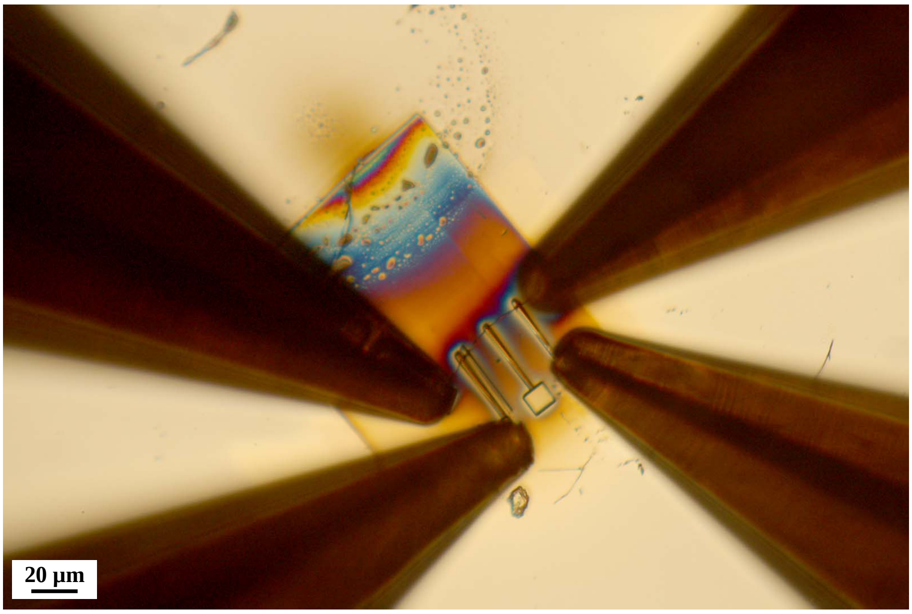

Figure 7.11: Probing the platinum pads with probe needles.

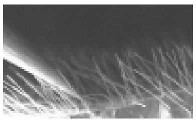

Thus, measuring the wires' resistance was not possible using this method. However, the experiments described here and in section 7.1.2 do show the possibilities in handling and mounting single wires.

7.1.4 Two-Point Resistance Measurements

Another attempt to measure the wires' resistivity was made by using a Kleindiek manipulator fitted with a microgripper, also fabricated by Kleindiek. The microgripper is constructed from two Picoprobes mounted in a casing and set in motion using another piezo. The gripper jaw itself is then shaped using a FIB and is approx. 4 µm in width and 1 µm in height. The gripper was used to retrieve a single wire from a filter paper. Subsequently, an attempt was made to insert the wire into a droplet of liquid gallium which was held in a copper holder. The droplet was approached using the nanomanipulator fitted with the microgripper holding the wire (fig. 7.12 **A**). Figures 7.12 **B** and **D** show a schematic representation of the ensuing situation and a frame grab from the digital video of the experiment, respectively. The wire did not pierce the liquid metal's surface due to the high surface tension of the metal droplet. Instead, the wire bended to a "U-shape" with a radius of approx. 15 µm without breaking. After retracting the manipulator, the wire made a full recovery from the bent position, showing full elastic behavior (figs. 7.12 **C** and **E**).

According to [167, p. 1092], gallium forms a surface oxide in air similar to valve metals such as aluminum. This caused the above-mentioned difficulties in piercing the droplet. Therefore, gallium was replaced by mercury. A final attempt at two-point resistance measurements was made using samples similar to the samples described in section 5.1.4. Stick shaped-samples were etched in hydrochloric acid under anodic polarization. This process was optimized to easily fabricate wire-tipped samples. These samples were subsequently dipped into liquid mercury droplets and two-point resistance measurements were performed. Since the nanowire at the tip of the sample was rigidly embedded in the matrix, it had a perfect low resistance contact. Dipping the wire into mercury created another low resistance contact. A galvanodynamic cycle from $-1\,\mathrm{mA}$ to $1\,\mathrm{mA}$ and back at a scan rate of $10\,\mathrm{mA{\cdot}s^{-1}}$ yielded the result shown in fig. 7.13. The resistance calculated from the slope of the graph is $90.5\,\Omega$ for a wire with a length of approx. 50 µm.

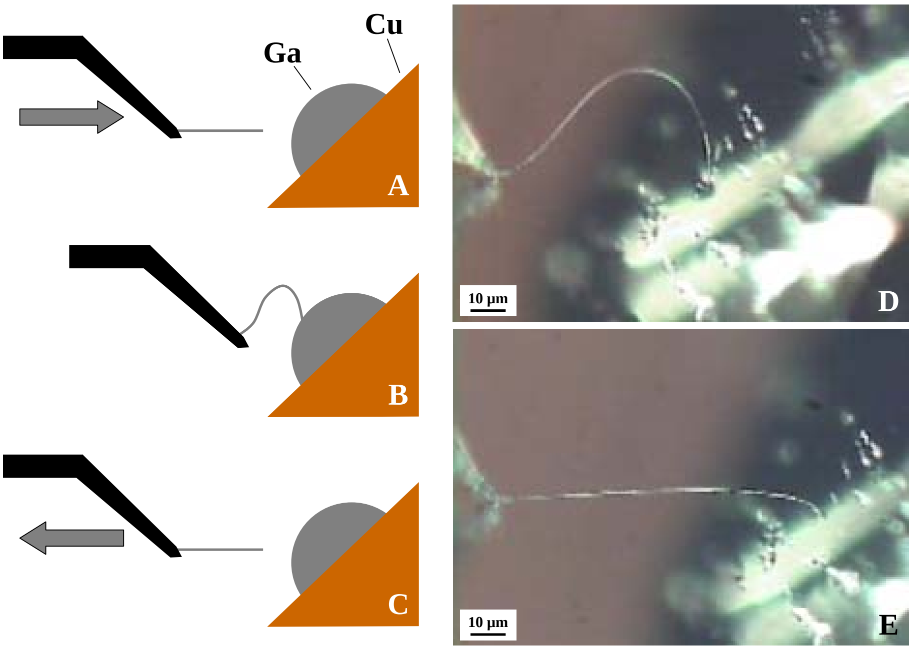

Figure 7.12: Attempted immersion of a W nanowire into liquid Ga; the wire is being held by the Kleindiek microgripper.

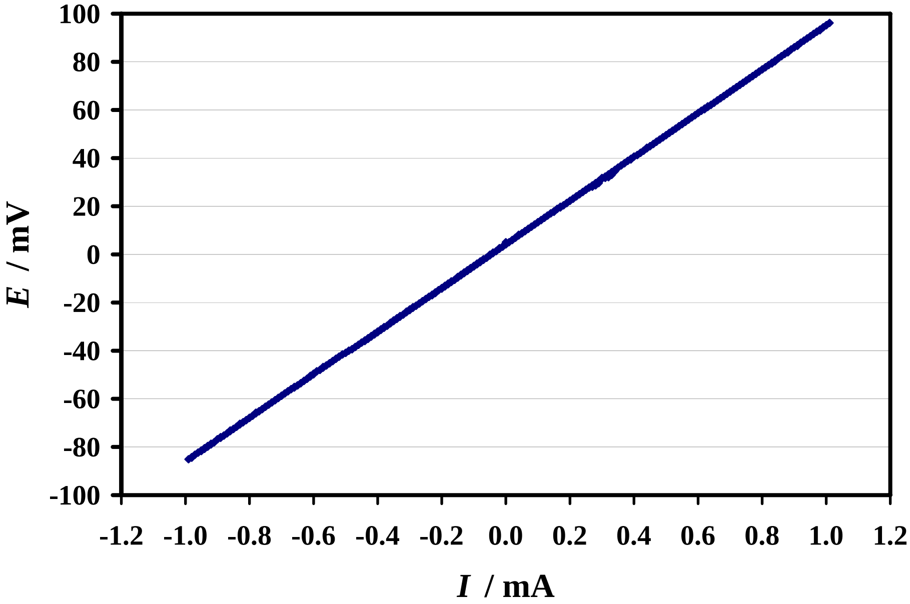

Figure 7.13: Galvanodynamic experiment for the determination of the W nanowire's resistance. The nanowire was partially embedded in the matrix and dipped into liquid Hg for contacting. The resistance of the wire is 90.5 Ω.

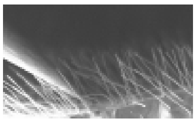

7.1.5 Initial Steps in Mechanical Bending Tests

After observing the extreme flexibility of the nanowires shown in fig. 7.12, further experiments were conducted to investigate the material properties. Fitting the scanning electron microscope with the Kleindiek manipulators made it possible to affect the wires while under close observation.

Using a "nanoforest" such as the samples described in section 5.1.1, initial experiments on the wires' mechanical properties were performed. After approaching a wire with the manipulator tip (fig. 7.14 **A**), the wire was bent (fig. 7.14 **B**) until the manipulator needle was touching the substrate (fig. 7.14 **C**). After retracting the manipulator, the wire made a full recovery showing purely elastic behavior (fig. 7.14 **D**).

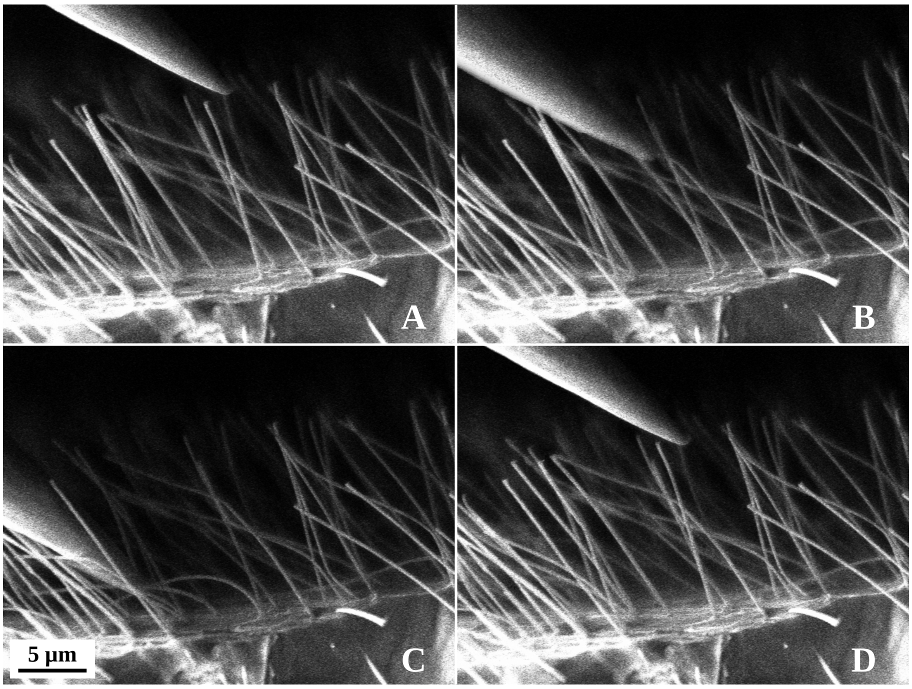

Figure 7.14: Initial investigation of the mechanical properties of tungsten nanowires. **A**: Approaching the nanowire. **B**: Contact and slight bending. **C**: Full deflection. **D**: The manipulator is retracted; the wire makes a full recovery.

Unfortunately, the manipulator was not equipped with force sensing capabilities. Therefore, it was not possible to extract any further information from the experiments performed.

Work done in cooperation with L. Phillipe from the ETH Thun, Switzerland on *ds*-NiAl-Re samples prepared at the Max-Planck-Institut für Eisenforschung using a similar set-up equipped with a force sensor has yielded interesting results concerning the yield stress of single crystal rhenium wires [168]. In these experiments, the mechanical properties of single crystal rhenium nanowires were measured and evaluated by applying finite element (FE) calculations. The yield stress of the single crystal nanowires was shown to be up to 100 times higher than that of the bulk material.

Other authors have also performed experiments on the yield stress and other mechanical properties of nanoscopic structures. In particular, results published by Nix, Feng, Hoffmann, and co-authors have contributed to understanding the mechanical properties at the nanoscale [34, 169–173]. One publication published by Uchic *et al.*, focusing on size-scale effects, deals with stress-strain curves measured on micro-sized nickel and nickel alloy structures [174]. The structures are produced by machining them from bulk materials using a focused ion beam (FIB). In this approach, the contamination with gallium, as discussed in section 7.1.3, may pose a problem as well as the enormous concentration of surface defects introduced to the surface through this treatment. Also, the directionally solidified material has a very distinct advantage in that directionally solidified samples are single crystals, as described in sections 3.2 and 3.3. The arrays of nanowires consist of crystallographically identical wires - each wire is an exact copy of all of its neighbors; each wire has the same crystallographic orientation as all of its neighbors - even azimuthically. This fact allows multiple non-reversible bending experiments to be performed on identical (virtually the “same”), single crystal wires. This is a unique situation; no other system can offer the possibility of repeatedly performing potentially destructive tests on the “same” sample.

7.1.6 Harvesting single nanowires

Using the Kleindiek manipulator in combination with the microgripper described above, (section 7.1.4) it is possible to harvest single nanowires. This is achieved by maneuvering the gripper into the close vicinity of a wire protruding from a selectively etched sample and gripping the base of the wire. The manipulator is then set to oscillate. This motion induces a fatigue breakage of the wire. The wire can then be extracted from the matrix and placed in the desired location on a different substrate. A SEM image of an extracted wire is shown in fig. 7.15.

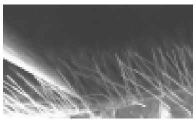

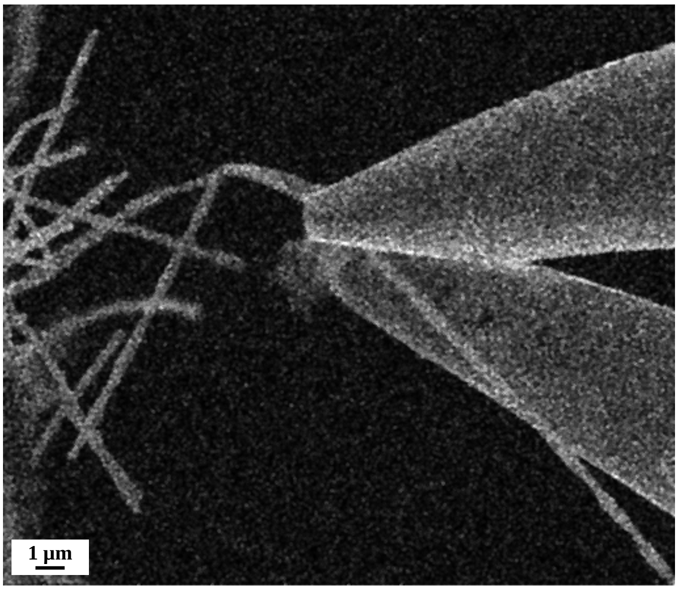

Figure 7.15: Kleindiek microgripper holding a W nanowire harvested from the matrix.

Transferring wires to other substrates (e.g. silicon wafers) can be achieved with much greater ease by simply pressing the substrate material against a filter paper loaded with wires (see fig. 5.17 and section 7.1.1, section 5.2, p. 66). In that case, the wire can only be chosen at random from the multitude of wires on the paper. Using the microgripper, it is possible to choose a specific wire directly from the matrix for further testing. This may be of interest, e.g., if a wire of a certain crystallographic orientation is desired or if it is necessary to position a wire with a certain orientation on a substrate. The wire's orientation can be determined by electron backscatter diffraction (EBSD) measurements prior to selective dissolution.

7.2 High Temperature Stability

The NiAl-X (where X is Mo, Re, or W) alloys under investigation are well-known for their high temperature resistance. In fact, this feature is what sparked a great deal of interest in eutectic materials in the 1960s: The fibrous structures obtained from directional solidification of eutectic alloys yielded materials that were stable at very high temperatures but with greatly improved mechanical properties compared to other high temperature alloys [82, 105, 116, 175, 176].

The previous investigations of the temperature stability all concentrated on the bulk properties of the materials.

In order to investigate the high temperature stability of the nanowires themselves, *ds*-NiAl-Mo, *ds*-NiAl-Re, and *ds*-NiAl-W samples were selectively etched according to the procedures described in section 5.1, exposing the molybdenum, rhenium, and tungsten wires, respectively. Next, the samples were microscopically labeled by using the focused ion beam (FIB) to cut markers into the sample surfaces. The samples were then enclosed in glass ampules with inert atmospheres of argon gas and exposed to a temperature of 1000 °C for periods of 1, 2, 4, and 8 days. Scanning electron microscope (SEM) images are shown in figures 7.16 through 7.19. In general, it can be seen that the wires themselves were hardly affected by the treatment, although the sample surfaces did oxidize substantially. The oxidation is due to residual oxygen left in the glass ampules. Further tests with higher quality inert atmospheres should yield more detailed results.

Figures 7.16 and 7.17 show the evolution of *ds*-NiAl-Mo from 1 day of exposure (fig. 7.16 **A** & **B**) and 2 days of exposure (fig. 7.16 **C** & **D**). While some oxide growth is evident in the lower images, the images show that the molybdenum wires withstood the temperature treatment well. This trend is continued in the images in fig. 7.17 depicting *ds*-NiAl-Mo samples exposed to 1000 °C for 4 (fig. 7.17 **A** & **B**) and 8 (fig. 7.17 **C** & **D**) days.

The same high temperature treatment of *ds*-NiAl-Re and *ds*-NiAl-W samples yielded very similar results. Figure 7.18 shows a single rhenium wire before (fig. 7.18 **A**) and after (fig. 7.18 **B**) 1 day of heat treatment. Again, the wire diameter is unchanged and the wire is covered with a thin oxide layer. The *ds*-NiAl-W (fig. 7.19) samples showed the highest amount of oxidation, although - as in all other cases - it was mainly the matrix that oxidized, not the wires.

The stability of the wires themselves should be very high at a temperature of 1000 °C. The melting temperatures for molybdenum, rhenium, and tungsten are 2623 °C, 3186 °C, and 3422 °C, respectively [120]. These values are much higher than the temperature the samples were exposed to in these experiments.

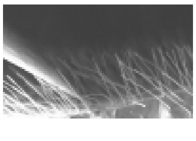

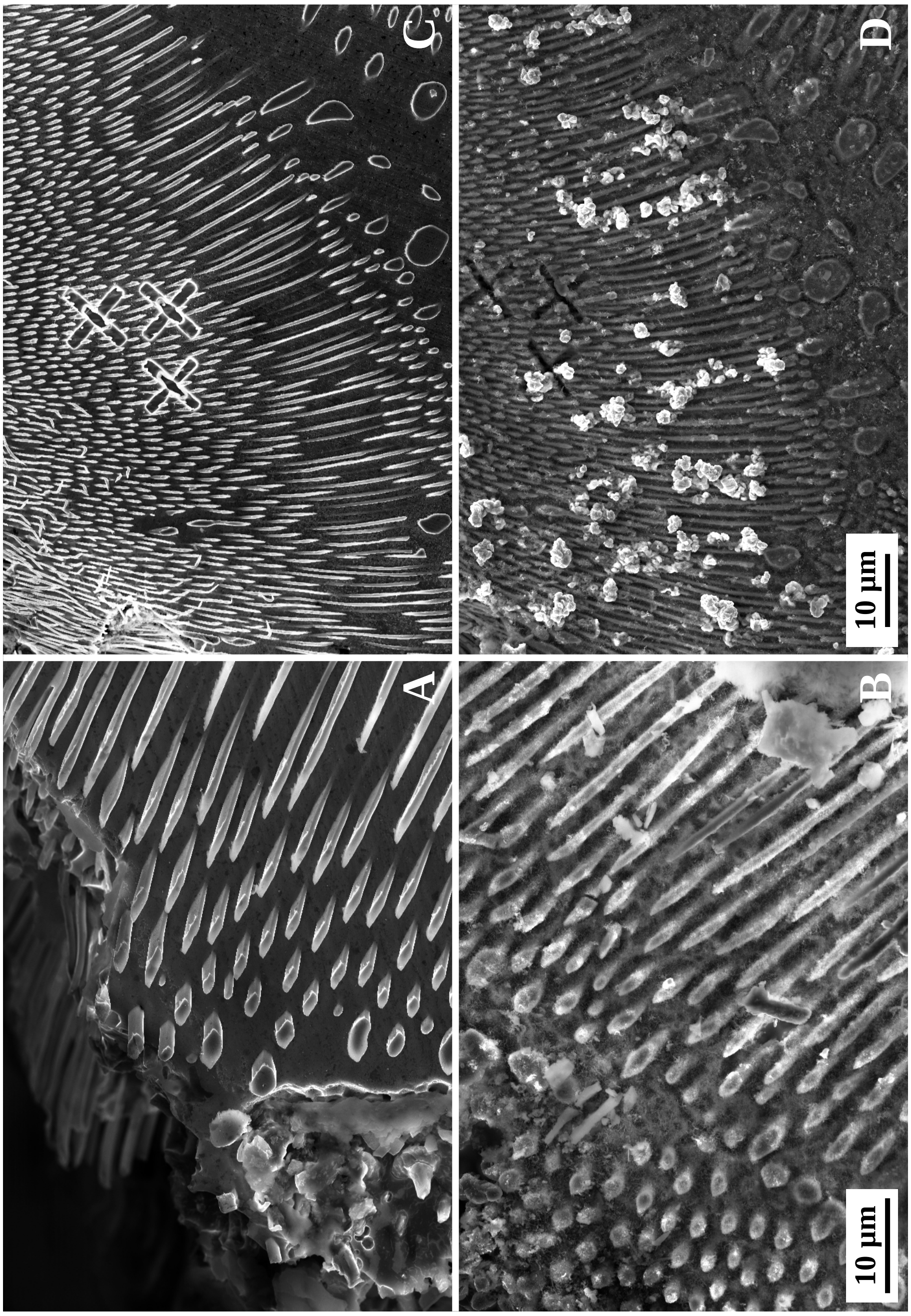

Figure 7.16: SEM images of a *ds*-NiAl-Mo sample before and after being heat treated at 1000 °C. **A** and **B**: Before and after being heat treated for 1 day. **C** and **D**: Before and after being heat treated for 2 days.

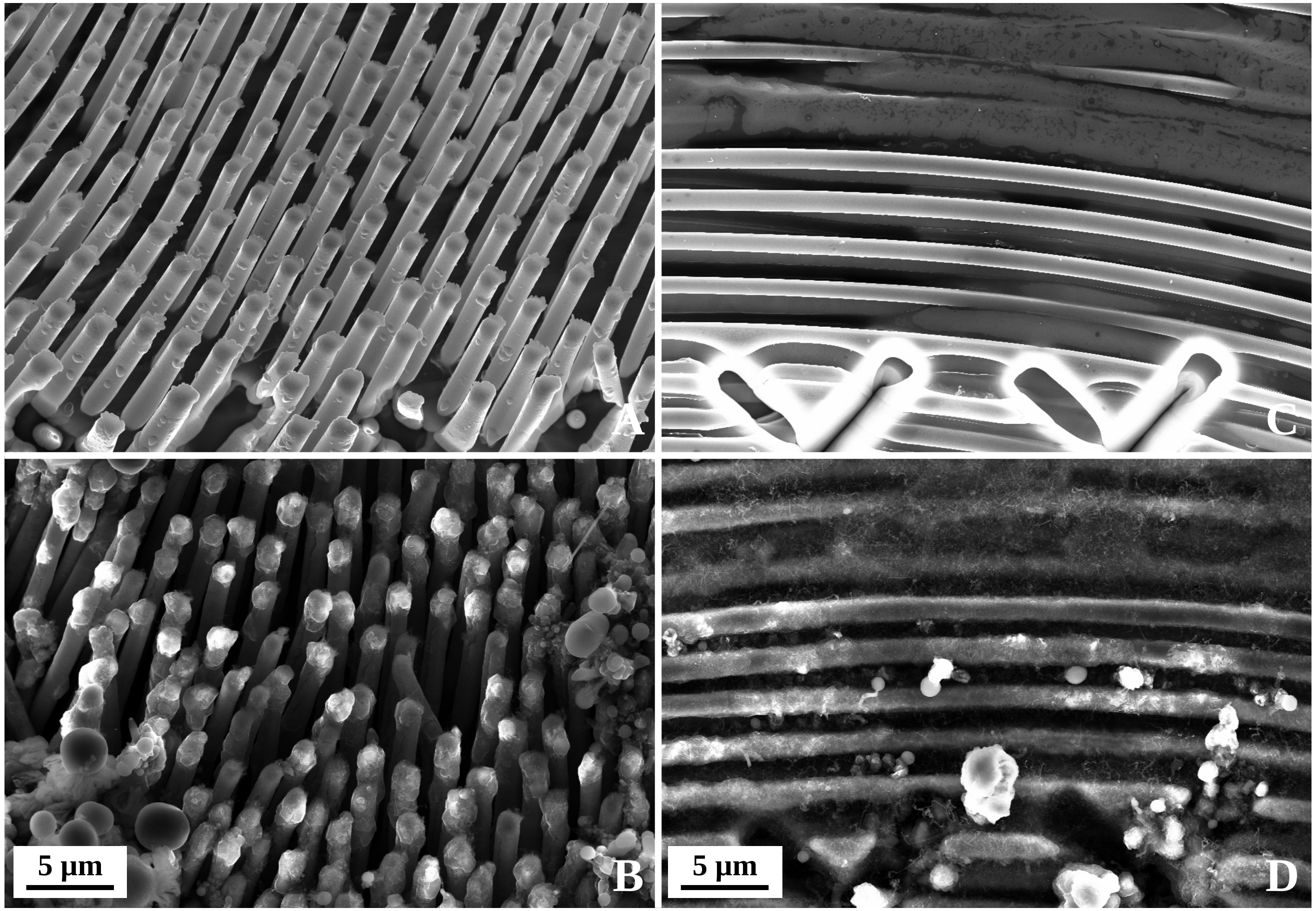

Figure 7.17: SEM images of a *ds*-NiAl-Mo sample before and after being heat treated at 1000 °C. **A** and **B**: Before and after being heat treated for 4 days. **C** and **D**: Before and after being heat treated for 8 days.

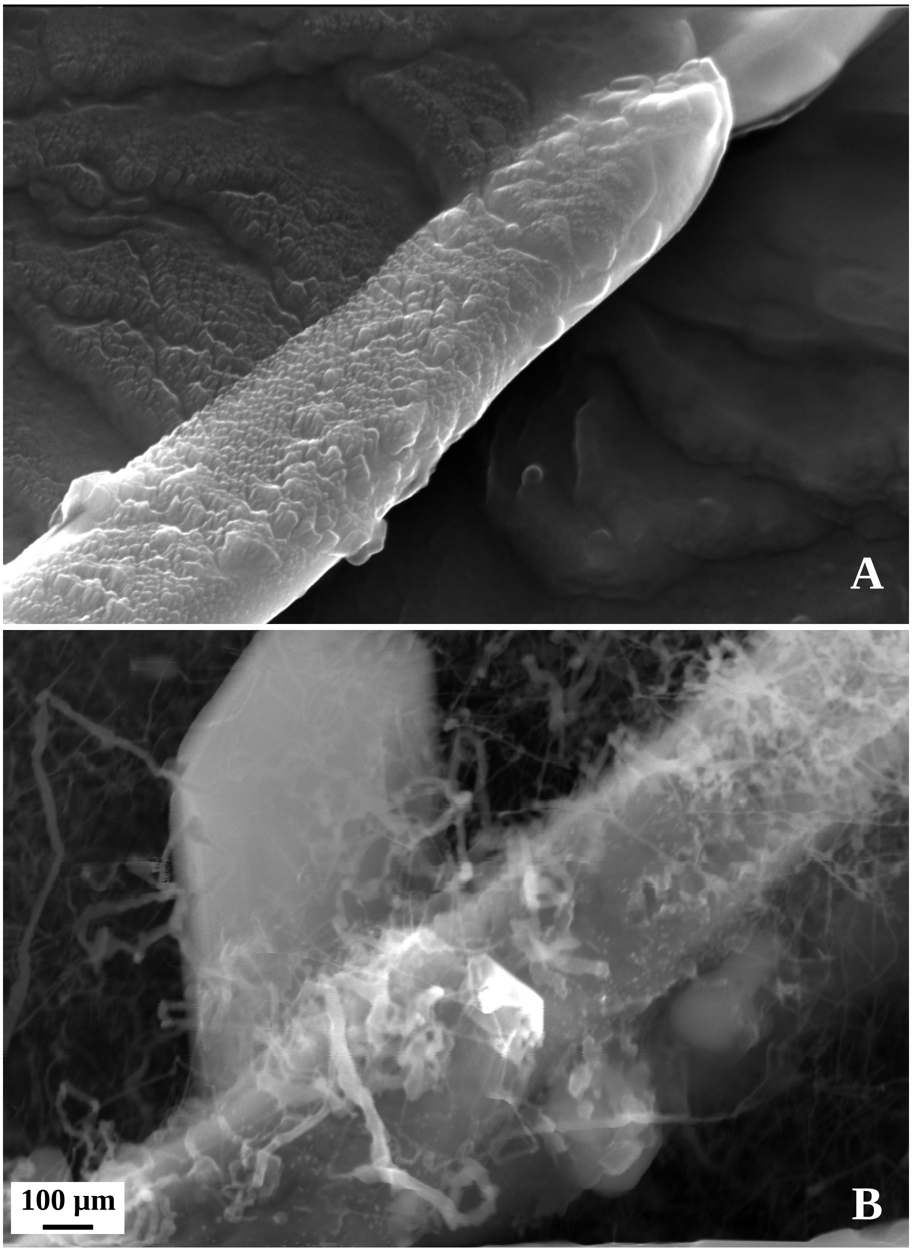

Figure 7.18: SEM images of a *ds*-NiAl-Re sample before (**A**) and after (**B**) being heat treated at 1000 °C for 1 day

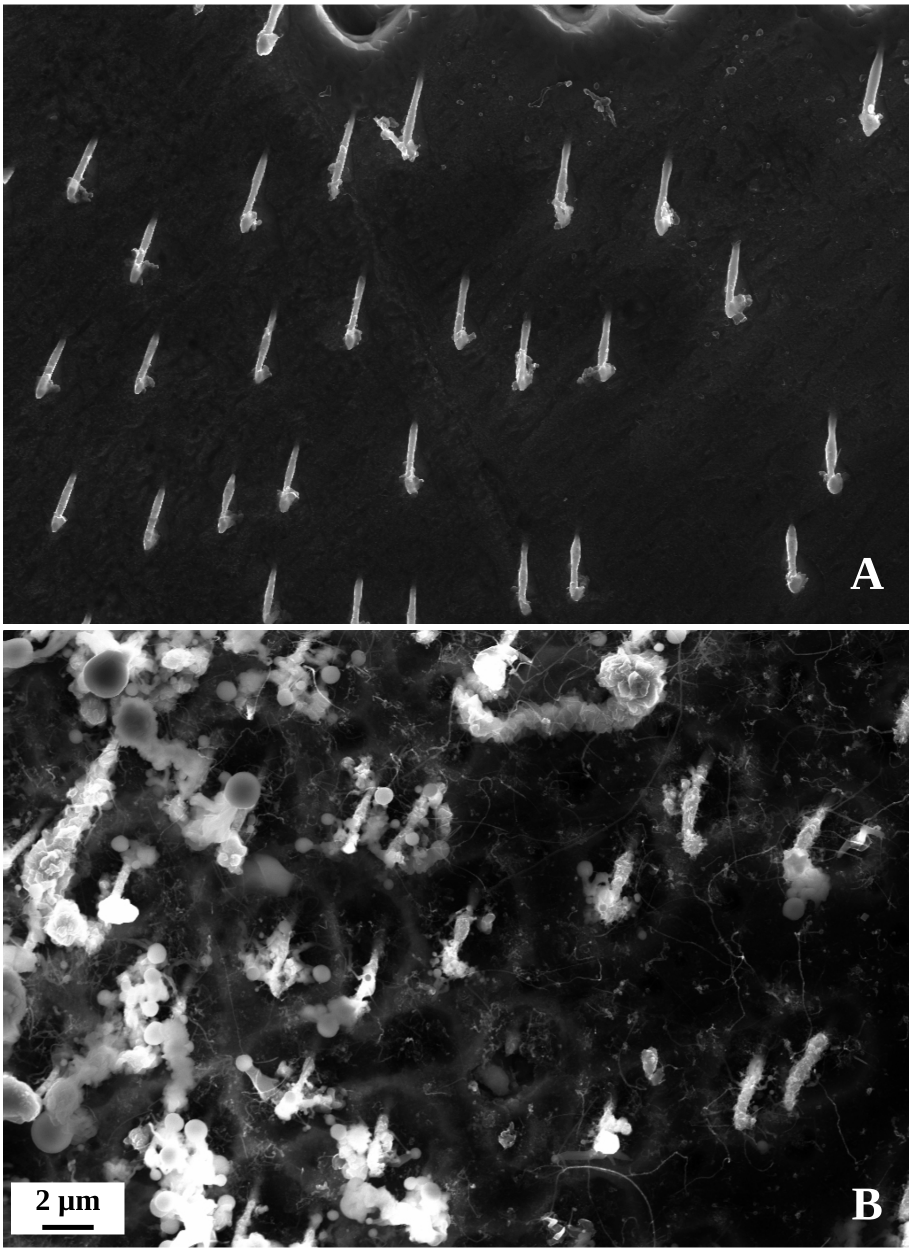

Figure 7.19: SEM images of a *ds*-NiAl-W sample before (**A**) and after (**B**) being heat treated at 1000 °C for 2 days

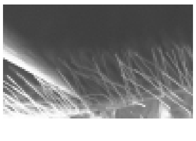

An important issue for applying nanoscopic structures at high temperatures is the formation of Rayleigh instabilities. This effect causes fluctuations in the thickness of wires at high temperatures due to the effects of surface tension [177–179]. Instabilities can start forming at temperatures of approx. two thirds of the melting temperature.

Due to the high melting points of the employed materials (which are among the thirty highest of known materials), they are well-suited for applications at elevated temperatures [180]. The single crystal nanoscopic wires have great potential for being utilized as sensor arrays, e.g. for combustion chambers.

7.3 Using Tungsten NanoWires for pH Measurement

It has been known for quite some time that oxide-covered tungsten probes can be used for measuring pH values. First experiments using tungsten wires inside light bulbs were reported as early as 1923 [181]. The light bulbs were transformed into electrochemical cells by fitting them with two holes - one for the electrolyte supply and one for the reference electrode. The whole bulb was then flooded with the test solution and the open circuit potential (OCP) was registered.

Fabrication of small tungsten electrodes for detecting H^+ concentrations was realized by Caldwell in the 1950s [182]. These electrodes were applied to measuring the pH values in large cells of crab muscles [183].

Investigations into the structure and properties of tungsten oxides were performed by Reichman and Bard [184]. A detailed report on the behavior of tungsten and tungsten oxides in alkaline media was published by Ortiz and coworkers, describing the formation of a so-called hydrogen and tungsten “bronze” [185, 186]. This oxide structure is pH sensitive due to the following reversible, proton-dependent redox reaction [187]:

$$\mathrm{WO_3 + nH^+ + ne^-} \rightleftharpoons \mathrm{H_nWO_3}$$

The electrodes used by Caldwell in the mid 1950s had diameters of approx. 100 µm and caused fatal damage to the tissue under investigation. Therefore, more recent approaches to producing ultra-small pH electrodes for *in situ* measurements involved making these electrodes smaller [188]. In this approach by Yamamoto *et al.*, thin tungsten wires were embedded in thin glass capillaries. The wires' cross-sections exposed at the tip of the capillaries were then electrochemically modified to obtain a well-defined oxide layer.

This electrochemical procedure was applied to single tungsten nanowires. Tip structures such as those described in section 5.1.4 were dipped into an electrolyte and processed according to the procedure described in [188]. One problem encountered was that the surface tension of the electrolytes caused the liquid to creep up along the wire so that the NiAl matrix was also wetted; this led to unwanted side effects which influenced the OCP. In order to overcome this problem, the tips were immersed into liquid contained in a glass capillary. This way, the tendency for the liquid to creep along the sample was balanced by the capillary forces in the glass capillary. Electrochemical experiments were made possible by adding a µ-reference electrode (see section 4.3) as well as a platinum wire counter electrode to the capillary. The set-up is shown schematically in fig. 7.20. A micromanipulator was used for positioning the nanowire inside the capillary cell.

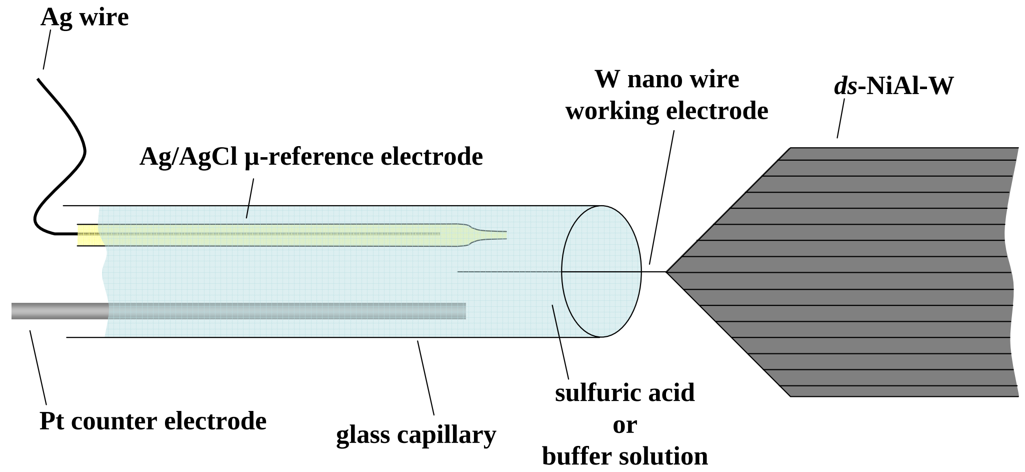

Figure 7.20: Capillary cell for electrochemical measurements on single nanowires.

The tungsten nanowire for pH measurements was prepared by cycling the wire in 2.0 M H_2SO_4 in a potential range of 1.2 V SHE to 2.2 V SHE twenty times at a scan rate of $20\,\mathrm{mV{\cdot}s^{-1}}$. Subsequently, the capillary was rinsed and filled with buffers of varying pH values. The buffers were prepared according to [189] by mixing the appropriate amounts of 0.2 M Na_2HPO_4 and 0.1 M citric acid, yielding solutions with pH values of 4.0 , 5.0 , and 6.0 .

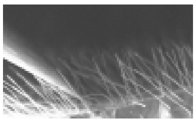

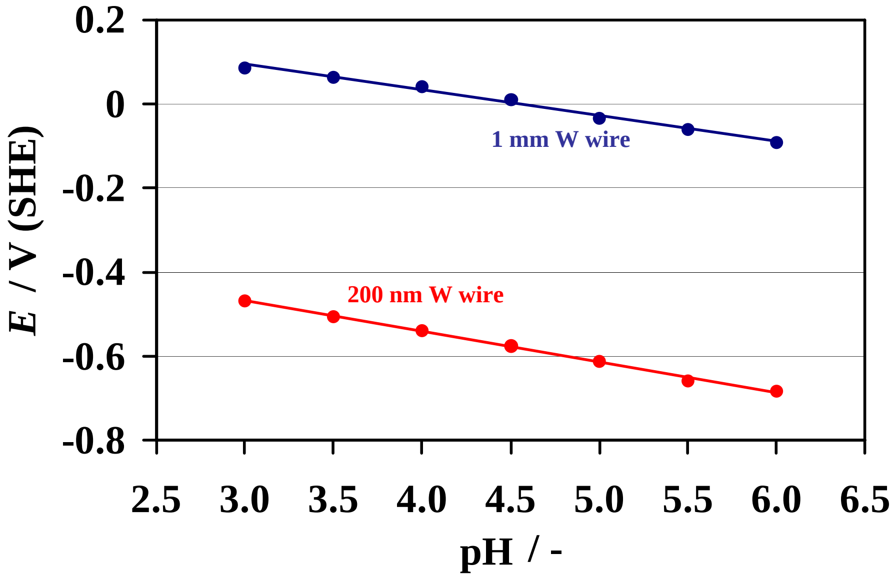

Figure 7.21: Potential of tungsten macroscopic (blue) and nanoscopic (red) wire electrodes at different pH values

Figure 7.21 shows the open circuit potentials at different pH values measured using the tungsten nanowire (red line). For comparison, identical measurements were performed using a macroscopic tungsten wire (blue line), which was pretreated the same way as the nanowire. Both samples show a strong dependency of the OCP on pH, suggesting the feasibility of employing tungsten nanowires as pH probes.

7.4 Polymer-Nanowire Composite Materials

Preliminary experiments on nanowire - polymer composites were performed using selectively etched *ds*-NiAl-W samples and a copolyimide.

This polymer was chosen because of its chemical and mechanical properties. The CF_3 groups increase the polymer's solubility in standard solvents, making it easy to process. Also, the polymer is extremely inert as well as stable at relatively high temperatures of up to 400 °C. A schematic of the underlying polymerization reaction is shown in fig. 7.22.

The monomers are also shown in fig. 7.22. The CF_3 groups of the 6FDA (4,4'-hexafluoroisopropylidene diphtalic anhydride) are responsible for the high solubility, and the DABA (3,5-diaminobenzoic acid) is added to yield a functional polymer. In this case, a copolyimide backbone with carboxylic acid groups - which are well-known as metal adhesion-promoting groups - is obtained [190, 191].

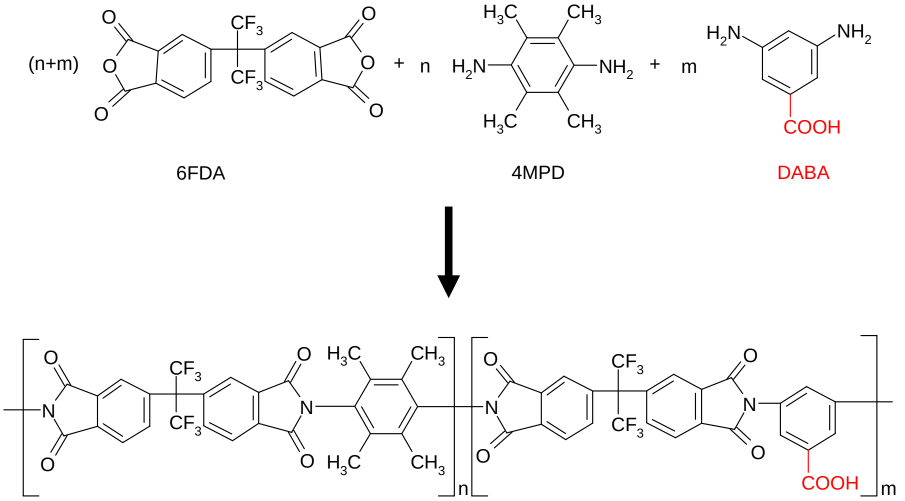

Figure 7.22: Copolyimide used for coating of W nanowires. The ratio of monomer units (n:m) in the polymer used was 4:1.

The polymer was dissolved in tetrahydrofuran (THF) and than applied to the surface of a sample with exposed wires using a pipette. Evaporation of the solvent led to the formation of a thin polymer film. The thickness of the films depended on the concentration of polymer in the solvent - typically 300 mg of polymer in 10 ml of THF - and the amount of solution applied to the sample surface (approx. 1 ml·cm^{-2}).

SEM images of selectively etched *ds*-NiAl-W samples coated with polymer are shown in fig. 7.23. Figure 7.23 **A** and **B** show long tungsten wires coated with polymer and protruding from the polymer layer. The images in fig. 7.23 **C** and **D** show cross-sections of the polymer-coated samples. The images illustrate that the wires are firmly embedded in the polymer and that there is a small gap between the metal surface and the polymer layer.

The images in fig. 7.24 show the result of lifting the polymer off of the metal surface. Some domains of the removed polymer film have embedded wires (fig. 7.24 **A**), whereas others show an “imprint” of the underlying nanowire array structure (fig. 7.24 **B**). As mentioned above, the polymer employed has excellent adhesion properties, yielding an ordered nanowire-polymer composite. On the other hand, the nanowires possess extreme flexibility - allowing them to withstand the lift-off process and leading to polymer films with nanosized channels.

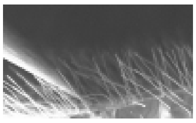

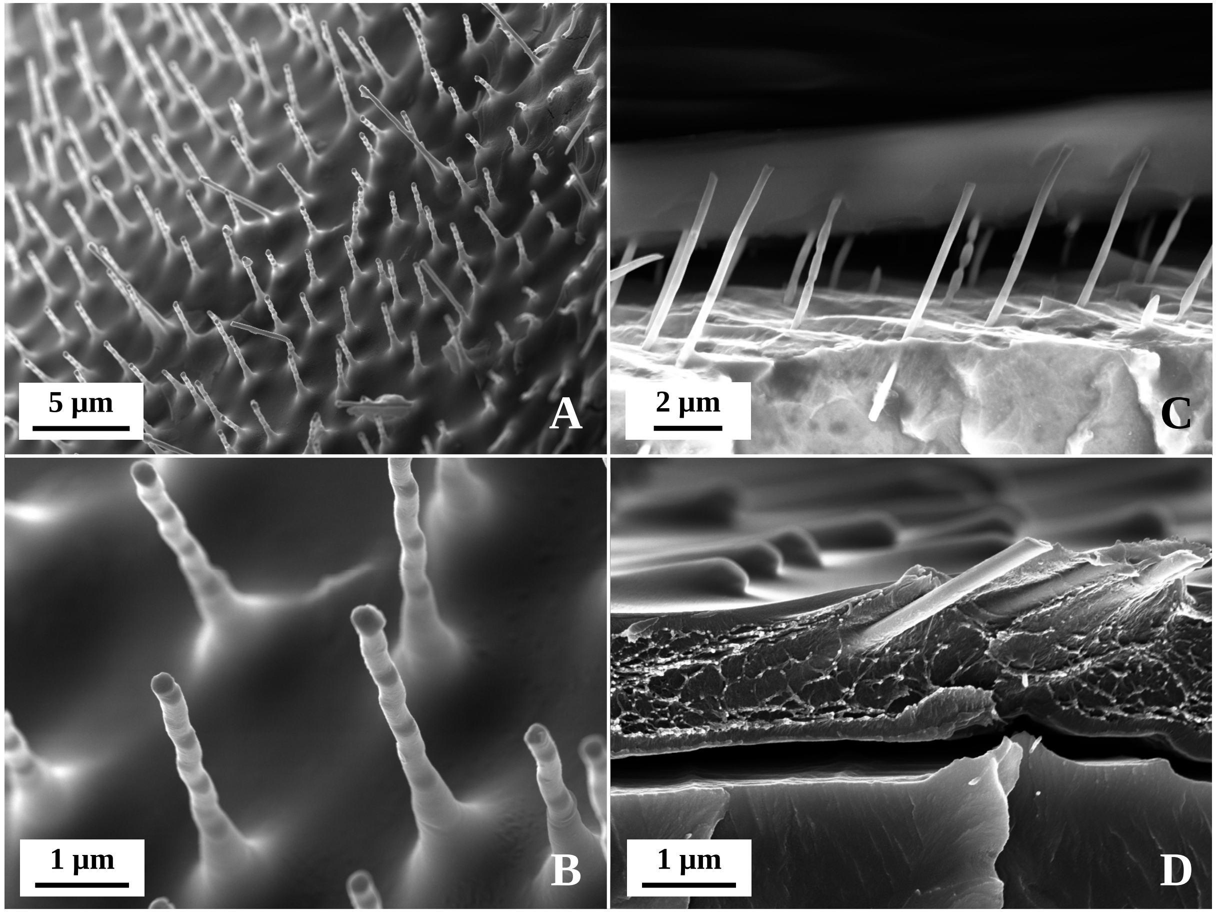

Figure 7.23: **A**: Tungsten nanowires covered by copolyimide. **B**: Close-up view of the coated nanowires. **C**: Cross-sectional view of a polymer coated sample; the polymer layer has a thickness of approx. 1 µm. **D**: Cross-section of fractured sample.

The chemical properties of the polymer can be tuned in order to adjust its adhesive qualities. This offers two possibilities: firstly, it is possible to produce polymer films with embedded wires. The thickness of the polymer film is easily controlled by varying the ratio of polymer to solvent and by utilizing different methods for producing films (spin coating, doctor blade, etc.). By changing the lengths of the exposed wires as well as the thickness of the polymer film, various types of composites with many different properties can be manufactured. The second possibility is the so-called PASTE process: **P**illar **AS**sisted **TE**mplating. An array of upright nanowires (pillars) is used as a template, which is coated with polymer. After the coating step, the polymer is removed leaving the wires intact on the substrate. The process yields polymer films with arrays of nanopores.

Another nanowire - polymer composite was fabricated by adding 25 mg of free nanowires (such as those shown in fig. 5.17 on p. 66) to 10 ml of the polymer - THF mixture described above. This mixture was then applied to a substrate using a pipette. Again, evaporation of the solvent led to the formation of a film. Figure 7.25 **A** shows the composite film deposited on a silicon wafer. The wires were randomly dispersed in the film. The wire density could easily be controlled by varying the number of wires added to the mixture prior to film formation.

The composite film was characterized by impedance measurements in order to determine the film's resistance. The composite was applied to a substrate made up of 12 copper strips. The lower portions of the strips were masked using adhesive tape. After applying the polymer, the tape was removed - exposing contact pads for electrical measurements. The sample is shown in fig. 7.25 **B**.

Resistance measurements were performed by probing the copper pads with micromanipulators fitted with the electrical probes also used in fig. 7.11 (p. 93).

Before measuring the resistance of the composite film, an identical sample was prepared which was coated with a polymer film without any wires. This sample was used to determine the resistance of the polymer itself. The resistance mea-

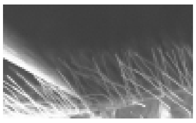

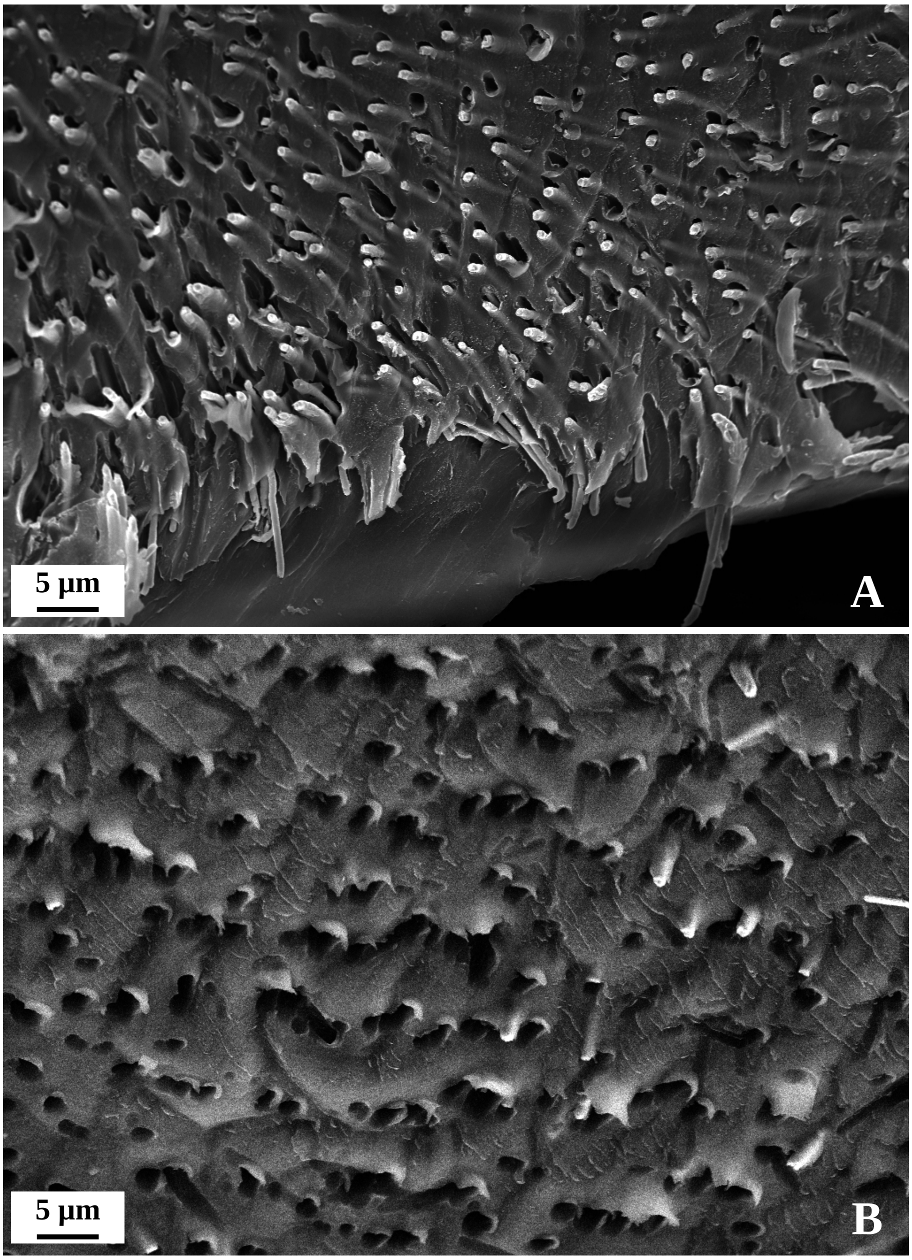

Figure 7.24: SEM images of copolyimide film peeled away from the nanowire array. **A**: Wires embedded in the polymer. **B**: Polymer without wires.

sured was $1.2 \times 10^9 \Omega$. Using this value, it was possible to estimate the polymer's resistivity (ρ_Ω), by taking the geometry of the sample into account:

$$\begin{aligned} \rho_\Omega &= \text{resistance} \cdot \frac{\text{cross-sectional area}}{\text{length}} \\ &= 1.20 \times 10^9 \Omega \cdot \frac{4.76 \times 10^{-4}\text{m}^2}{1.28 \times 10^{-3}\text{m}} \\ &= 4.47 \times 10^8 \Omega\cdot\text{m} \qquad \text{eq. (7.1)} \end{aligned}$$

The plotted results of the resistance measurements of the composite film are superimposed on the image of the sample in fig. 7.25 **B**. It is important to note that the colorations of the film in fig. 7.25 **B** are the result of the surface roughness of the film and do not give an indication of the density of wires in the film. As mentioned above, the wires were evenly dispersed in the film.

The resistance values obtained for the composite film are significantly lower than the value for the plain polymer, proving that the wires provide conductive paths through the polymer. For comparison, the resistance of a virtual nanowire, crossing the gap between two adjacent copper strips was calculated:

$$\begin{aligned} R_W &= \rho_{\Omega,W} \cdot \frac{\text{length}}{\text{cross-sectional area}} \\ &= 5.29 \times 10^{-8} \Omega\cdot\text{m} \cdot \frac{1.28 \times 10^{-3}\text{m}}{3.14 \times 10^{-14}\text{m}^2} \\ &= 2155\,\Omega \qquad \text{eq. (7.2)} \end{aligned}$$

This is well within the range of the values measured, indicating that in some cases a single "path" of wires reached from strip to strip, in other cases multiple "paths" connect two copper strips.

The employed substrates were taken from a blank circuit board, therefore the copper strips are normed to a specific socket. Using this socket, an electronic measuring device is imaginable, which could easily act as a read-out device for exchangeable "plug-in" sensors with different polymer coatings for various applications.

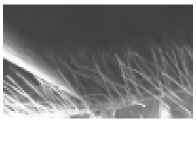

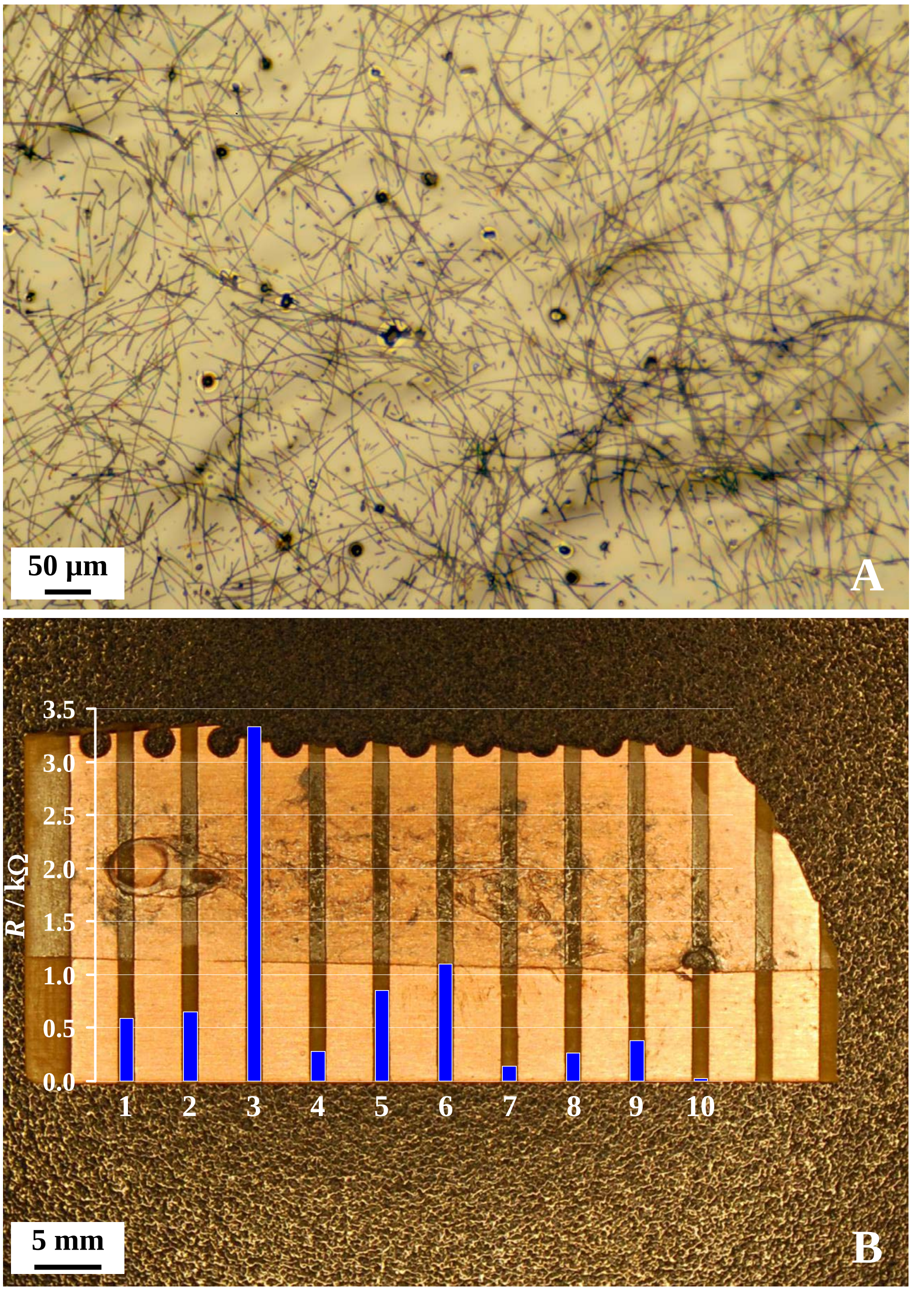

Figure 7.25: **A**: Tungsten nanowires dispersed in copolyimide film. **B**: Copper strips coated with nanowire - polymer composite. The measured resistance for each gap is superimposed on the image.

8 Summary & Future Applications

After presenting the investigated materials, the obtained sample morphologies, and initial results of characterizing the produced nanoscopic structures in the previous chapters, this chapter gives an overview of the results and discuss some of the possible future applications of these novel materials.

8.1 Electrochemical Processing

Next to the chemical etching of the matrix phase of the *ds*-NiAl-X materials using a mixture of hydrochloric acid and hydrogen peroxide, the electrochemical processing of the materials described in this work were discussed in chapter 5. Optimizing this process allowed the production of wire arrays with well definable wire lengths. The morphology of the wires as well as their spacing and diameter are determined prior to selective etching during the solidification process. But, electrochemical etching reveals the result of directional solidification and gives control over the exposed wire length.

Complete dissolution of the matrix phase yields free wires, which can be collected by simple filtration. The wires then reside on filter papers allowing further investigation or utilization for other experiments or applications. Upscaling this process allowed producing large amounts of nanowires; amounts so large that the nanoscopic wires conglomerate to macroscopic bundles.

Adjusting the employed chemical and electrochemical conditions allowed reversing the selectivity of the electrochemical etching process yielding arrays of nanopores. While the dissolution of the minor phase tends to stagnate due to the formation of an unfavorable chemical gradient in the pores, further optimization of the sample preparation and of the conditions for selectively etching the fibrous phase should yield metallic filters with nano-sized pores.

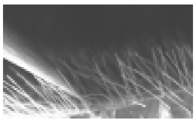

8.2 Manipulation

After preparation of wire arrays or free wires initial characterization is limited to imaging with light microscopy or scanning electron microscopy. Even though many different sample morphologies can be realized with the help of various mechanical, chemical, and electrochemical preparation steps, handling and manipulating individual wires is only possible with the help of more or less sophisticated mechanical and piezo-electric tools.

Harvesting Using piezo-driven nanomanipulators equipped with a microgripper it was possible to harvest individual wires. At the same time it was possible to place the wires on substrates for further experimentation and / or processing. A future project may entail placing wires on a silicon wafer substrate in well ordered patterns, e.g. for spectroscopy experiments.

Bending Handling free wires under the light microscope revealed their extreme flexibility. Bending wires to radii of 180° and more was easily achieved, after which the wires made a full recovery. The nanomanipulators were also used for testing the wires elastic properties in the SEM. In this case partially exposed wires still embedded in the matrix were bent. Again, the wires showed extreme flexibility. On the other hand, it was also possible to plastically deform the wires. Applying too much pressure caused the wires to fracture. Sadly, no quantitative results could be obtained, since the nanomanipulation system is not (yet) fitted with force sensing capabilities.

Further analysis of the wires' mechanical properties were performed in cooperation with groups from the Technische Universität Ilmenau and the Max-Planck-Institut für Festkörperforschung in Stuttgart [165]. Using a combination of e-beam lithography, chemical etching, and AFM as well as electromotive resonance measurements and other techniques, singly and doubly clamped wires were investigated. Results obtained include the wires' Young's modulus and other elastic properties.

FIB preparations The focused ion beam was another useful tool for handling, manipulating, and further investigating the nanowires; especially when used in combination with the nanomanipulators.

FIB processing was used to prepare samples for EBSD measurements. Processing is necessary prior to measurements due to the fact that the matrix phase and the wire phase have different hardnesses leading to microscopically rough surfaces after grinding and polishing. Therefore, the FIB was used to mill a nanoscopically flat surface on the sample. Subsequent EBSD mapping yielded information on the single crystallinity and crystallographic orientation of the matrix and of the wires (fig. 8.1).

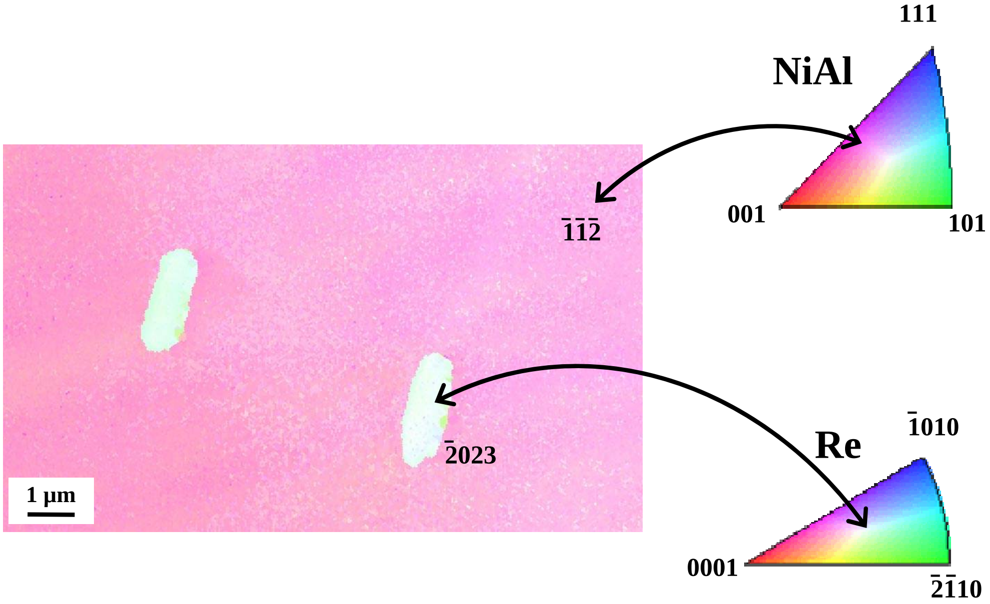

Figure 8.1: EBSD map of a *ds*-NiAl-Re sample. Each crystallographic orientation is represented by a color, coded into the inverse pole figures for each phase.

Another important application for the focused ion beam technology was handling, positioning, and modifying single nanowires. As described in detail in sections 7.1.2 and 7.1.3 FIB preparations allowed picking up individual wires and placing them on different substrates. In these experiments the ion beam was not used to remove material by milling, rather it was used to decompose a gaseous precursor facilitating the deposition of platinum at user defined locations.

This allowed preparing samples such as the ones used in [165], as well as structures intended for the measurement of a single nanowire's resistance. Finally, individual wires were mounted to copper TEM grids and thinned to allow electron transmission experiments.

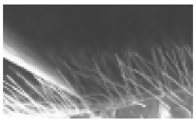

TEM characterization Using the above mentioned manipulation tools it was possible not only to mount a wire to a copper TEM grid, but to also mill away some of the tungsten in order to make the wire thinner. Due to the high density of tungsten transmission electron microscopy requires samples that have thicknesses under 100 nm. Thinning the samples using the ion beam after “gluing” them to the TEM grid allowed characterizing tungsten nanowires utilizing SAD, CBED, light field and dark field imaging, and EDX techniques.

It was found that the wire under investigation was indeed single crystalline and had a crystallographic orientation of <001> in the direction of growth.

The EDX measurements showed that the wires are not contaminated with nickel or aluminum from the matrix. Also, they revealed that the sample was coated with a thick layer made up of platinum, gallium, and copper. This layer is obviously a result of the preceding FIB preparation. This fact was also useful in understanding the problems in measuring the wire’s resistance through FIB-deposited platinum structures described in section 7.1.3 and below.

Finally, the TEM measurements showed that the wires are covered in a thin oxide layer of about 6 nm; again, a fact which must be taken into account when discussing measurements of the wires’ resistance.

Resistance measurements Determining the resistance of individual nanowires proved to be very difficult task. Several attempts in measuring the wires’ resistance were made.

The first attempt using the SÜSS microprober in combination with four micromanipulators fitted with Picoprobe tips was unsuccessful. The contact resistance between the tips and the wire was too high. Presumably the high contact resistance is a result of the small contact surface area as well as the oxide layer which naturally forms on the tungsten Picoprobe tips.

Another attempt was conducted using high precision nanomanipulators under SEM observation. Again, it was not possible to achieve a usable contact, presumably due to the oxide layers on the probes and the wires [192, 193].

The most promising sample preparation was described in section 7.1.3. Using the FIB technique platinum pads and contact leads were deposited on tungsten wires residing on a silicon wafer. The obtained structures are shown in figures 7.8

through 7.11. Sadly, the measurements were not successful; presumably due to the fact that the deposited material was heavily contaminated with gallium from the ion beam.

The tip shaped samples as shown in fig. 5.15 were also used for resistance measurements. These samples had single wires protruding from the tips which were rigidly embedded in the matrix and therefore had excellent contact on one end. Immersing these into a droplet of liquid mercury led to the formation of another excellent contact on the oppisite end of the wire. The measured resistance for a tungsten nanowire with a length of 50 µm and a diameter of 200 nm was 90 Ω.

Further measurements using tungsten nanowires supplied by the Max-Planck-Institut für Eisenforschung were performed by Andreas Rummel, an employee of Kleindiek Nanotechnik in Reutlingen. Using two micrograppers he was also able to measure the wires resistance yielding a value of 129 Ω for a wire with a length of 50 µm (fig. 8.2).

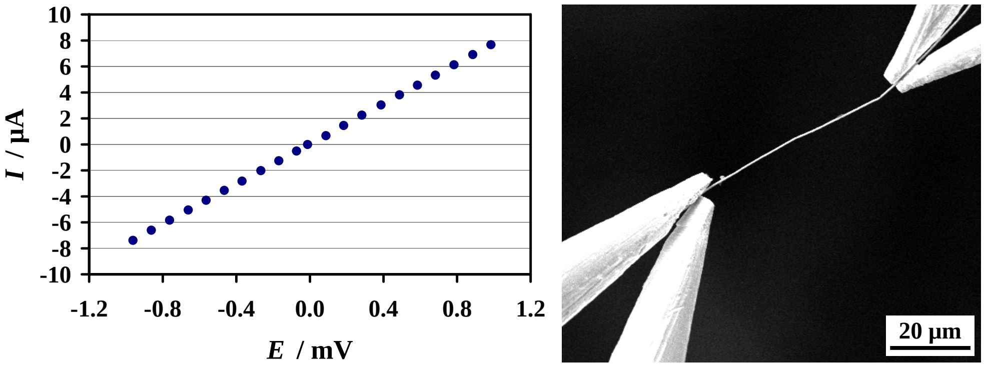

Figure 8.2: Characterization of a W nanowire using two microgrippers. Left: Evaluating the slope of the current vs. potential plot yields a resistance of 129 Ω. Right: SEM image showing two microgrippers holding a tungsten nanowire. (printed with permission from Kleindiek Nanotechnik GmbH)

Further measurements with wires of different lengths should yield more precise values as well as determining the influence of any residual contact resistance.

Electrochemical characterization In section 7.3, a µ-electrochemical cell was described which was used for preparing well defined oxides on single tungsten nanowires. This cell can also be applied to the full range of electrochemical methods. A multitude of electrochemical experiments can now be performed on single crystalline nanowires.

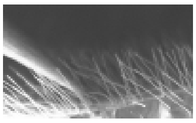

8.3 High Temperature Stability

Exposing wire arrays to high temperatures showed that the nanowires are stable at elevated temperatures, as was to be expected. High temperature applications including thermo emitters and sensors, e.g. for combustion processes, are potentially worthwhile topics for further investigation [194, 195]. It should be emphasized here that these systems potentially have the highest thermal stability of all available nanostructures as well as yielding iso-oriented single crystalline wire arrays, and will therefore give rise to the development of devices for various high temperature applications, such as sensing arrays or *in situ* micro or nanoprobing.

8.4 Future Applications

The following section lists a selection of potential applications for the materials described in the previous chapters.

STM tips The first application of a nanowire realized was the utilization of a single tungsten wire as a tip for a scanning tunneling microscope (STM) measurement. A scan of highly ordered pyrolytic graphite (HOPG) surface recorded with a sample such as the one described in section 5.1.4 is shown in fig. 8.3. The advantage of this type of nanowire sample over traditionally etched tungsten needles is the extreme aspect ratio of the wire. Probing the inside of deep cavities is feasible with a tip such as the one shown in fig. 5.15.

Sensor arrays For well over twenty years the positive effects of ever smaller electrodes and - more importantly - electrode arrays has been theorized and investigated [196–199]. In general, a significant improvement of the signal to noise ratio can be achieved, by using arrays of µ-electrodes. The enhancement in the signal to noise ratio was especially utilized in bio-sensing applications [200], such as detecting DNA and proteins [201], detecting low concentrations of glucose [202], detecting ultra low concentrations of pesticides [203], and extremely small concentrations of pathogens [204]. Another application studied by Cosofret *et al.* utilized polymeric, ion sensitive sensor arrays for cardiovascular monitoring [205].

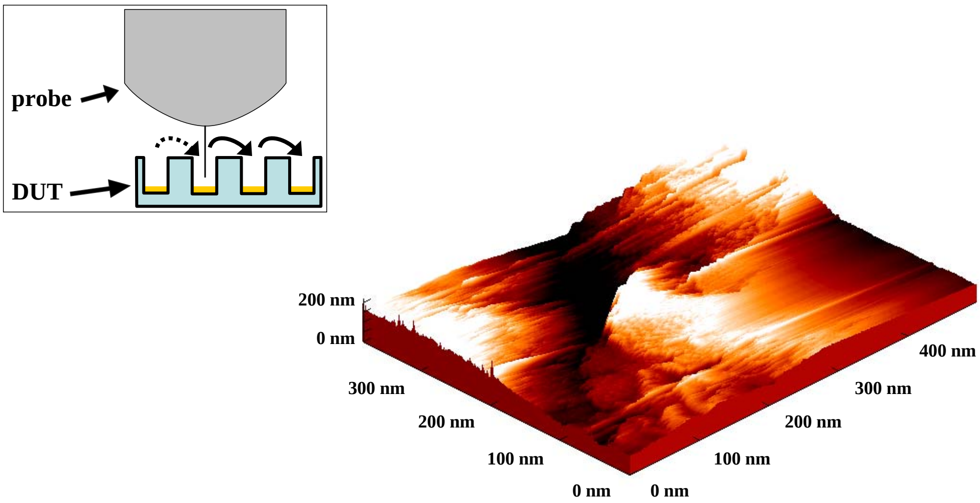

Figure 8.3: STM image of a HOPG sample using the tip shown in fig. 5.15 for imaging. The inset shows a schematic of the possible application of these high aspect ratio probes (DUT: device under test).

Combining the well studied effect of micro and nanoarrays as sensors with the knowledge of specific properties of certain metal oxides opens up new possibilities for applying the systems investigated in this work to constructing sensors [206–208]. Therefore, structures obtained from selectively etching directionally solidified materials are expected to yield substrates for fabricating sensor arrays for various applications, such as bio sensors or electrochemical sensing arrays as well as sensors for high temperature applications. Utilizing ordered arrays of chemically or electrochemically active nano-sized probes should greatly improve the sensibility of sensors for the above mentioned applications. Especially, the fact that the wires produced here are single crystalline is very advantageous to sensing applications.

In the case of the porous structures, sensors could be produced by first dissolving the fibrous phase and then depositing a noble metal such as gold or platinum into the obtained pores. Arrays of noble metal discs with nanoscopic diameters and controllable spacing could be produced in this manner.

Work on electrode arrays using the materials described here was performed by Bello Rodriguez and Hassel [162, 209]. The utilization of nanodisc arrays for electrochemical response measurements was achieved by submersing cross-sectionally cut and polished samples of *ds*-NiAl-Re and *ds*-NiAl-W in acetate buffer in order to passivate the matrix. In some cases the wire phase was simultaneously dissolved, yielding pores as described in section 6.1. Finally, gold

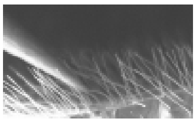

was electro-deposited selectively in the pores or on the active metal nanodiscs from a sulfite electro-plating bath. The experiments yielded arrays of gold discs of the diameter of the employed wires or - for longer processing times - slightly larger or much larger gold hemispheres, depending on the deposition conditions. Characterization of the obtained arrays was performed by cycling the arrays in potassium ferrocyanide solution at potentials around the transition potential of Fe^{2+} / Fe^{3+}. The idea in this approach is to utilize the features of nano-sized electrodes (with non-overlapping diffusion hemispheres) and achieve high signal to noise ratios by employing large numbers of nanoelectrodes.

Nanoscale pH probe Utilizing nanoscopic wires for probing ultra small cavities is an obvious potential application [210], e.g. the fabrication of a microelectrode system for monitoring enzyme activity in living plant cells [211]. As it is well known that certain oxides have pH-sensing capabilities, manufacturing nano-sized pH probes is very feasible [212, 213]. The results discussed in section 7.3 demonstrate that tungsten nanowires are useful pH probes. The experiments described here were aimed at characterizing the behavior of the nanoscopic tungsten wires. This was achieved by setting up a microcapillary cell. Since the determination of the pH requires measuring the variation of the nanowire's potential, a reference electrode system is required. In order to use the proposed system *in vivo* it is necessary to construct a probe which contains both the pH sensitive material and a reference electrode.

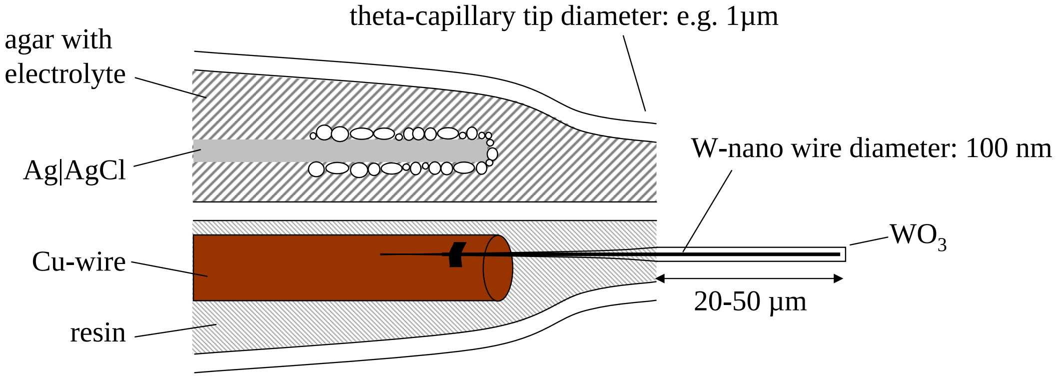

Figure 8.4: Possible assembly for a µ-pH-probe combining a µ-reference electrode system with a pH sensitive tungsten nanowire.

One possible design of such a probe is shown in fig. 8.4. In this set-up a single tungsten nanowire with a length of 100 to 200 µm is attached to a copper wire with a diameter of some µm using FIB deposition of platinum. A theta capillary is drawn in order to obtain a fine tip with a diameter of 1 µm or less. One chamber of the capillary is filled with a microreference system such as the Ag | AgCl | KCl system described in section 4.3. The copper wire with the attached tungsten nanowire is inserted into the other chamber and embedded in resin in such a fashion that the tungsten wire protrudes from the tip of the capillary. Finally, dipping the whole assembly in the appropriate electrolyte and polarizing the sample can facilitate tailored oxide formation yielding a microcapillary probe with a nano-sized tip.

Field emitter The emission of electrons from the surface of one solid phase to another phase caused by applying high electric fields is called Fowler-Nordheim tunneling or field emission. This quantum mechanical tunneling process is an important mechanism for thin barriers as those in metal-semiconductor junctions on highly-doped semiconductors. The high electric field narrows the potential barrier at the surface allowing electrons with energies below the Fermi level to tunnel through the barrier [214]. One of the primary uses of this phenomenon is the field emission microscope (FEM). Other devices utilizing the field emission effect are field emission triodes, amplifiers, microwave frequency devices, and light emitting devices [215–219].

Nanomaterials are good candidates for fabricating field emitters due to their favorable material properties [220, 221]. Using the materials obtained from directional solidification of eutectic alloys should yield field emitters with novel properties. Especially the tunable geometry of the nanostructures obtained from directional solidified eutectics should lead to advantageous properties: An array of standing nanowires with high aspect ratios and well defined spacing could lead to a local amplification of the field and therefore to an inhomogeneous field when applied to field emission. The beneficial effects could include a higher current efficiency as well as a decrease in the required voltage. The limiting factor at the moment is the work function of the oxide covered wires; chemically treating the wire arrays in order to remove the oxide may be a route to overcoming this problem.

Polymer composites Preliminary steps in manufacturing and characterizing nanowire - polymer composites were taken as described in section 7.4. A num-

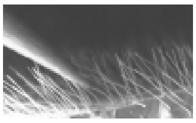

ber of interesting sample morphologies were obtained by applying a copolyimide polymer to selectively etched samples of *ds*-NiAl-W with exposed tungsten nanowires. Peeling the deposited films off of the *ds*-NiAl-W substrates resulted either in wires embedded on the polymer film (yielding ordered composite structures) or in polymer films with ordered arrays of nanosized holes (PASTE process). Tuning the surface chemistry of the wires as well as the chemical properties of the employed polymer will make it possible to choose which of the two results mentioned above will be obtained.

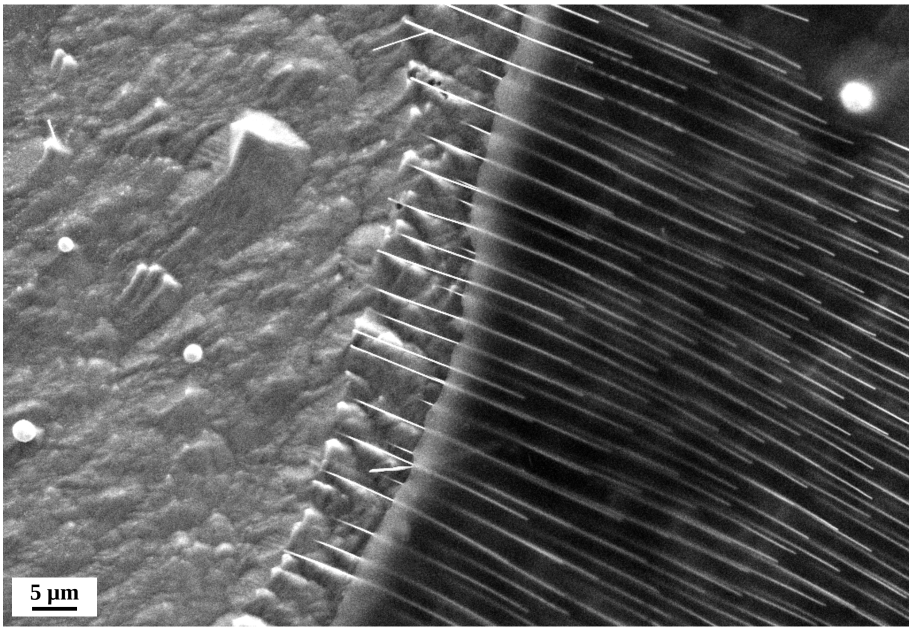

Figure 8.5: SEM image showing tungsten nanowires inside the copolyimd polymer film. The film does not charge, due the presence of the metallic wires.

The first indication of modified properties was given by the fact that the polymer composites were imaged in the SEM and showed virtually no charging effects, which are usually expected when imaging non-conducting materials (fig. 8.5). In order to investigate this further, a nanowire - polymer composite was fabricated by mixing free wires into the polymer-solvent mixture and subsequently applying the mixture to substrates yielding thin composite films. The films had thicknesses of approx. 30 µm. Impedance measurements were performed to determine the films resistance. It was found that the composites resistance is drastically reduced compared to the resistance of the plain polymer.

Finding the percolation threshold - the amount of wires necessary to facilitate the decrease in resistance of the film by statistically forming continuous pathways with direct metal contact - could open up the possibility of constructing sensing films: Adjusting the concentration of nanowires in the film to a value just below the percolation threshold, combined with a polymer sensitive to certain environments could be the basis of such a sensor. A change in the environment leading to a change in the properties of the polymer causing a reorientation of the wires in the film could lead to a sudden drop in resistance, yielding a measurable signal for a sensing application.

Additional physical properties, besides the resistivity, such as thermal conductivity, yield strength, and other mechanical properties should also be investigated. In the case of the copolyimide polymer the adhesion between the metal wires and the polymer itself is very strong resulting in excellent mechanical properties of the composite.

In general, novel materials for a wide range of applications are potentially available through the combination of the unique properties (e.g. the extreme flexibility) of the single crystalline nanowires with suitable polymers.

Other systems were also investigated within the framework of the project and in cooperation with Rainer Adelung from the Christian-Albrecht-Universität Kiel. Notably, coating arrays of rhenium nanowires with polytetrafluoroethylene (PTFE) yielded ultra hydrophobic surfaces. These surfaces reflect an impacting water jet as shown in fig. 8.6 [222]. A droplet of low viscosity polymer was applied to the surface and the wire - polymer interface was investigated with the SEM (fig. 8.6 **A**). The coated wires appear “reluctant” to come into contact with the droplet. Figure 8.6 **B** shows a water jet reflected off of the surface of a sample such as the one shown in fig. 8.6 **A**. It is interesting to note that the water impacts the surface, then travels along the surface, spreading out slightly, and is then ejected from the surface with nearly no loss in energy.

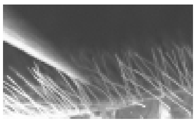

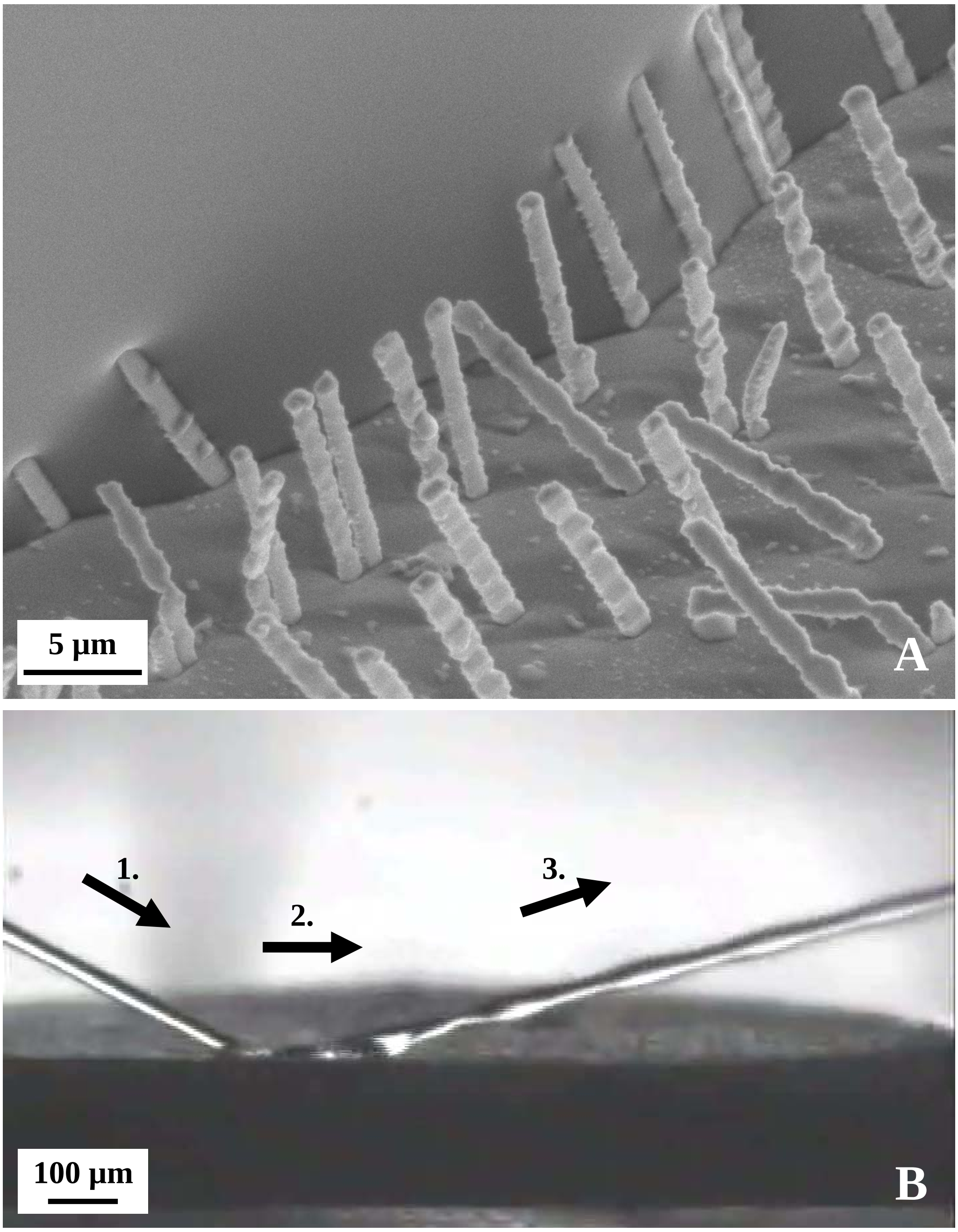

Figure 8.6: **A**: Array of rhenium nanowires coated with PTFE. A droplet of low viscosity epoxy was applied to the surface. **B**: Water jet reflected off of the surface. The arrows indicate the three phases of (1) impacting water jet, (2) water travelling along the sample surface, (3) ejected water jet.

Bibliography

[1] R. P. Feynman “There’s plenty of room at the bottom” *Engineering and Science* **XXIII** (1960).

[2] N. Taniguchi “Nanotechnology” *Journal of the Japan Society of Precision Engineering* **40** (1974) 287.

[3] G. Savard, S. Becker, G. Bollen, H. J. Kluge, R. B. Moore, T. Otto, L. Schweikhard, H. Stolzenberg, U. Wiess “A new cooling technique for heavy ions in a penning trap” *Physics Letters A* **158** (1991) 247.

[4] P. Groning “Nanotechnology: An approach to mimic natural architectures and concepts” *Advanced Engineering Materials* **7** (2005) 279.

[5] G. Granek, G. Hon “Searching for asses, finding a kingdom: The story of the invention of the scanning tunnelling microscope (STM)” *Annals of Science* **65** (2008) 101.

[6] D. M. Kolb, R. Ullmann, T. Will “Nanofabrication of small copper clusters on gold(111) electrodes by a scanning tunneling microscope” *Science* **275** (1997) 1097.

[7] D. A. Bonnell, R. Shao “Local behavior of complex materials: scanning probes and nano structure” *Current Opinion in Solid State & Materials Science* **7** (2003) 161.

[8] G. B. Khomutov, V. V. Kislov, M. N. Antipina, R. V. Gainutdinov, S. P. Gubin, A. Y. Obydenov, S. A. Pavlov, A. A. Rakhnyanskaya, A. N. Sergeev-Cherenkov, E. S. Soldatov, D. B. Suyatin, A. L. Tolstikhina, A. S. Trifonov, T. V. Yurova “Interfacial nanofabrication strategies in development of new functional nanomaterials and planar supramolecular nanostructures for nanoelectronics and nanotechnology” *Microelectronic Engineering* **69** (2003) 373.

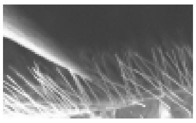

[9] G. B. Khomutov "Interfacially formed organized planar inorganic, polymeric and composite nanostructures" *Advances in Colloid and Interface Science* **111** (2004) 79.

[10] R. Garcia, R. V. Martinez, J. Martinez "Nano-chemistry and scanning probe nanolithographies" *Chemical Society Reviews* **35** (2006) 29.

[11] D. P. Yu, C. S. Lee, I. Bello, X. S. Sun, Y. H. Tang, G. W. Zhou, Z. G. Bai, Z. Zhang, S. Q. Feng "Synthesis of nano-scale silicon wires by excimer laser ablation at high temperature" *Solid State Communications* **105** (1998) 403.

[12] J. L. Liu, S. J. Cai, G. L. Jin, Y. S. Tang, K. L. Wang "Gas-source MBE growth of freestanding Si nano-wires on Au/Si substrate" *Superlattices and Microstructures* **25** (1999) 477.

[13] S. Botti, R. Ciardi, R. Larciprete, A. Goldoni, L. Gregoratti, B. Kaulich, M. Kiskinova "Silicon nanowires grown on Si(100) substrates via thermal reactions with carbon nanoparticles" *Chemical Physics Letters* **371** (2003) 394.

[14] J. J. Niu, J. Sha, Z. H. Liu, Z. X. Su, J. Yu, D. R. Yang "Silicon nanowires fabricated by thermal evaporation of silicon wafer" *Physica E-Low-Dimensional Systems & Nanostructures* **24** (2004) 268.

[15] Y. G. Wang, A. Z. Jin, Z. Zhang "Cu/SiO$_{2-x}$ nanowires with compositional modulation structure grown via thermal evaporation" *Applied Physics Letters* **81** (2002) 4425.

[16] K. Kakushima, T. Bourouina, T. Sarnet, G. Kerrien, D. Debarre, J. Boulmer, H. Fujita "Silicon periodic nano-structures obtained by laser exposure of nano-wires" *Microelectronics Journal* **36** (2005) 629.

[17] J. J. Niu, J. Sha, D. R. Yang "Sulfide-assisted growth of silicon nano-wires by thermal evaporation of sulfur powders" *Physica E-Low-Dimensional Systems & Nanostructures* **24** (2004) 278.

[18] J. J. Niu, J. Sha, D. R. Yang "Silicon nano-wires fabricated by a novel thermal evaporation of zinc sulfide" *Physica E-Low-Dimensional Systems & Nanostructures* **24** (2004) 178.

[19] J. J. Niu, J. Sha, L. Wang, Y. J. Ji, D. R. Yang “Silicon nano-wires grown at low temperature” *Physica E-Low-Dimensional Systems & Nanostructures* **27** (2005) 309.

[20] J. J. Niu, J. Sha, X. Y. Ma, J. Xu, D. Yang “Array-orderly single crystalline silicon nano-wires” *Chemical Physics Letters* **367** (2003) 528.

[21] Z. X. Su, J. Sha, J. J. Niu, J. X. Liu, D. R. Yang “Synthesis and raman spectra of Si-nanowires” *Physica E-Low-Dimensional Systems & Nanostructures* **203** (2006) 792.

[22] F. Nakajima, J. Motohisa, T. Fukui “Self-formed quantum nano-structures by selective area MOVPE and their application to GaAs single electron devices” *Applied Surface Science* **162** (2000) 650.

[23] Y. Huang, X. F. Duan, Y. Cui, L. J. Lauhon, K. H. Kim, C. M. Lieber “Logic gates and computation from assembled nanowire building blocks” *Science* **294** (2001) 1313.

[24] A. Bachtold, P. Hadley, T. Nakanishi, C. Dekker “Logic circuits with carbon nanotube transistors” *Science* **294** (2001) 1317.

[25] V. Derycke, R. Martel, J. Appenzeller, P. Avouris “Carbon nanotube inter- and intramolecular logic gates” *Nano Letters* **1** (2001) 453.

[26] Y. Cui, C. M. Lieber “Functional nanoscale electronic devices assembled using silicon nanowire building blocks” *Science* **291** (2001) 851.

[27] L. G. Wang, Y. Li, D. W. Yu, J. Wang “Quantum transport of four-terminal nano-molecular bridge” *Acta Physica Sinica* **54** (2005) 233.

[28] M. Sakai, M. Iizuka, M. Nakamura, K. Kudo “Organic nano-transistor fabricated by co-evaporation method under alternating electric field” *Synthetic Metals* **153** (2005) 293.

[29] T. Komoda, X. Sheng, N. Koshida “Mechanism of efficient and stable surface-emitting cold cathode based on porous polycrystalline silicon films” *Journal of Vacuum Science & Technology B* **17** (1999) 1076.

[30] X. F. Duan, Y. Huang, Y. Cui, J. F. Wang, C. M. Lieber “Indium phosphide nanowires as building blocks for nanoscale electronic and optoelectronic devices” *Nature* **409** (2001) 66.

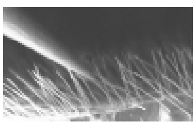

[31] M. Ishida, T. Kawano, M. Futagawa, Y. Arai, H. Takao, K. Sawada "A Si nano-micro-wire array on a Si(111) substrate and field emission device applications" *Superlattices and Microstructures* **34** (2003) 567.

[32] N. Ooike, J. Motohisa, T. Fukui "MOVPE selectively grown GaAs nanowires with self-aligned W side gate" *Journal of Crystal Growth* **272** (2004) 175.

[33] Y. G. Sun, J. A. Rogers "Fabricating semiconductor nano/microwires and transfer printing ordered arrays of them onto plastic substrates" *Nano Letters* **4** (2004) 1953.

[34] T. Namazu, Y. Isono "Quasi-static bending test of nano-scale SiO_2 wire at intermediate temperatures using afm-based technique" *Sensors and Actuators A-Physical* **104** (2003) 78.

[35] Z. L. Wang "Zinc oxide nanostructures: growth, properties and applications" *Journal of Physics-Condensed Matter* **16** (2004) R829.

[36] H. J. Fan, R. Scholz, F. M. Kolb, M. Zacharias "Two-dimensional dendritic ZnO nanowires from oxidation of Zn microcrystals" *Applied Physics Letters* **85** (2004) 4142.

[37] P. Raji, S. Sivakanth, K. K. Umesh, S. K. Ramakrishnan, K. Ramachandran "Growth, optical and thermal properties of zinc oxide nano wires" *International Journal of Modern Physics B* **19** (2005) 4247.

[38] J. W. Schultze, A. Bressel "Principles of electrochemical micro- and nanosystem technologies" *Electrochimica Acta* **47** (2001) 3.

[39] H. Masuda, K. Fukuda "Ordered metal nanohole arrays made by a 2-step replication of honeycomb structures of anodic alumina" *Science* **268** (1995) 1466.

[40] H. Masuda, H. Yamada, M. Satoh, H. Asoh, M. Nakao, T. Tamamura "Highly ordered nanochannel-array architecture in anodic alumina" *Applied Physics Letters* **71** (1997) 2770.

[41] J. Kunze, A. Seyeux, P. Schmuki "Anodic TiO_2 layer conversion: Fluoride-induced rutile formation at room temperature" *Electrochemical and Solid State Letters* **11** (2008) K11.

[42] H. Masuda, H. Asoh, M. Watanabe, K. Nishio, M. Nakao, T. Tamamura "Square and triangular nanohole array architectures in anodic alumina" *Advanced Materials* **13** (2001) 189.

[43] G. Sauer, G. Brehm, S. Schneider, K. Nielsch, R. B. Wehrspohn, J. Choi, H. Hofmeister, U. Gosele "Highly ordered monocrystalline silver nanowire arrays" *Journal of Applied Physics* **91** (2002) 3243.

[44] D. Dobrev, J. Vetter, N. Angert, R. Neumann "Periodic reverse current electrodeposition of gold in an ultrasonic field using ion-track membranes as templates: growth of gold single-crystals" *Electrochimica Acta* **45** (2000) 3117.

[45] J. S. Lee, G. H. Gu, H. Kim, K. S. Jeong, J. Bae, J. S. Suh "Growth of carbon nanotubes on anodic aluminum oxide templates: Fabrication of a tube-in-tube and linearly joined tube" *Chemistry of Materials* **13** (2001) 2387.

[46] J. S. Lee, G. H. Gu, H. Kim, J. S. Suh, I. Han, N. S. Lee, J. M. Kim, G. S. Park "Well-ordered Co nanowire arrays for aligned carbon nanotube arrays" *Synthetic Metals* **124** (2001) 307.

[47] H. Asoh, S. Sakamoto, S. Ono "Metal patterning on silicon surface by site-selective electroless deposition through colloidal crystal templating" *Journal of Colloid and Interface Science* **316** (2007) 547.

[48] Y. Piao, H. Lim, J. Y. Chang, W. Y. Lee, H. Kim "Nanostructured materials prepared by use of ordered porous alumina membranes" *Electrochimica Acta* **50** (2005) 2997.

[49] A. Mozalev, M. Sakairi, I. Saeki, H. Takahashi "Nucleation and growth of the nanostructured anodic oxides on tantalum and niobium under the porous alumina film" *Electrochimica Acta* **48** (2003) 3155.

[50] K. R. Pirota, D. Navas, M. Hernandez-Velez, K. Nielsch, M. Vazquez "Novel magnetic materials prepared by electrodeposition techniques: arrays of nanowires and multi-layered microwires" *Journal of Alloys and Compounds* **369** (2004) 18.

[51] S. W. Lin, S. C. Chang, R. S. Liu, S. F. Hu, N. T. Jan "Fabrication and magnetic properties of nickel nanowires" *Journal of Magnetism and Magnetic Materials* **282** (2004) 28.

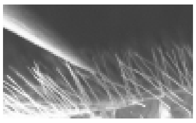

[52] S. Kato, H. Shinagawa, H. Okada, G. Kido, K. Mitsuhashi “Application of ferromagnetic nano-wires in porous alumina arrays for magnetic force generator” *Science and Technology of Advanced Materials* **6** (2005) 341.

[53] T. M. Whitney, J. S. Jiang, P. C. Searson, C. L. Chien “Fabrication and magnetic-properties of arrays of metallic nanowires” *Science* **261** (1993) 1316.

[54] W. Kautek, S. Reetz, S. Pentzien “Template electrodeposition of nanowire arrays on gold foils fabricated by pulsed-laser deposition” *Electrochimica Acta* **40** (1995) 1461.

[55] M. Sima, I. Enculescu, A. Ioncea, T. Visan, C. Trautmann “Manganese and copper doped CdS nanowire arrays preparation” *Journal of Optoelectronics and Advanced Materials* **6** (2004) 1193.

[56] N. J. Tao “Electrochemical fabrication of metallic quantum wires” *Journal of Chemical Education* **82** (2005) 720.

[57] A. Bai, C. C. Hu “Cyclic voltammetric deposition of nanostructured iron-group alloys in high-aspect ratios without using templates” *Electrochemistry Communications* **5** (2003) 619.

[58] C. X. Ji, P. C. Searson “Fabrication of nanoporous gold nanowires” *Applied Physics Letters* **81** (2002) 4437.

[59] Z. G. Bai, D. P. Yu, H. Z. Zhang, Y. Ding, Y. P. Wang, X. Z. Gal, Q. L. Hang, G. C. Xiong, S. Q. Feng “Nano-scale GeO_2 wires synthesized by physical evaporation” *Chemical Physics Letters* **303** (1999) 311.

[60] M. S. Gudiksen, L. J. Lauhon, J. Wang, D. C. Smith, C. M. Lieber “Growth of nanowire superlattice structures for nanoscale photonics and electronics” *Nature* **415** (2002) 617.

[61] J. C. Bao, D. P. Xu, Q. F. Zhou, Z. Xu “An array of concentric composite nanostructure of metal nanowires encapsulated in zirconia nanotubes: Preparation, characterization, and magnetic properties” *Chemistry of Materials* **14** (2002) 4709.

[62] A. V. Alekseeva, V. A. Bogatyrev, B. N. Khlebtsov, A. G. Mel’nikov, L. A. Dykman, N. G. Khlebtsov “Gold nanorods: Synthesis and optical properties” *Colloid Journal* **68** (2006) 661.

[63] M. Tsuji, M. Hashimoto, Y. Nishizawa, T. Tsuji “Synthesis of gold nanorods and nanowires by a microwave-polyol method” *Materials Letters* **58** (2004) 2326.

[64] P. Selvakannan, S. Mandal, R. Pasricha, M. Sastry “Hydrophobic, organically dispersible gold nanoparticles of variable shape produced by the spontaneous reduction of aqueous chloroaurate ions by hexadecylaniline molecules” *Journal of Colloid and Interface Science* **279** (2004) 124.

[65] S. Karim, M. E. Toimil-Molares, F. Maurer, G. Miehe, W. Ensinger, J. Liu, T. W. Cornelius, R. Neumann “Synthesis of gold nanowires with controlled crystallographic characteristics” *Applied Physics A-Materials Science & Processing* **84** (2006) 403.

[66] J. L. Zhang, J. M. Du, B. X. Han, Z. M. Liu, T. Jiang, Z. F. Zhang “Sonochemical formation of single-crystalline gold nanobelts” *Angewandte Chemie-International Edition* **45** (2006) 1116.

[67] A. Halder, N. Ravishankar “Ultrafine single-crystalline gold nanowire arrays by oriented attachment” *Advanced Materials* **19** (2007) 1854.

[68] Z. Y. Gu, H. K. Ye, A. Bernfeld, K. J. T. Livi, D. H. Gracias “Three-dimensional electrically interconnected nanowire networks formed by diffusion bonding” *Langmuir* **23** (2007) 979.

[69] P. Diaconis, S. Holmes, R. Montgomery “Dynamical bias in the coin toss” *Siam Review* **49** (2007) 211.

[70] S. Milenković, A. Schneider, A. W. Hassel “Gold nanostructures by directional solid-state decomposition” *Gold Bulletin* **39** (2006) 185.

[71] Y. Chen, S. Milenkovic, A. W. Hassel “Arrays of iso-oriented gold nanobelts” *Nano Letters* **8** (2008) 737.

[72] F. S. Galasso “Unidirectionally solidified eutectics for optical electronic and magnetic applications” *Journal of Metals* **19** (1967) 17.

[73] A. W. Hassel, B. Bello-Rodriguez, S. Milenković, A. Schneider “Electrochemical production of nanopore arrays in a nickel aluminium alloy” *Electrochimica Acta* **50** (2005) 3033.

[74] A. W. Hassel, B. Bello-Rodriguez, S. Milenković, A. Schneider “Fabrication of rhenium nanowires by selective etching of eutectic alloys” *Electrochimica Acta* **51** (2005) 795.

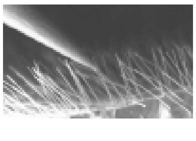

[75] F. Rüdorff "Ueber Kältemischungen" *Annalen der Physik und Chemie* **122** (1864) 337.

[76] F. Guthrie "On eutexia" *Philosophical Magazine and Journal of Science* **5** (1884) 462.

[77] B. Chalmers *Principles of Solidification* John Wiley & Sons, Inc., New York 1964.

[78] R. Vogel "Concerning eutectic crystallisation" *Zeitschrift für Anorganische Chemie* **76** (1912) 425.

[79] M. Straumanis, N. Brakšs "The structure of zinc-cadmium eutectic compounds" *Zeitschrift für Physikalische Chemie-Abteilung B-Chemie der Elementarprozesse Aufbau der Materie* **30** (1935) 117.

[80] K. A. Jackson, J. D. Hunt "Lamellar and rod eutectic growth" *Transactions of the Metallurgical Society of AiME* **236** (1966) 1129.

[81] T. Heumann, B. Predel "Constitution and thermodynamic properties of alloys" *Archiv Für Das Eisenhüttenwesen* **39** (1968) 783.

[82] W. K. Sahm, P. Rudolf *Gerichtet erstarrte eutektische Werkstoffe* Springer Verlag, Berlin 1975.

[83] D. B. Miracle "Overview no. 104 - the physical and mechanical-properties of NiAl" *Acta Metallurgica et Materialia* **41** (1993) 649.

[84] R. Rablbauer, G. Frommeyer, F. Stein "Determination of the constitution of the quasi-binary eutectic NiAl-Re system by DTA and microstructural investigations" *Materials Science and Engineering - A - Structural Materials Properties Microstructure and Processing* **343** (2003) 301.

[85] H. Bei, G. M. Pharr, E. P. George "A review of directionally solidified intermetallic composites for high-temperature structural applications" *Journal of Materials Science* **39** (2004) 3975.

[86] J. Deges, R. Fischer, G. Frommeyer, A. Schneider "Atom probe field ion microscopy investigations on the intermetallic Ni49.5Al49.5Re1 alloy" *Surface and Interface Analysis* **36** (2004) 533.

[87] H. E. Cline, D. Lee "Strengthening of lamellar vs. equiaxed Ag-Cu eutectic" *Acta Metallurgica* **18** (1970) 315.

[88] T. B. Massalski, H. Okamoto *Binary Alloy Phase Diagrams* ASM International, Chicago 1990.

[89] D. Dobrev, J. Vetter, N. Angert "Electrochemical preparation of metal microstructures on large areas of etched ion track membranes" *Nuclear Instruments & Methods in Physics Research Section B-Beam Interactions with Materials and Atoms* **149** (1999) 207.

[90] A. Z. Jin, Y. G. Wang, Z. Zhang "Synthesis and characterization of Cu/SiO_{2-x} composite nanowires" *Journal of Crystal Growth* **252** (2003) 167.

[91] Y. J. Xiong, Y. Xie, C. Z. Wu, J. Yang, Z. Q. Li, F. Xu "Formation of silver nanowires through a sandwiched reduction process" *Advanced Materials* **15** (2003) 405.

[92] Y. G. Wang, D. R. Li, Z. C. Lu, S. X. Zhou "Morphological evolution of Ag nano-wires via thermal evaporation" *Journal of Materials Science* **39** (2004) 3833.

[93] F. Scholz, U. Hasse "Controlling the morphology of silver deposition at liquid/liquid interfaces: From nano-wires to super smooth films" *Electrochemistry Communications* **7** (2005) 541.

[94] R. Rablbauer *Mikrostrukturen und Eigenschaften quasibinärer eutektischer NiAl-Re und NiAl-(Ti,Zr,Hf)B2-Legierungen für den Hochtemperatureinsatz.* PhD thesis Shaker Verlag, Aachen 2006.

[95] M. C. Flemings *Solidification Processing* McGraw-Hill, Inc., New York 1974.

[96] M. R. Aguiar, R. Caram "Directional solidification of a Sn-Se eutectic alloy using the Bridgman-Stockbarger method" *Journal of Crystal Growth* **166** (1996) 398.

[97] J. D. Hunt, K. A. Jackson "Binary eutectic solidification" *Transactions of the Metallurgical Society of AiME* **236** (1966) 843.

[98] W. Kurz, D. J. Fischer *Fundamentals of Solidification* Trans Tech Publications Ltd., Uetikon-Zuerich 1998.

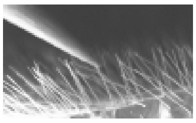

[99] S. Brittman, A. J. Smith, S. Milenković, A. W. Hassel "Copper nanowires and silver micropit arrays from the electrochemical treatment of a directionally solidified silver-copper eutectic" *Electrochimica Acta* **53** (2007) 324.

[100] J. C. Liu, R. Elliott "Selfconsistent solutions for lamellar eutectic growth" *Acta Metallurgica et Materialia* **43** (1995) 3301.

[101] W. J. Boettinger, S. R. Coriell, A. L. Greer, A. Karma, W. Kurz, M. Rappaz, R. Trivedi "Solidification microstructures: Recent developments, future directions" *Acta Materialia* **48** (2000) 43.

[102] E. Cadirli, M. Gunduz "The directional solidification of Pb-Sn alloys" *Journal of Materials Science* **35** (2000) 3837.

[103] S. Milenković, A. W. Hassel, A. Schneider "Effect of the growth conditions on the spatial features of Re nanowires produced by directional solidification" *Nano Letters* **6** (2006) 794.

[104] W. Massa *Kristallstrukturbestimmung* Teubner Verlag, Stuttgart 2007.

[105] M. McLean *Directionally Solidified Materials for High Temperature Service* The Metals Society, London 1983.

[106] H. E. Cline, J. L. Walter, E. F. Koch, L. M. Osika "Variation of interface dislocation networks with lattice mismatch in eutectic alloys" *Acta Metallurgica* **19** (1971) 405.

[107] W. T. Read, W. Shockley "Dislocation models of crystal grain boundaries" *Physical Review* **78** (1950) 275.

[108] W. T. Read "Quantitative prediction of grain boundary energies by anisotropic dislocation theory" *Physical Review* **78** (1950) 350.

[109] W. Shockley, W. T. Read "Quantitative predictions from dislocation models of crystal grain boundaries" *Physical Review* **75** (1949) 692.

[110] E. Scheil "Über die eutektische Kristallisation" *Zeitschrift für Metallkunde* **45** (1954) 298.

[111] R. W. Kraft "Structure of Mg-Mg_2Sn eutectic" *Transactions of the Metallurgical Society of AiME* **227** (1963) 393.

[112] G. A. Chadwick “Interphase interfaces in lamellar growth” *Journal of the Australian Institute of Metals* **10** (1965) 178.

[113] V. S. Stubican, R. C. Bradt “Eutectic solidification in ceramic systems” *Annual Review of Materials Science* **11** (1981) 267.

[114] J. L. Walter, H. E. Cline, E. F. Koch “Interface dislocations in directionally solidified NiAl-Cr eutectic” *Transactions of the Metallurgical Society of AiME* **245** (1969) 2073.

[115] J. L. Walter, H. E. Cline, E. F. Koch “Interface dislocations in directionally solidified NiAl-Cr eutectic” *Journal of Metals* **21** (1969) A125.

[116] J. L. Walter, H. E. Cline “Effect of solidification rate on structure and high-temperature strength of eutectic NiAl-Cr” *Metallurgical Transactions* **1** (1970) 1221.

[117] H. E. Cline, J. L. Walter “Effect of alloy additions on rod-plate transition in eutectic NiAl-Cr” *Metallurgical Transactions* **1** (1970) 2907.

[118] H. E. Cline, J. L. Walter, E. Lifshin, R. R. Russell “Structures, faults and rod-plate transition in eutectics” *Metallurgical Transactions* **2** (1971) 189.

[119] L. Plazanet, F. Nardou “Reaction process during relative sintering of NiAl” *Journal of Materials Science* **33** (1998) 2129.

[120] M. Winter “WebElements periodic table” (www.webelements.com, 2007-10-14).

[121] G. Frommeyer, R. Fischer, J. Deges, R. Rablbauer, A. Schneider “APFIM investigations on site occupancies of the ternary alloying elements Cr, Fe, and Re in NiAl” *Ultramicroscopy* **101** (2004) 139.

[122] J. Deges, A. Schneider, R. Fischer, G. Frommeyer “APFIM investigations on quasi-binary hypoeutectic NiAl-Re alloys” *Materials Science and Engineering - A - Structural Materials Properties Microstructure and Processing* **353** (2003) 80.

[123] R. Fischer, G. Frommeyer, A. Schneider “APFIM investigations on site preferences, superdislocations, and antiphase boundaries in NiAlCr with B2 superlattice structure” *Materials Science and Engineering - A - Structural Materials Properties Microstructure and Processing* **353** (2003) 87.

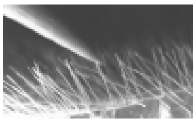

[124] Z. G. Liu, G. Frommeyer, M. Kreuss "Atom probe FIM investigations on the intermetallic NiAl phase with B2 superlattice structure" *Surface Science* **246** (1991) 272.

[125] C. H. Hamann, W. Vielstich, A. Hammet *Electrochemistry* Wiley-VCH, Weinheim 1998.

[126] J. Kawakita, M. Stratmann, A. W. Hassel "High voltage pulse anodization of a NiTi shape memory alloy" *Journal of the Electrochemical Society* **154** (2007) C294.

[127] A. Güntherschulze, H. Betz "Die Bewegung der Ionengitter von Isolatoren bei extremen elektrischen Feldstärken" *Zeitschrift für Physk* **91** (1934) 367.

[128] E. J. W. Verwey "Electrolytic conduction of a solid insulator at high fields - the formation of the anodic oxide film on aluminium" *Physica* **2** (1935) 1059.

[129] N. F. Mott "The theory of the formation of protective oxide films on metals 3" *Transactions of the Faraday Society* **43** (1947) 429.

[130] N. F. Mott "L'oxydation des metaux" *Journal de Chimie Physique et de Physico-Chimie Biologique* **44** (1947) 172.

[131] N. Cabrera, N. F. Mott "Theory of the oxidation of metals" *Reports on Progress in Physics* **12** (1948) 163.

[132] F. DiQuarto, A. DiPaola, C. Sunseri "Kinetics of growth of amorphous WO_3 anodic films on tungsten" *Journal of the Electrochemical Society* **127** (1980) 1016.

[133] M. M. Lohrengel "Thin anodic oxide layers on aluminum and other valve metals - High-Field Regime" *Materials Science & Engineering R-Reports* **R11** (1993) 243.

[134] F. DiQuarto, A. DiPaola, C. Sunseri "Semiconducting properties of anodic WO_3 amorphous films" *Electrochimica Acta* **26** (1981) 1177.

[135] S. R. Biaggio, R. C. RochaFilho, J. R. Vilche, F. E. Varela, L. M. Gassa "A study of thin anodic WO_3 films by electrochemical impedance spectroscopy" *Electrochimica Acta* **42** (1997) 1751.

[136] D. D. Macdonald, E. Sikora, J. Sikora "The kinetics of growth of the passive film on tungsten in acidic phosphate solutions" *Electrochimica Acta* **43** (1998) 2851.

[137] M. Metikos-Hukovic, R. Babic "Passivation and corrosion behaviours of cobalt and cobalt-chromium-molybdenum alloy" *Corrosion Science* **49** (2007) 3570.

[138] A. Giraudea, P. Lemoine, M. Gross "Electrochemical oxidation of rhenium" *Corrosion Science* **13** (1973) 421.

[139] D. Ng, M. Kulkarni, J. Johnson, A. Zinovev, D. Yang, H. Liang "Oxidation and removal mechanisms during chemical-mechanical planarization" *Wear* **263** (2007) 1477.

[140] E. Abelev, A. J. Smith, A. W. Hassel, Y. Ein-Eli "Copper repassivation characteristics in carbonate-based solutions" *Journal of the Electrochemical Society* **153** (2006) B337.

[141] E. Abelev, A. J. Smith, A. W. Hassel, Y. Ein-Eli "Potassium sorbate solutions as copper chemical mechanical planarization (CMP) based slurries" *Electrochimica Acta* **52** (2007) 5150.

[142] E. Abelev, D. Starosvetsky, Y. Ein-Eli "Potassium sorbate - A new aqueous copper corrosion inhibitor electrochemical and spectroscopic studies" *Electrochimica Acta* **52** (2007) 1975.

[143] B. Macdougal, M. Cohen "Anodic-oxidation of nickel in neutral sulfate solution" *Journal of the Electrochemical Society* **121** (1974) 1152.

[144] C. V. D'Alkaine, M. A. Santanna "The passivating films on nickel in alkaline solutions I. general aspects of the Ni(II) region" *Journal of Electroanalytical Chemistry* **457** (1998) 5.

[145] C. V. D'Alkaine, M. A. Santanna "Passivating films on nickel in alkaline solutions II. Ni(II) anodic film growth: quantitative treatment and the influence of the OH^- concentration" *Journal of Electroanalytical Chemistry* **457** (1998) 13.

[146] L. Cassayre, P. Chamelot, L. Arurault, L. Massot, P. Palau, P. Taxil "Electrochemical oxidation of binary copper-nickel alloys in cryolite melts" *Corrosion Science* **49** (2007) 3610.

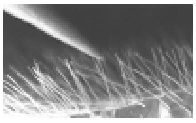

[147] W. A. Badawy, F. M. Al-Kharafi, A. S. El-Azab "Electrochemical behaviour and corrosion inhibition of Al, Al-6061 and Al-Cu in neutral aqueous solutions" *Corrosion Science* **41** (1999) 709.

[148] W. A. Badawy, R. M. El-Sherif, H. Shehata "Electrochemical behavior of aluminum bronze in sulfate-chloride media" *Journal of Applied Electrochemistry* **37** (2007) 1099.

[149] K. S. Tan, A. W. Hassel, M. Stratmann "Design and construction of a micro-indenter for tribological investigations" *Materialwissenschaft und Werkstofftechnik* **36** (2005) 13.

[150] E. Akiyama, M. Stratmann, A. W. Hassel "Discrete electrochemical transients of aluminium alloys generated by slurry jet impingement" *Journal of Physics D-Applied Physics* **39** (2006) 3157.

[151] A. J. Smith, M. Stratmann, A. W. Hassel "Investigation of the effect of impingement angle on tribocorrosion using single impacts" *Electrochimica Acta* **51** (2006) 6521.

[152] A. W. Hassel, A. J. Smith "Single particle impact experiments for studying particle induced flow corrosion" *Corrosion Science* **49** (2007) 231.

[153] M. Pourbaix *Atlas of Electrochemical Equilibria in Aqueous Solutions* Pergamon Press Ltd, Headington Hill, Oxford 1966.

[154] W. D. Larson, F. H. MacDougall "The mercurous acetate electrode" *Journal of Physical Chemistry* **41** (1937) 493.

[155] A. W. Hassel *Elektronische und Ionische Transportprozesse in ultradünnen Ventilmetalloxidschichten* PhD thesis Shaker Verlag 1997.

[156] A. W. Hassel, K. Fushimi, M. Seo "An agar-based silver / silver chloride reference electrode for use in micro-electrochemistry" *Electrochemistry Communications* **1** (1999) 180.

[157] K. A. Lill, A. W. Hassel "A combined µ-mercury reference electrode/Au counter-electrode system for microelectrochemical applications" *Journal of Solid State Electrochemistry* **10** (2006) 941.

[158] U. Kreibig, D. Wagner "Oberflächenplasmonen auf Silber-Nanodrähten" *Photonik* **3** (2005) 105 supplement "Nanotechnik".

[159] A. W. Hassel, A. J. Smith, S. Milenković "Nanostructures from directionally solidified NiAl-W eutectic alloys" *Electrochimica Acta* **52** (2006) 1799.

[160] A. W. Hassel, M. M. Lohrengel "The scanning droplet cell and its application to structured nanometer oxide films on aluminium" *Electrochimica Acta* **42** (1997) 3327.

[161] A. I. Mardare, A. D. Wieck, A. W. Hassel "Microelectrochemical lithography: A method for direct writing of surface oxides" *Electrochimica Acta* **52** (2007) 7865.

[162] B. Bello-Rodriguez, A. Schneider, A. W. Hassel "Preparation of ultramicroelectrode array of gold hemispheres on nanostructured NiAl-Re" *Journal of the Electrochemical Society* **153** (2006) C33.

[163] M. Noyong, K. Blech, A. Rosenberger, V. Klocke, U. Simon "In situ nanomanipulation system for electrical measurements in sem" *Measurement Science & Technology* **18** (2007) N84.

[164] M. Rogers, G. Kothleitner, A. Berendes, W. Bock, B. O. Kolbesen "Focused ion beam preparation and EFTEM/EELS studies on vanadium nitride thin films" *Praktische Metallographie-Practical Metallography* **42** (2005) 172.

[165] A. W. Hassel, V. Cimalla, C. Röhlig, J. Pezoldt, M. Niebelschütz, O. Ambacher, K. Brückner, M. Hein, J. Weber, S. Milenković, A. J. Smith "Nanomechanics of single crystalline tungsten nanowires" *Journal of Nanomaterials* **in press** (2008).

[166] H. Okamoto "Ga-Pt (Gallium-Platinum)" *Journal of Phase Equilibria and Diffusion* **28** (2007) 494.

[167] A. Hollemann, E. Wiberg, N. Wiberg *Lehrbuch der Anorganischen Chemie* de Gruyter, Berlin 101 Aufl. 1995.

[168] L. Philippe, I. Peyrot, J. Michler, A. W. Hassel, S. Milenković "Yield stress of monocrystalline rhenium nanowires" *Applied Physics Letters* **91** (2007) 111919.

[169] J. N. Florando, W. D. Nix "A microbeam bending method for studying stress-strain relations for metal thin films on silicon substrates" *Journal of the Mechanics and Physics of Solids* **53** (2005) 619.

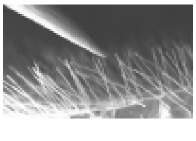

[170] S. Hoffmann, I. Utke, B. Moser, J. Michler, S. H. Christiansen, V. Schmidt, S. Senz, P. Werner, U. Gosele, C. Ballif "Measurement of the bending strength of vapor-liquid-solid grown silicon nanowires" *Nano Letters* **6** (2006) 622.

[171] G. Feng, W. D. Nix, Y. Yoon, C. J. Lee "A study of the mechanical properties of nanowires using nanoindentation" *Journal of Applied Physics* **99** (2006) 074304.

[172] G. Feng, S. Qu, Y. Huang, W. D. Nix "An analytical expression for the stress field around an elastoplastic indentation/contact" *Acta Materialia* **55** (2007) 2929.

[173] W. D. Nix, J. R. Greer, G. Feng, E. T. Lilleodden "Deformation at the nanometer and micrometer length scales: Effects of strain gradients and dislocation starvation" *Thin Solid Films* **515** (2007) 3152.

[174] M. D. Uchic, D. M. Dimiduk, J. N. Florando, W. D. Nix "Sample dimensions influence strength and crystal plasticity" *Science* **305** (2004) 986.

[175] R. W. Kraft, D. L. Albright, J. A. Ford "Anomalous thermal stability of Al-CuAl2 eutectic specimens" *Transactions of the Metallurgical Society of AiME* **227** (1963) 540.

[176] E. R. Thompson, F. D. Lemkey "Structure and properties of Ni_3Al eutectic alloys produced by unidirectional solidification" *ASM Transactions Quarterly* **62** (1969) 140.

[177] T. R. Powers, R. E. Goldstein "Pearling and pinching: Propagation of Rayleigh instabilities" *Physical Review Letters* **78** (1997) 2555.

[178] K. F. Gurski, G. B. McFadden "The effect of anisotropic surface energy on the Rayleigh instability" *Proceedings of the Royal Society of London Series A-Mathematical Physical and Engineering Sciences* **459** (2003) 2575.

[179] J. G. Hagedorn, N. S. Martys, J. F. Douglas "Breakup of a fluid thread in a confined geometry: droplet-plug transition, perturbation sensitivity, and kinetic stabilization with confinement" *Physical Review E* **69** (2004).

[180] E. Wuchina, E. Opila, M. Opeka, W. Fahrenholtz, I. Talmy "UHTCs: Ultra-high temperature ceramic materials for extreme environment applications" *Interface* **15** (2007) 30.

[181] J. R. Baylis "Tungsten wire for hydrogen-ion determinations" *Industrial and Engineering Chemistry* **15** (1923) 852.

[182] P. C. Caldwell "Measurement of intracellular pH by means of a tungsten microelectrode" *Journal of Physiology-London* **120** (1953) P31.

[183] P. C. Caldwell "An investigation of the intracellular pH of crab muscle fibres by means of micro-glass and micro-tungsten electrodes" *Journal of Physiology-London* **126** (1954) 169.

[184] B. Reichman, A. J. Bard "Electrochromic process at WO_3 electrodes prepared by vacuum evaporation and anodic-oxidation of W" *Journal of the Electrochemical Society* **126** (1979) 583.

[185] P. I. Ortiz, M. L. Teijelo, M. C. Giordano "Electrochemical-behavior of tungsten in alkaline media .1. NaOH solutions" *Journal of Electroanalytical Chemistry* **243** (1988) 379.

[186] P. I. Ortiz, M. C. Giordano, M. L. Teijelo "Electrochemical-behavior of tungsten in alkaline media .2. sodium-carbonate solutions" *Journal of Electroanalytical Chemistry* **251** (1988) 393.

[187] M. J. Natan, T. E. Mallouk, M. S. Wrighton "pH-sensitive WO_3-based microelectrochemical transistors" *Journal of Physical Chemistry* **91** (1987) 648.

[188] K. Yamamoto, G. Y. Shi, T. S. Zhou, F. Xu, M. Zhu, M. Liu, T. Kato, J. Y. Jin, L. T. Jin "Solid-state pH ultramicrosensor based on a tungstic oxide film fabricated on a tungsten nanoelectrode and its application to the study of endothelial cells" *Analytica Chimica Acta* **480** (2003) 109.

[189] T. C. McIlvaine "A buffer solution for colorimetric comparison" *Journal of Biological Chemistry* **49** (1921) 183.

[190] F. Pithan, C. Staudt-Bickel, S. Hess, R. N. Lichtenthaler "Polymeric membranes for aromatic/aliphatic separation processes" *Chemphyschem* **3** (2002) 856.

[191] D. Katarzynski, C. Staudt "Permeation properties of different aromatic substances in multicomponent aromatic/aliphatic pervaporation experiments" *Desalination* **200** (2006) 23.

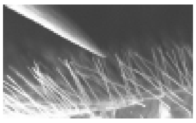

[192] C. Yu, S. F. Lee, Y. D. Yao, M. S. Wong, E. W. Huang, Y. R. Ma, J. L. Tsai, C. R. Chang "Fabrication and physical properties of permalloy nano-size wires" *Physica B-Condensed Matter* **327** (2003) 247.

[193] M. Wilms, J. Conrad, K. Vasilev, M. Kreiter, G. Wegner "Manipulation and conductivity measurements of gold nanowires" *Applied Surface Science* **238** (2004) 490.

[194] Y. Inoue, Y. Okamoto, J. Morimoto "Thermoelectric properties of porous zinc oxide ceramics doped with praseodymium" *Journal of Materials Science* **43** (2008) 368.

[195] S. Roy, A. Salomonsson, A. L. Spetz, C. Aulin, P. O. Kall, L. Ojamae, M. Strand, M. Sanati "Metal oxide nanoparticles as novel gate materials for field-effect gas sensors" *Materials and Manufacturing Processes* **21** (2006) 275.

[196] R. M. Penner, C. R. Martin "Preparation and electrochemical characterization of ultramicroelectrode ensembles" *Analytical Chemistry* **59** (1987) 2625.

[197] K. Borgwarth, D. Ebling, J. Heinze "Applications of scanning ultra micro electrodes for studies on surface conductivity" *Electrochimica Acta* **40** (1995) 1455.

[198] P. Van Gerwen, W. Laureyn, W. Laureys, G. Huyberechts, M. O. De Beeck, K. Baert, J. Suls, W. Sansen, P. Jacobs, L. Hermans, R. Mertens "Nanoscaled interdigitated electrode arrays for biochemical sensors" *Sensors and Actuators B-Chemical* **49** (1998) 73.

[199] H. J. Lee, C. Beriet, R. Ferrigno, H. H. Girault "Cyclic voltammetry at a regular microdisc electrode array" *Journal of Electroanalytical Chemistry* **502** (2001) 138.

[200] A. C. Barton, S. D. Collyer, F. Davis, D. D. Gornall, K. A. Law, E. C. D. Lawrence, D. W. Mills, S. Myler, J. A. Pritchard, M. Thompson, S. P. J. Higson "Sonochemically fabricated microelectrode arrays for biosensors offering widespread applicability: Part I" *Biosensors & Bioelectronics* **20** (2004) 328.

[201] K. Dill, D. D. Montgomery, A. L. Ghindilis, K. R. Schwarzkopf, S. R. Ragsdale, A. V. Oleinikov "Immunoassays based on electrochemical detection using microelectrode arrays" *Biosensors & Bioelectronics* **20** (2004) 736.

[202] C. G. J. Koopal, B. Deruiter, R. J. M. Nolte “Amperometric biosensor based on direct communication between glucose-oxidase and a conducting polymer inside the pores of a filtration membrane” *Journal of the Chemical Society-Chemical Communications* (1991) 1691.

[203] J. Pritchard, K. Law, A. Vakurov, P. Millner, S. P. J. Higson “Sonochemically fabricated enzyme microelectrode arrays for the environmental monitoring of pesticides” *Biosensors & Bioelectronics* **20** (2004) 765.

[204] S. A. Radke, E. C. Alocilja “A high density microelectrode array biosensor for detection of E-coli O157:H7” *Biosensors & Bioelectronics* **20** (2005) 1662.

[205] V. V. Cosofret, M. Erdosy, T. A. Johnson, R. P. Buck, R. B. Ash, M. R. Neuman “Microfabricated sensor arrays sensitive to pH and K^+ for ionic distribution measurements in the beating heart” *Analytical Chemistry* **67** (1995) 1647.

[206] P. J. Kulesza, L. R. Faulkner “Electrochemical preparation of electrodes modified with non-stoichiometric mixed-valent tungsten(VI, V) oxides” *Journal of Electroanalytical Chemistry* **248** (1988) 305.

[207] I. G. Casella, M. Contursi “Electrochemical and spectroscopic characterization of a tungsten electrode as a sensitive amperometric sensor of small inorganic ions” *Electrochimica Acta* **50** (2005) 4146.

[208] A. Hermans, R. M. Wightman “Conical tungsten tips as substrates for the preparation of ultramicroelectrodes” *Langmuir* **22** (2006) 10348.

[209] B. Bello-Rodriguez, A. J. Smith, A. W. Hassel “Electrodeposition of gold on tungsten nanowires present in NiAl-W eutectics” *Journal of Electroanalytical Chemistry* **in press** (2008).

[210] K. Yum, H. N. Cho, J. Hu, M.-F. Yu “Individual nanotube-based needle nanoprobes for electrochemical studies in picoliter microenvironments” *ACS Nano* **1** (2007) 440.

[211] M. Saito, H. Matsuoka “pH microelectrode-micropipette system for the measurement of enzyme reactions in a picoliter volume of a living plant cell” *Analytica Chimica Acta* **404** (2000) 223.

[212] C. Colombo, T. Kappes, P. C. Hauser “Coulometric micro-titrator with a ruthenium dioxide pH-electrode” *Analytica Chimica Acta* **412** (2000) 69.

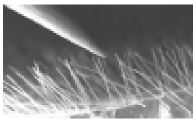

[213] J. C. Chou, J. L. Chiang "Ion sensitive field effect transistor with amorphous tungsten trioxide gate for pH sensing" *Sensors and Actuators B-Chemical* **62** (2000) 81.

[214] J. He, P. H. Cutler, N. M. Miskovsky "Generalization of Fowler-Nordheim field-emission theory for nonplanar metal emitters" *Applied Physics Letters* **59** (1991) 1644.

[215] K. Subramanian, Y. Wong, W. P. Kang, J. L. Davidson, B. K. Choi, M. Howell "Field emission devices for advanced electronics comprised of lateral nanodiamond or carbon nanotube emitters" *Diamond and Related Materials* **16** (2007) 1997.

[216] Y. M. Wong, W. P. Kang, J. L. Davidson, D. V. Kerns, J. H. Huang "Development of carbon nanotubes vacuum field emission differential amplifier integrated circuit" *Journal of Vacuum Science & Technology B* **25** (2007) 627.

[217] J. P. Calame, H. F. Gray, J. L. Shaw "Analysis and design of microwave-amplifiers employing field-emitter arrays" *Journal of Applied Physics* **73** (1993) 1485.

[218] K. L. Jensen "Field emitter arrays for plasma and microwave source applications" *Physics of Plasmas* **6** (1999) 2241.

[219] Y. L. Tung, L. S. Chen, Y. Chi, P. T. Chou, Y. M. Cheng, E. Y. Li, G. H. Lee, C. F. Shu, T. I. Wu, A. J. Carty "Orange and red organic light-emitting devices employing neutral Ru(II) emitters: Rational design and prospects for color tuning" *Advanced Functional Materials* **16** (2006) 1615.

[220] E. Cappelli, S. Orlando, G. Mattei, C. Scilletta, F. Corticelli, P. Ascarelli "Nano-structured oriented carbon films grown by PLD and CVD methods" *Applied Physics A-Materials Science & Processing* **79** (2004) 2063.

[221] R. B. Rakhi, A. L. M. Reddy, M. M. Shaijumon, K. Sethupathi, S. Ramaprabhu "Electron field emitters based on multiwalled carbon nanotubes decorated with nanoscale metal clusters" *Journal of Nanoparticle Research* **10** (2008) 179.

[222] A. W. Hassel, S. Milenković, U. Schurmann, H. Greve, V. Zaporojtchenko, R. Adelung, F. Faupel "Model systems with extreme aspect ratio, tunable geometry, and surface functionality for a quantitative investigation of the lotus effect" *Langmuir* **23** (2007) 2091.

List of Figures

Glossary

A	surface area, m^2
a	lattice constant
a_x	activity of species x, mol·l^{-1}
a_{ox}	activity of the oxidized species, mol·l^{-1}
a_{red}	activity of the reduced species, mol·l^{-1}
AFM	atomic force microscope
b	lattice constant
c	lattice constant
CBED	convergent beam electron diffraction
CCD	charge coupled device
CVD	chemical vapor deposition
D	diffusion coefficient, m^2·s^{-1}
d	distance, cm
DMM	digital multi meter
DUT	device under test
DVD	digital versatile disc
E	electrochemical potential, V
E_0	standard electrochemical potential, V
E_c	cell potential, V
E_F	Flade-potential, V
E_s	sample potential, V
e	elementary charge, 1.602×10^{-19}C
EBSD	electron backscatter diffraction
EDX	energy dispersive x-ray
ETR	electron transfer reaction

F	number of degrees of freedom
f	average length of tungsten nanowires, m
F	Faraday's number, $96\,485.33\,\mathrm{C{\cdot}mol^{-1}}$
FE	finite element
FEM	field emission microscope
FIB	focused ion beam
FRA	frequency response analyzer
G	temperature gradient, $\mathrm{K{\cdot}cm^{-1}}$
g	length of virtual wire, m
GBIP	general purpose interface bus
GIS	gas inlet system
h	Miller-Index
HDD	hard disc drive
HOPG	highly ordered pyrolitic graphite
I_c	etching current, A
i_p	residual passive current density, $\mathrm{A{\cdot}cm^{-2}}$
I_s	sample current, A
ICP	inductive coupled plasma
ITR	ion transfer reaction
K	equilibrium constant
k	Miller-Index
L	liquid phase in a phase diagram
l	Miller-Index
MOVPE	metal organic vapor phase epitaxy
MPSE	multi pressure secondary electron (detector)
N	number of components
n	number of electrons transferred
$\mathrm{N_A}$	Avogrado's number, $6.023 \times 10^{23}\mathrm{mol^{-1}}$
OCP	open circuit potential
P	number of phases
PASTE	**P**illar **AS**sisted **TE**mplating

PTFE	polytetrafluoroethylene
r	radius, m
R_W	resistance of a W nanowire, Ω
R	ideal gas constant, $8.314\,472\,\mathrm{J{\cdot}K^{-1}{\cdot}mol^{-1}}$
SAD	selected area diffraction
SDC	scanning droplet cell
SEM	scanning electron microscope
SHE	standard hydrogen electrode
SLR	single lens reflex (camera)
STM	scanning tunneling microscope
$\dot{T}$	cooling speed (change of temperature with time), $\mathrm{K{\cdot}s^{-1}}$
T	absolute temperature, K
t	time, s
TEM	transmission electron microscope
THF	tetrahydrofuran
USB	universal serial bus
V	Volume, $\mathrm{m^3}$
v	growth speed, $\mathrm{mm{\cdot}s^{-1}}$
VLS	vapor liquid solid
W	number of wires
w	diameter, m
x	fractional lattice coordinate
X	refractory metal
y	fractional lattice coordinate
z	fractional lattice coordinate
α	α-phase in a phase diagram, or angle
β	β-phase in a phase diagram, or angle
γ	angle
ΔG_r^0	Gibbs free energy, $\mathrm{J{\cdot}mol^{-1}}$
$\Delta G_{f,x}^0$	standard free formation enthalpy of species x, $\mathrm{J{\cdot}mol^{-1}}$
ΔT	temperature difference, K
ρ	density, g·m−3
ρ_Ω	resistivity, Ω·m
$\rho_{\Omega,W}$	resistivity of W, $5.29 \times 10^{-8}\Omega{\cdot}\mathrm{m}$

Index

Die hier vorgelegte Dissertation habe ich eigenständig und ohne unerlaubte Hilfe angefertigt. Die Dissertation wurde in der vorgelegten oder in ähnlicher Form noch bei keiner anderen Institution eingereicht. Ich habe bisher keine erfolglosen Promotionsversuche unternommen.

Düsseldorf, den 05.05.2008

(Andrew J. Smith)